MICROSCALE MEDIUM-TO-HIGH-TEMPERATURE REACTORS VIA MODIFIED BINDER JET PRINTING PROCESSES AND PITCH CONTROL IN NANOSPHERE PATTERNS VIA SOFT LITHOGRAPHY

By

Xiaolu Huang

A DISSERTATION

Submitted to
Michigan State University
in partial fulfillment of the requirements
for the degree of

Mechanical Engineering-Doctor of Philosophy

2019

ABSTRACT

MICROSCALE MEDIUM-TO-HIGH-TEMPERATURE REACTORS VIA MODIFIED BINDER JET PRINTING PROCESSES AND PITCH CONTROL IN NANOSPHERE PATTERNS VIA SOFT LITHOGRAPHY

By

Xiaolu Huang

A conventional approach to making miniature or microscale reactor components (e.g., heat exchangers, microreactors, separators, etc.) relies on silicon as a base material and MEMS fabrication as manufacturing processes. These Si-based microfluidic devices, however, often fail in applications involving medium-to-high-temperature operations due to lack of robust fluidic interconnects and a high-yield bonding process required to make those devices. Here we explore additive manufacturing (AM), also known as metal 3D printing, as an alternative platform to produce small scale microfluidic devices that can operate at temperature much higher than what polymers can withstand. Binder jet printing (BJP), is utilized to make stainless steel (SS) preconcentrators (PCs) with submillimeter internal features. Small-scale PCs can increase the concentration of gaseous analytes or serve as an inline injector for micro gas chromatography system (micro-GC) or portable gas sensor applications. Normally, parts printed by BJP are highly porous and thus unsuitable as fluidic components due to leaks. By adding to SS316 powder sintering additives such as boron nitride (BN), which reduces the liquid temperature, we produce near full-density SS PCs at sintering temperatures much lower than the SS melting temperature and importantly without any measurable shape distortion. Next, we leverage high initial porosity and decoupling of printing and sintering in BJP to fabricate 3D-printed heterogeneous metal/ceramic structures that are functionally graded. Functionally-graded materials (FGMs) are particularly challenging to produce in AM because of the material and processing incompatibilities caused by the thermal shrinkage/expansion mismatch and residual stress issues. We introduce a

selective-reactive sintering (SRS) process to locally tune the electrical properties of BJP-derived SS parts. The SRS process utilizes reactive gaseous environments such as oxygen during sintering and partially converts metal powders to more resistive metal oxides. The combination of BJP and SRS allows the portion of the resulting structures to possess much higher electrical resistance than the other regions, facilitating efficient electrothermal conversion for heat exchanger or reactor applications. Moreover, the heterogeneous nature of the metal/metal oxide structures significantly increases the temperature coefficient of resistance (TCR) compared to that of the raw metal. Large TCR values of the heterogeneous FGM structure makes it highly sensitive to the temperature variation, i.e., useful as resistance-temperature detectors (RTD) or anemometer-like flow sensors at medium-to-high temperatures. The second part of the dissertation is to address the intrinsic limitation of nanosphere lithography (NSL). NSL is known as one of the most inexpensive and widespread nanopatterning approaches, and in conjunction with metal-assisted chemical etching (MACE), can create an array of vertically-aligned silicon nanowires (VA-SiNWs) for various applications including highly-sensitive gas detectors and Li-ion battery anodes. However, VA-SiNWs obtained from NSL and MACE are limited in their size and spacing because the array pitch and wire diameter are inherently linked to the original nanosphere size. Here, we present deformable soft lithography using controlled deformation of elastomeric substrates and subsequent contact printing transfer to systematically control the lattice spacing and arrangements of the nanosphere array. The unique aspect of our approach is to utilize a custom-made radial stretching apparatus that allows the nanospheres to be stretched without disrupting original hexagonal arrangements over large areas. This is different from the patterns obtained from the more conventional uniaxial or biaxial stretching method whose anisotropic nature breaks the hexagonal symmetry.

ACKNOWLEDGEMENTS

All my accomplishments and honors in these years are coming from the help and the support that I have received from all professors, colleagues, friends and my family. First, I would like to express my sincere gratitude to my advisor, Professor Junghoon Yeom, for his constant encouragement, untiring help and invaluable suggestions, and offering me a great opportunity of working in his group. His guidance and support regarding both my professional study and personal life has helped me had a great life and study at MSU and will be benefit to my future career and life. Next, I would also like to thank all my committee members, Prof Patrick Kwon, Prof Wen Li and Prof Peter Lillehoj, for their suggestions and help in my Ph.D research.

I would like to thank many collaborators to help me a great deal during my research project. Thanks Dr Truong Do, Hawke Suen and Tyler Bauder in Prof. Kwon's group, for allowing and helping us to perform a lot experiments and testing. I also express my gratitude to Connor Boss who helps to develop the heating controller circuit used in two projects. I am grateful to Dr. Baokang Bi (W.M.Keck Microfabrication Facility), Dr. Karl Dersch (Enginnering Research Complex) and Dr. Daniel C. Ratchford (Naval Research Laboratory) for their help and instruments training. I thank all my fellow lab mates: Dr. Yaozhong (Ragnar) Zhang, Dr. Aryan Mehboudi, Matthew Bjork and Zirui Wang for helping me in conducting the experiments.

In addition, I want to thank all my friends for their help and encouragement throughout my Ph.D career. Last but not the least, I would express my sincere gratitude to my parents and sister for their unconditional love and support in my Ph.D study. They are the most important in my whole life.

TABLE OF CONTENTS

LIST OF TABLES

LIST OF FIGURES

CHAPTER 1

INTRODUCTION

1.1 Microreactors

Microreactors, or microchemical reactors, are miniaturized reactors in which key chemical processes such as reactions, transport, mixing, and separation occur at the length scale of typically less than 1 mm and can be found in many applications including sophisticated chemical reactions[1], nanomaterials synthesis[2] catalytic reaction[3], fuel cells[4] and biological system[5,6]. Microreactors offer numerous advantages over conventional scale reactors mainly due to high surface-area-to-volume ratio in small confinements, resulting in significant enhancements in energy efficiency, reaction speed and yield, waste reduction, safety, reliability, production flexibility, scalability, , and process controllability. Therefore, more extensive research activities have been conducted to improve the fabrication technology for microreactors and expand their applications. A higher surface-area-to-volume-ratio delivers higher stability of chemicals, higher heat and mass transfer rates for reactants and products, and a lower risk for explosive and hazardous reactions. In recent years, global demand for microreactor technology has gradually increased due to major driving factors such as increasing demand of 3D printed microreactor owing to its relative affordability and high designing capability, increasing regulations and rising safety concerns in chemical industry and others. Global Micro Reactor Technology Market was valued at USD 32,456 million in 2015 and is expected to reach USD 1,08,927.1 million by 2022 expanding with a compound annual growth rate of 19.05% [7](shown in Figure 1.1).

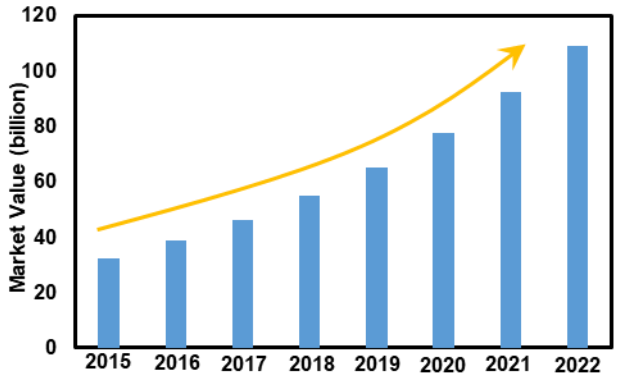

Figure 1.1 global Micro Reactor Technology Market[7]

1.1.1 Fabrication techniques of microreactors

1.1.1.1 Materials of microreactors

Microreactors are fabricated in a range of materials, including silicon, glass, polymer, metal, and ceramics[8–13]. The selection of materials depends on target applications, especially operation conditions such as temperature, pressure, and corrosivity of reactants and products. The availability of manufacturing technologies also influences the choice of reactor materials. Among the abovementioned materials, silicon is one of the first to be used as reactor structures because microfabrication technologies established from microelectronic and microelectromechanical system (MEMS) industries have been developed for silicon. Naturally, microreactors with submillimeter features can be easily produced by the existing tools. Glass has been extensively used in microfluidic and lab-on-a-chip applications mainly because transparent walls provide direct visualization of chemical reactions and characterization. While silicon and glass are well characterized for microreactor development in terms of creating fine external or internal features, they are brittle and difficult to be machined, posing issues in making fluidic interconnects and interfacing with macroscopic worlds. In addition, silicon and glass come in a form of flat plates,

and therefore, the final shape of microreactors is often limited to the planar geometry. Polymers have also been used for microreactors and can be broadly divided into two categories: polydimethylsiloxane (PDMS) and its modified versions and thermoplastic polymers[14–18]. Although polymers are widely used as microreactors thanks to merits such as flexibility in materials, a wide range of available fabrication protocols, and cost-effectiveness, they can only be used in applications compatible with the polymer's operation conditions. For example, they are not or hardly suited for chemical reactions in the harsh environments such as high temperature, high pressure, and corrosive reactants. Metallic and ceramic materials are better suited under such harsh operating conditions. Metals, in particular, are attractive because they are not only compatible with conventional machining processes (thus easier to make connections) but also potentially provide better performance and long-term stability due to their superior mechanical, thermal, and electrical properties.

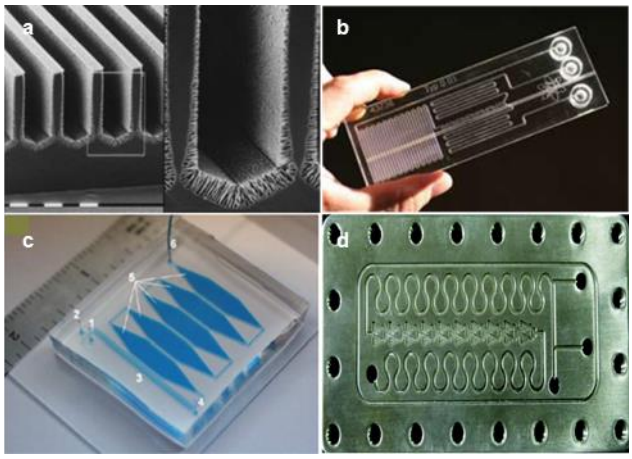

Figure 1.2 (a) porous silicon microreacto for lab-on-chip based flow through catalytical processes as well as continuous[19]; (b) a glass microreactor on a chip for chemical reaction[20]; (c) PDMS microreactor used as microfluidics channel in radiopharmaceutical chemistry[21] ; (d) metal microreactor for PMMA nanoparticles fabrication[22]

1.1.1.2 Fabrication approaches to microreactors

A number of fabrication approaches have been employed for the construction of microreactors. Depending on the reactor materials, different methods have been chosen including MEMS fabrication techniques, precision machining, laser ablation, hot embossing, nanoimprinting, etc.[23–25] MEMS fabrication techniques such as photolithography, wet and dry etching, deposition, and bonding[26–28], are perhaps most widely used in making microreactors as most microreactors are based on silicon, glass, and polymers. However, these fabrication techniques have some weaknesses. First, the MEMS fabrication typically requires cleanroom environments as well as expensive equipment, significantly increasing a production cost. Next, microreactor structures generated from MEMS-based technology cannot have arbitrary 3D shapes because the technology has been developed on a flat surface and add or subtract materials in the direction perpendicular to the substrate, known as 2.5 dimensional. In addition, as mentioned earlier, incompatibility with conventional machining, robust fluidic interconnects are hard to be made for Si or glass-based microreactors. This limitation in design freedom and fluidic connections can be somewhat lifted if metal is considered as a base material for microreactors. Most manufacturing technologies for metals rely on either subtractive approaches such as lathing, milling, drilling, etc., or molding/casting approaches if the melting point is relatively low. Even though precision machining using 5-axis CNC machines or electrical discharge machining can nowadays produce small external features that are well below a few hundred microns, it is extremely difficult to produce internal features with the similar size and complexity. In addition, these precision machining approaches cannot fully address the limitation of the overall geometric complexities. These challenges for microstructure fabrication of metallic materials can be overcome via a

recently burgeoning manufacturing process, so called additive manufacturing (AM) or also known as metal 3D printing.

1.1.2 Metal Additive Manufacturing (AM)

Additive manufacturing (AM) is another name of 3D printing processes: 3D printing is more commonly referred to a process for plastic/polymeric parts and AM is for metals and ceramics. This process doesn't require a careful and detailed analysis of the part geometry to determine how features arrange the order, what tools and process can be used, and what additional information need to be added to complete the part[29,30]. Basically, the principle of the AM processes is straightforward; that is, the part can be fabricated directly without complicated processes using a model initially designed through a three-dimensional computer-aided design (3D CAD) program. AM is the process of joining materials to make objects from CAD model data, usually in a layer-by-layer manner, rather than removing materials from parts: in other words, converting from the virtual CAD description to the physical resultant part.

Various AM technologies were originally developed in the late 1980's and early 1990's as a prototyping tool, but have recently regained its popularities in both the academic community and the business world. AM can revolutionize many sectors in manufacturing by offering the advantages of reducing component build time, material waste, manufacturing cost and increasing energy efficiency. Furthermore, AM has the potential to simplify the product design that is difficult to be created from traditional subtractive manufacturing process. In terms of manufacturing technology, AM is also known as additive fabrication, free form fabrication, layer manufacturing, rapid prototyping and "3D printing", which are also in use. A number of steps involved in fabricating the physical parts in the AM process include CAD, STL file conversion, file transfer

to the AM machine, machine set-up, part building, removal and post-process, which are generally applied to all AM technologies.

Metal AM gains enormous popularities in the past few years and is often dubbed as a game-changing technology or third-industrial revolution for the following reasons: (1) the diversity of products (or mass customization), (2) the complexity in shape, and (3) production cost independent of production scale without significant waste. 3D printing directly connects design and manufacturing activities. Thus, many designs perceived, including any number of variations as needed, can be directly fed into 3D printing, enabling mass customization of producing many variations of a product. This is quite different from mass production where dies, molds and tools are needed to produce a massive number of parts in consistent quality. Many features such as cavities and tortuous internal channels that are impossible to be made by traditional manufacturing techniques can be manufactured with AM. The cost of production is independent of the quantity of production, meaning the cost per part is the same whether making one, thousands or millions. We will harness these advantages in fabricating the proposed meso-scale devices, mainly microreactors.

According to ASTM F42 Committee on Additive Manufacturing[31], metal AM has been classified into four main categories: Powder Bed Fusion (PBF), Direct Energy Deposition (DED), Sheet Lamination, and Binder Jet Printing (BJP). In PBF (e.g., electron beam melting (EBM), selective laser melting (SLM), and selective laser sintering (SLS)), powder is consolidated on each powder layer locally with directed energy (electron beam or laser). In other words, a part is fabricated by consolidating a small segment at a time. Each segment experiences a complex thermal history consisting of directed heat input and heat extraction, which are affected by the state of neighboring segments and chamber environment. In addition, while neighboring segments are

being heated, each segment undergoes repeated partial melting and heat treatment, rapid solidification, and solid state phase transformations. Rapid solidification can induce the formation of metastable phases and, in some cases, heat is extracted directionally, resulting in preferred directional grain growth[32,33]. The cooling rate is reported to be relatively high (up to 10^3 –10^4 K/s for some metals), which leads to non-equilibrium microstructures. Vilaro et al.[34] reported the SLS processing of Ti-6Al-4V exhibiting a strong texture as a result of epitaxial growth and the strong anisotropy attributed to the reduced integrity of the resulting parts. These numerous phenomena result in a complex and heterogeneous microstructure in the final part. In addition, some processing defects such as micro-porosity and rough surface finish affect the final integrity of the produced part, resulting in parts with inconsistent performances.

Many researchers have developed novel microchannels, chemical microreactor, gas sensors and systems in metal using AM approach. Tuchinskiy *et al*. presented a low-cost manufacturing process, capable of controlling the geometry and properties and carrying out the net-shape fabrication for metal and ceramic micro-honeycombs with parallel microchannels[35]. This work combines the powder and binder in the shell and places the mixture of binder and a channel-forming filler in the core and after re-extruding the shell and core, debinding and sintering were adopted to obtain the final micro-honeycombs[35]. Uhlmann *et al.* fabricated the titanium alloy used for aircraft components using the SLM technology. TiAl6V4 was adopted as additive manufacture components and showed enormous potentials in improvement of quality and mechanical properties of the titanium alloy parts by SLM[37]. Ladd *et al*. described a method to direct-write 3D liquid microcomponents at room temperature and showed it is possible to direct-write a low viscosity liquid metal into a variety of stable free-standing 3D microstructures, which is important to print metal with properties of soft, stretchable and shape reconfigurable[38].

1.1.2.1 Binder Jet Printing (BJP)

Among various metal powder based AM systems, binder jetting printing (BJP) methods are used in our project[29,39,40]. BJP is a 3D printing process which injects the binder phase onto a powder bed to form a physical part. The standard BJP process is shown in Figure 1.3[40]. First, binder droplets are jetted from a nozzle to form spherical agglomerates of binder liquid and delivered into the target area of metal powder particles in the build bed to bind themselves as well as to the previously printed layer. The build bed is then lowered, allowing a roller to spread a new layer of metal powder from the powder bed. These steps are repeated until the part is completed. Many post-processing steps are involved after printing to improve the mechanical properties of the printed part. First, the part is removed from the build bed and transferred to an oven to temporarily cure the binder phase for minimal structural support. Excessive (unbound) powder particles within and around the part are carefully removed using a brush or by blowing air. The part is now transferred to a regular convection oven to burn off the polymeric binder at low temperature (around 460ºC) followed by vacuum sintering to consolidate/densify powder particles in the part and improve its strength. Alternatively, the part after the binder burn-out process remains highly porous and can be sintered in a reactive environment to tune the electrical or other physical properties of the printed part. After these steps, we obtain either a mechanically strong metal part suitable for fluidic and microreactor applications or a metal/metal-oxide heterogeneous structure whose properties can be used for novel applications.

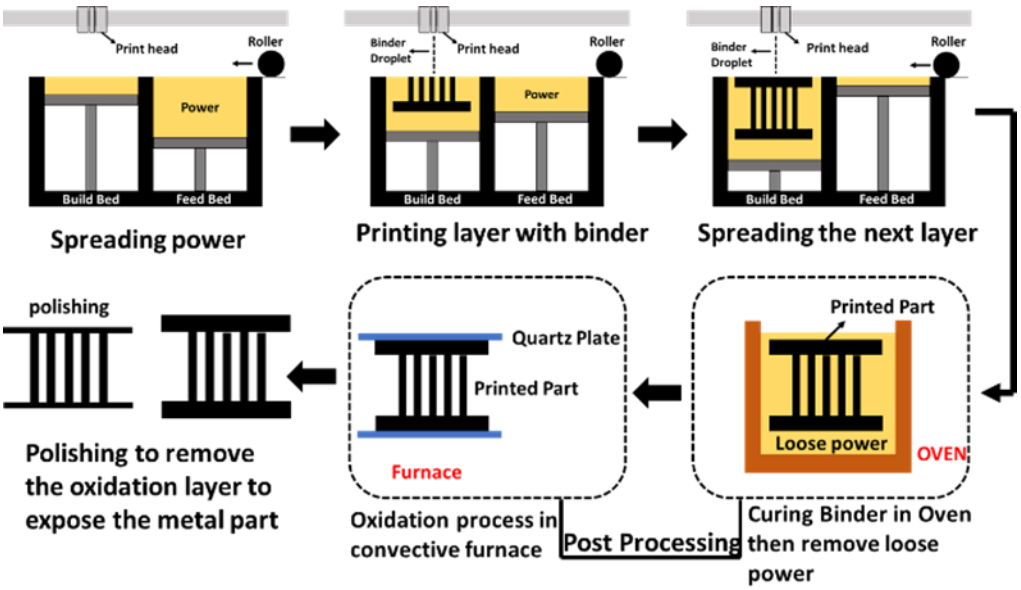

Figure 1.3 The schematic procedure of Binder Jet Printing (BJP) and post processing

1.1.3 Microreactor applications of BJP parts

1.1.3.1 Micro preconcentrator

With the fast development of miniaturization and microfabrication technologies, researchers have developed a wide range of gas sensors to detect gaseous components in ambient or other media. These devices are used in air monitoring for environmental applications, explosive/illicit and harmful chemical detection for security/safety and industrial applications, and breath analysis for medical diagnosis. In many cases, the gaseous compounds of interest are present in extremely low concentrations. The challenge is that many gas detectors themselves do not possess sufficient sensitivity and selectivity to be useful in such situation. Despite tremendous efforts in improving the minimum detection limit, very different approaches have been proposed to measure such a low concentration of gases. One approach is to implement a gas preconcentrator and couple it with GC system[41–44]. A preconcentrator (PC) is the device that can collect the target

samples over a period of time and then release highly concentrated analytes by thermal desorption in a relative narrow period (i.e., smaller volume) for chemical analysis.

Traditionally, these sampling processes of gaseous analytes are conducted using relatively large-size instruments like thermal desorption units (TDUs) and complex procedures like solid-phase microextraction (SPME). These systems are bulky and consume large power, unsuitable for portable applications. A number of efforts have been made to miniaturize PCs and develop so called microscale PCs (or micro-PCs) for the real- time detection with fast response and low power consumption as well as portability[45–47]. Here, we consider micro-PCs as a sort of microreactors because it involves the delivery of gaseous species, heat and mass transfer, and medium-to-high temperature operation. The majorities of micro-PCs are built on silicon using MEMS technologies, and as discussed earlier, Si-based microreactors (created by MEMS fabrication processes) suffer from the lack of robust fluidic interconnects and low device fabrication yield. In this dissertation, we propose to utilize AM, specifically BJP, to produce stainless steel PCs.

1.1.3.2 Functionally graded materials (FGM)

FGMs are advanced engineering materials in which the elemental composition or microstructure progressively varies as a function of position resulting in the gradation in the material properties. They are highly advantageous when the service conditions of a component change with position (or gradient loading) and thus, to become a highly effective media, the material requirements also locally vary accordingly. A notable example includes thermal barrier materials in extreme-environmental applications such as aerospace or nuclear power generation[48], where the structures are exposed to extremely gradient thermal loading within the part. Another example is an orthopedic or dental implant application in which the main body has high strength

and lightweight but its surface should be biocompatible and wear and corrosion resistant[49,50]. Numerous techniques have been developed to fabricate FGMs with compositional gradients, including chemical vapor deposition[51,52], thermal spraying[53,54], combustion synthesis[55,56], and other deposition methods[57,58]. These FGMs are in the form of surface coatings, well supporting gradients over length scales of less than 1 mm. However, these techniques cannot be implemented to fabricate any bulk FGM material made of ceramics and metals[59]. Metal/ceramic FGMs with the compositional variation over larger length scales entail completely different fabrication methods such as centrifugal casting[60,61], tape or slip casting[62–65], spark plasma sintering[66–68], and powder metallurgy[69–71]. A significant amount of research efforts have been made to address the material and processing incompatibilities (due to the thermal shrinkage or expansion mismatch) and residual stress issues. These bulk FGM structures are, without 3D printing technology, too simple in their shape and nearly impossible to attain more complex features and overall shapes that many modern engineering applications require. Recently, AM has received an increasing attention as a promising technique to create near net-shaped FGM structures[69]. Among the various kinds of AM, the directed energy deposition (DED) method, in which metal powder is fed into the melt pool under a moving laser[72] is most widely employed for the preparation of FGMs because the variation of powder composition among layers can be easily achieved by two or more powder feeders. The elemental composition and mechanical properties of such DED-enabled FGMs have been investigated for the various graded metal alloys from Ti-6Al-4V to pure V, 304L stainless steel (SS) to Invar 36[69], Ti-6Al-4V to 304L SS[73], 304L SS to Inconel 625[74], and finally Ti-6Al-4V to Invar 36[75]. The majority of these works are, however, focused on the feasibility of achieving gradual compositional changes in metals without any particular application in mind. The powder

bed systems such as BJP are ideal for the mesoscale fabrication meeting the accuracy and tolerance required for the proposed applications.

1.2 Nanosphere lithography combined with soft lithography

1.2.1 Nanosphere lithography

Nanosphere lithography (NSL) offers a simple and low-cost approach to creating periodic nanostructures or nanoparticles over a relatively large area[76] and provides design flexibility as the density and size of the NSL-derived patterns can be tuned at a reasonable precision- a feature that is not commonly found in other inexpensive bottom-up methods[77]. NSL produce ordered arrays of nanometer-sized polymer or silica spheres that generally serve as lithographic masks for further deposition or etching processes. Numerous methods have been developed to obtain the nanosphere arrays including Langmuir-Blodogett, dip coating, spin coating, solvent evaporation, convective assembly, and air-water interface[78–81].

Despite an extraordinary number of the papers that report ingenious methods to adapt/modify NSL for generating a wide variety of nanopatterns, we identify a few challenges that are not easily met by the existing NSL-derived methods. Those limitations include (1) difficulty in producing high-quality hexagonal array of metallic nanodots with the same arrangement of the original nanosphere array, (2) lack of a facile and robust method to create highly-ordered, well-separated non-close-packed hexagonal nanosphere array with a pitch much larger than the original nanosphere diameter, and (3) lack of any approach to producing nanosphere arrays with multiple yet controlled pitches across the same substrate. Here we aim to lay out a few novel fabrication methods that address each of the abovementioned challenges.

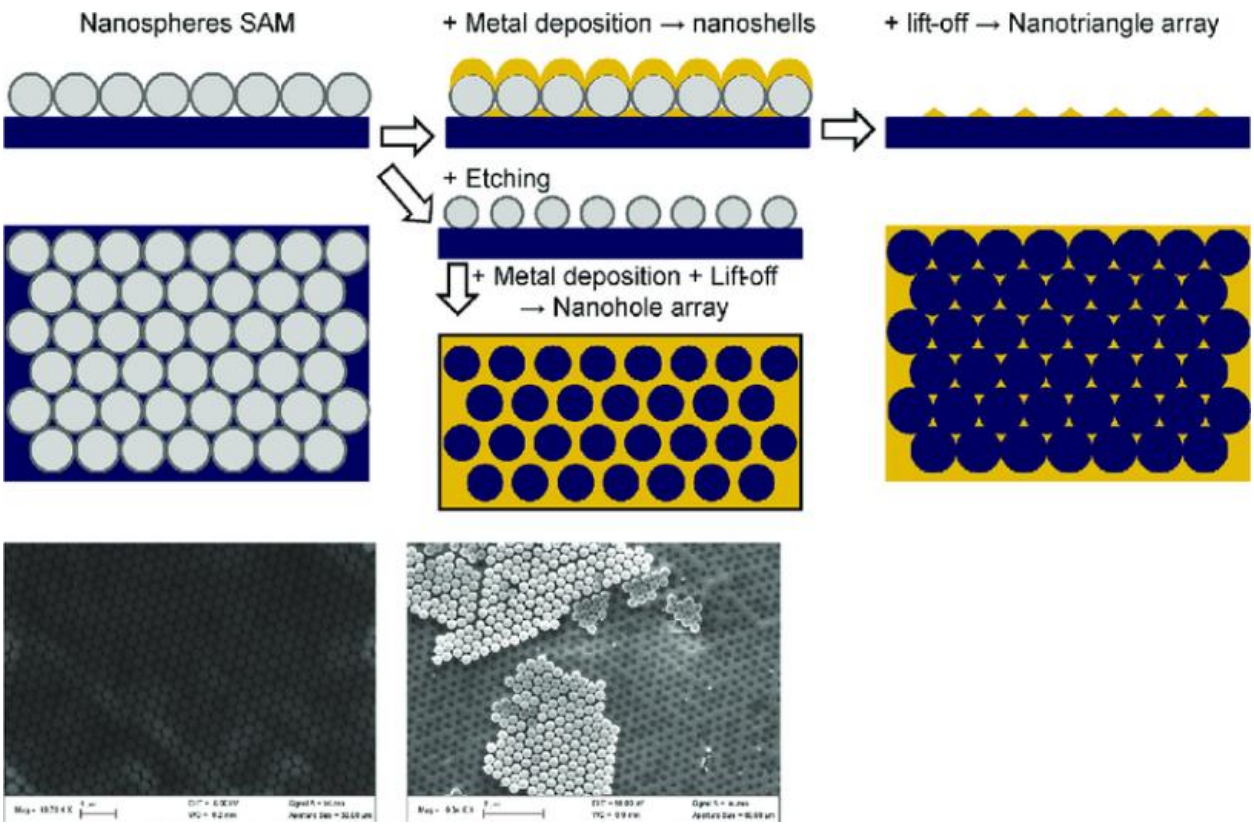

Figure 1.4 Nanosphere lithography process (NSL) to produce the nanoholes or nanotriangle arrays[82]

1.2.2 Soft lithography

The concept of soft lithography was introduced in 1988 by Whiteside's group at Harvard[83]. It is an alternative technique for nano- and micro-fabrication involving the inverse replication of a mold with the aid of elastomeric polymers. Specifically, soft lithography utilizes an elastomer, such as polydimethylsiloxane (PDMS), and makes use of that mold to create features with geometries defined by the mold's relief structure. When compared to other nanofabrication approaches, soft lithography offers several advantages, including low cost, simplicity, and applicability to soft materials[84]. Various modified versions of soft lithography have been also proposed to create patterns well beyond what the technique was originally intended. In particular, in conjunction with NSL, soft lithography can pick up and transfer nanosphere patterns from the

originally-assembled surface to any target substrate. During the transfer process, the elastomeric membrane whose surface is covered with nanospheres can be stretched to increase the pitch of the nanosphere array, which will serve as a key technique in our study.

1.3 Research objectives and scopes of the dissertation

In chapter 2, we address issues associated with fabricating and operating Si-based micro-PCs by developing stainless steel (SS) PCs. Binder jet printing (BJP), one of the metal AM processes, was utilized to make SS PCs with submillimeter internal features. Normally, parts printed by BJP are highly porous and thus often infiltrated with low melting point metal. By adding to SS316 powder sintering additives such as boron nitride (BN), which reduces the liquid temperature, we produce near full-density SS PCs at sintering temperatures much lower than the SS melting temperature and importantly without any measurable shape distortion. Conversely, the SS PC without BN remains porous after the sintering process and unsuitable for fluidic applications. Since the SS parts, unlike Si, are compatible with machining, they can be modified to work with commercial compression fitting. The PC structures as well as the connection with the fitting are leak-free with relatively high operating pressures. A flexible membrane heater along with a resistance-temperature detector is integrated with the SS PCs for thermal desorption. The proof-of-concept experiment demonstrates that the SS PC can preconcentrate and inject 0.6% headspace toluene as an in-line injector to enhance the detector's response.

In chapter 3, we propose metal/metal-oxide functionally-gradient materials (FGM) with tunable electrical properties using the combination of BJP and selective reactive sintering (SRS). Metal parts built by BJP are highly porous, allowing reactants to easily diffuse into the structures. By introducing oxygen during sintering, we can convert metal to metal oxide in a powder level

and thus locally modulate the structure's electrical resistivity. Local control of the electrical properties can be accomplished by the part geometry and placing diffusion barriers. We here show that more than 6 orders of magnitude difference in electrical resistivity can be realized by the proposed approach. Since only the certain region of the structure is more resistive than the others, it enables the construction of highly efficient resistive heating element in which electrothermal conversion takes place at the desired location within the structure. As a proof-of-the-concept device, we create a SS microreactor with an array of posts that serve as heating elements. Heater performance by structural Joule heating by the microreactor is compared to that of the external heating theoretically and experimentally, demonstrating that the proposed microreactor structure with the BJP-SRS process delivers thermal energy more efficiently to a fluid (i.e., more efficient heat exchanger). The conversion of metal to metal/metal oxide heterostructure also induces a large difference in temperature coefficient of resistance (TCR), increasing its absolute value by two to three orders of magnitude. This enables the microreactor to measure the temperature and flow rate of the fluid by simply monitoring the structure's resistance, i.e., used as a built-in resistance temperature detector (RTD). These types of multifunctional microreactors that can survive from medium-to-high temperature operating conditions have not been reported to our best of knowledge. We believe the proposed fabrication scheme can be applied to other application areas and expand the scope of metal AM technologies.

Chapter 4 addresses the key challenge inherent to NSL-derived fabrication, namely array pitch control without disturbing the original hexagonal arrangement. We present a facile and robust method to create a highly ordered, well-separated, non-close-packed monolayer of colloidal nanospheres using soft-lithographic lift-off and transfer-printing techniques combined with radial stretching of an elastomer. A custom-made elastomer enables the elastomer substrate

(onto which the original nanosphere array is transferred) to expand isotropically and allows the pitch of the non-close-packed nanosphere array to be accurately controlled while preserving the original hexagonal symmetry. A pitch increase as large as 213% can be achieved in a single stretch-and-transfer step, which is a significant improvement from the existing technique relying on solvent swelling. These nanosphere arrays on the stretched elastomer substrate can be transferred to various target substrates. The effect of the stretching direction on the resulting lattice structure will be investigated for uniaxial, biaxial, and radial stretching scenarios. Finally, the optical response of the pitch controlled nanosphere arrays in the target substrates (e.g., Si, glass, PET) will be studied, and it will be shown that the patterns can be used as the etching mask to produce a mold and replica for further applications.

In chapter 5, a highly ordered hexagonal array of metallic nanodots with original arrangement was fabricated by nanosphere lithography combined with a facile double lift-off process. This approach overcomes the limitation of traditional lift off process with metal which is the surface diffusion to metal on the top of surface so that well-defined metallic nanodots were created. Here, the double lift-off process enables two consecutive metal lift-off process. The first lift-off and the second lift-off process adopted the different metal as etching mask to create re-entrant sidewall profile by sacrificial etching layer of the underlying metal layer to improve the yield. This ordered metallic nanodot array also serves as an etch mask in reactive ion etching (RIE) and is used to produce a large-area, hexagonal array of silicon nanowires exhibiting highly anti-reflecting structures in almost all UV and visible wavelengths.

REFERENCES

REFERENCES

1. Yi, S. J., Park, J. M., Chang, S.-C. & Kim, K. C. Design and validation of a uniform flow microreactor. *J. Mech. Sci. Technol.* **28**, 157–166 (2014).

2. Amii, H., Nagaki, A. & Yoshida, J. Flow microreactor synthesis in organo-fluorine chemistry. *Beilstein J. Org. Chem.* **9**, 2793–2802 (2013).

3. Groppi, G. & Tronconi, E. Design of novel monolith catalyst supports for gas/solid reactions with heat exchange. *Chem. Eng. Sci.* **55**, 2161–2171 (2000).

4. Reuse, P., Renken, A., Haas-Santo, K., Görke, O. & Schubert, K. Hydrogen production for fuel cell application in an autothermal micro-channel reactor. *Chem. Eng. J.* **101**, 133–141 (2004).

5. Higgins, J. A. *et al.* A handheld real time thermal cycler for bacterial pathogen detection. *Biosens. Bioelectron.* **18**, 1115–1123 (2003).

6. Daniel, J. H. *et al.* Silicon microchambers for DNA amplification. *Sens. Actuators Phys.* **71**, 81–88 (1998).

7. Micro reactor technology Market Report- Global 2027. Available at: https://www.marketresearchfuture.com/reports/micro-reactor-technology-market-1128. (Accessed: 20th April 2019)

8. Liu, D. *et al.* A Versatile and Robust Microfluidic Platform Toward High Throughput Synthesis of Homogeneous Nanoparticles with Tunable Properties. *Adv. Mater.* **27**, 2298–2304 (2015).

9. Liu, D.-M., Chen, J. & Shi, Y.-P. An online immobilized α-glucosidase microreactor for enzyme kinetics and inhibition assays. *RSC Adv.* **5**, 56841–56847 (2015).

10. Martínez-Cisneros, C. S., Pedro, S. G., Puyol, M., García-García, J. & Alonso-Chamarro, J. Design, fabrication and characterization of microreactors for high temperature syntheses. *Chem. Eng. J.* **211**–**212**, 432–441 (2012).

11. Jensen, K. F. Flow chemistry—Microreaction technology comes of age. *AIChE J.* **63**, 858–869 (2017).

12. Shang, M., Noël, T., Su, Y. & Hessel, V. Kinetic study of hydrogen peroxide decomposition at high temperatures and concentrations in two capillary microreactors. *AIChE J.* **63**, 689–697 (2017).

13. Ren, W. *et al.* Whole ceramic-like microreactors from inorganic polymers for high temperature or/and high pressure chemical syntheses. *Lab. Chip* **14**, 779–786 (2014).

14. Zilio, C., Sola, L., Damin, F., Faggioni, L. & Chiari, M. Universal hydrophilic coating of thermoplastic polymers currently used in microfluidics. *Biomed. Microdevices* **16**, 107–114 (2014).

15. Kucuk, I. & Edirisinghe, M. Microfluidic preparation of polymer nanospheres. *J. Nanoparticle Res.* **16**, 2626 (2014).

16. Halldorsson, S., Lucumi, E., Gómez-Sjöberg, R. & Fleming, R. M. T. Advantages and challenges of microfluidic cell culture in polydimethylsiloxane devices. *Biosens. Bioelectron.* **63**, 218–231 (2015).

17. Fouillet, Y. *et al.* Stretchable Material for Microfluidic Applications. *Proceedings* **1**, 501 (2017).

18. Azouz, A. B., Murphy, S., Karazi, S., Vázquez, M. & Brabazon, D. Fast Fabrication Process of Microfluidic Devices Based on Cyclic Olefin Copolymer. *Mater. Manuf. Process.* **29**, 93–99 (2014).

19. Porous silicon microreactors | Biomedical Engineering. Available at: http://bme.lth.se/research-pages/nanobiotechnology-and-lab-on-a-chip/research/earlier-projects/porous-silicon-microreactors/. (Accessed: 20th April 2019)

20. Microreactors: Discovery, Development and Chemical Engineering Opportunities. (2009). Available at: https://www.aiche.org/academy/webinars/microreactors-discovery-development-and-chemical-engineering-opportunities. (Accessed: 20th April 2019)

21. Pascali, G., Watts, P. & Salvadori, P. A. Microfluidics in radiopharmaceutical chemistry. *Nucl. Med. Biol.* **40**, 776–787 (2013).

22. Dobhal, A., Kulkarni, A., Dandekar, P. & Jain, R. A microreactor-based continuous process for controlled synthesis of poly-methyl-methacrylate-methacrylic acid (PMMA) nanoparticles. *J. Mater. Chem. B* **5**, 3404–3417 (2017).

23. Wilson, M. E. *et al.* Fabrication of circular microfluidic channels by combining mechanical micromilling and soft lithography. *Lab. Chip* **11**, 1550–1555 (2011).

24. Konstantinou, D., Shirazi, A., Sadri, A. & Young, E. W. K. Combined hot embossing and milling for medium volume production of thermoplastic microfluidic devices. *Sens. Actuators B Chem.* **234**, 209–221 (2016).

25. Acikgoz, C., Hempenius, M. A., Huskens, J. & Vancso, G. J. Polymers in conventional and alternative lithography for the fabrication of nanostructures. *Eur. Polym. J.* **47**, 2033–2052 (2011).

26. Kim, T. & Kwon, S. Design, fabrication and testing of a catalytic microreactor for hydrogen production. *J. Micromechanics Microengineering* **16**, 1760 (2006).

27. Martínez-Cisneros, C. S., Pedro, S. G., Puyol, M., García-García, J. & Alonso-Chamarro, J. Design, fabrication and characterization of microreactors for high temperature syntheses. *Chem. Eng. J.* **211**–**212**, 432–441 (2012).

28. Tiggelaar, R. M. *et al.* Fabrication of a high-temperature microreactor with integrated heater and sensor patterns on an ultrathin silicon membrane. *Sens. Actuators Phys.* **119**, 196–205 (2005).

29. *Additive Manufacturing Technologies - 3D Printing, Rapid | Ian Gibson | Springer*.

30. Kruth, J.-P., Leu, M. C. & Nakagawa, T. Progress in Additive Manufacturing and Rapid Prototyping. *CIRP Ann.* **47**, 525–540 (1998).

31. Committee F42 on Additive Manufacturing Technologies. Available at: https://www.astm.org/COMMITTEE/F42.htm. (Accessed: 17th April 2019)

32. Liu, S. & Shin, Y. C. Additive manufacturing of Ti6Al4V alloy: A review. *Mater. Des.* **164**, 107552 (2019).

33. Trevisan, F. *et al.* On the Selective Laser Melting (SLM) of the AlSi10Mg Alloy: Process, Microstructure, and Mechanical Properties. *Materials* **10**, (2017).

34. Vilaro, T., Colin, C. & Bartout, J. D. As-Fabricated and Heat-Treated Microstructures of the Ti-6Al-4V Alloy Processed by Selective Laser Melting. *Metall. Mater. Trans. A* **42**, 3190–3199 (2011).

35. Tuchinskiy, L. Novel Manufacturing Process for Metal and Ceramic Microhoneycombs. *Adv. Eng. Mater.* **10**, 219–222 (2008).

36. Uhlmann, E., Kersting, R., Klein, T. B., Cruz, M. F. & Borille, A. V. Additive Manufacturing of Titanium Alloy for Aircraft Components. *Procedia CIRP* **35**, 55–60 (2015).

37. Ladd, C., So, J.-H., Muth, J. & Dickey, M. D. 3D Printing of Free Standing Liquid Metal Microstructures. *Adv. Mater.* **25**, 5081–5085 (2013).

38. Frazier, W. E. Metal Additive Manufacturing: A Review. *J. Mater. Eng. Perform.* **23**, 1917–1928 (2014).

39. Do, T., Kwon, P. & Shin, C. S. Process development toward full-density stainless steel parts with binder jetting printing. *Int. J. Mach. Tools Manuf.* **121**, 50–60 (2017).

40. James, F. *et al.* Development of a MEMS Preconcentrator for Micro-gas Chromatography Analyses. *Procedia Eng.* **87**, 500–503 (2014).

41. Seo, J. H., Kim, S. K., Zellers, E. T. & Kurabayashi, K. Microfabricated passive vapor preconcentrator/injector designed for microscale gas chromatography. *Lab. Chip* **12**, 717–724 (2012).

42. Tian, W.-C., Pang, S. W., Lu, C.-J. & Zellers, E. T. Microfabricated preconcentrator-focuser for a microscale gas chromatograph. *J. Microelectromechanical Syst.* **12**, 264–272 (2003).

43. Tian, W. C., Chan, H. K. L., Lu, C. J., Pang, S. W. & Zellers, E. T. Multiple-stage microfabricated preconcentrator-focuser for micro gas chromatography system. *J. Microelectromechanical Syst.* **14**, 498–507 (2005).

44. Li, S., Day, J. C., Park, J. J., Cadou, C. P. & Ghodssi, R. A fast-response microfluidic gas concentrating device for environmental sensing. *Sens. Actuators Phys.* **136**, 69–79 (2007).

45. Alfeeli, B., Cho, D., Ashraf-Khorassani, M., Taylor, L. T. & Agah, M. MEMS-based multi-inlet/outlet preconcentrator coated by inkjet printing of polymer adsorbents. *Sens. Actuators B Chem.* **133**, 24–32 (2008).

46. Voiculescu, I., Zaghloul, M. & Narasimhan, N. Microfabricated chemical preconcentrators for gas-phase microanalytical detection systems. *TrAC Trends Anal. Chem.* **27**, 327–343 (2008).

47. Zinkle, S. J. & Was, G. S. Materials challenges in nuclear energy. *Acta Mater.* **61**, 735–758 (2013).

48. Oshida, Y., Tuna, E. B., Aktören, O. & Gençay, K. Dental Implant Systems. *Int. J. Mol. Sci.* **11**, 1580–1678 (2010).

49. Navarro, M., Michiardi, A., Castaño, O. & Planell, J. . Biomaterials in orthopaedics. *J. R. Soc. Interface* **5**, 1137–1158 (2008).

50. Elkasabi, Y., Lahann, J. & Krebsbach, P. H. Cellular transduction gradients via vapor-deposited polymer coatings. *Biomaterials* **32**, 1809–1815 (2011).

51. Design of SiC/C Functionally Gradient Material and Its Preparation by Chemical Vapor Deposition. Available at: https://www.jstage.jst.go.jp/article/jcersj1988/97/1125/97_1125_539/_article/-char/en. (Accessed: 17th April 2019)

52. Sioh, E. L. & Tok, A. I. Y. Functionally Graded Materials using Plasma Spray with Nano Structured Ceramic. *J. Phys. Conf. Ser.* **419**, 012048 (2013).

53. Majumdar, J. D. & Manna, I. Development of Functionally Graded Coating by Thermal Spray Deposition. *Therm. Sprayed Coat. Their Tribol. Perform.* 121–162 (2015). doi:10.4018/978-1-4666-7489-9.ch005

54. Niedzialek, S. E., Stangle, G. C. & Kaieda, Y. Combustion-synthesized functionally gradient refractory materials. *J. Mater. Res.* **8**, 2026–2034 (1993).

55. Stangle, G. C. & Miyamoto, Y. FGM Fabrication by Combustion Synthesis. *MRS Bull.* **20**, 52–53 (1995).

56. Sattar, N. *A Review For Functionally Gradient Materials Manufacturing And Useful Application*. (2018).

57. Suryakumar, S. & Somashekara, M. A. Manufacturing of functionally gradient materials by using weld-deposition. in *Proceedings of the 1st International Joint Symposium on Joining and Welding* (ed. Fujii, H.) 505–508 (Woodhead Publishing, 2013). doi:10.1533/978-1-78242-164-1.505

58. Chmielewski, M. & Pietrzak, K. Metal-ceramic functionally graded materials – manufacturing, characterization, application. *Bull. Pol. Acad. Sci. Tech. Sci.* **64**, 151–160 (2016).

59. Rajan, T. P. D., Pillai, R. M. & Pai, B. C. Centrifugal casting of functionally graded aluminium matrix composite components. *Int. J. Cast Met. Res.* **21**, 214–218 (2008).

60. Xie, Y., Liu, C., Zhai, Y., Wang, K. & Ling, X. Centrifugal casting processes of manufacturing in situ functionally gradient composite materials of Al-19Si-5Mg alloy. *Rare Met.* **28**, 405–411 (2009).

61. Moya, J. S., Sánchez-Herencia, A. J., Requena, J. & Moreno, R. Functionally gradient ceramics by sequential slip casting. *Mater. Lett.* **14**, 333–335 (1992).

62. Navarro, A., Whatmore, R. W. & Alcock, J. R. Preparation of Functionally Graded PZT Ceramics Using Tape Casting. *J. Electroceramics* **13**, 413–415 (2004).

63. Yeo, J.-G., Jung, Y.-G. & Choi, S.-C. Design and microstructure of ZrO2/SUS316 functionally graded materials by tape casting. *Mater. Lett.* **37**, 304–311 (1998).

64. Yeo, J.-G., Jung, Y.-G. & Choi, S.-C. Zirconia-stainless steel functionally graded material by tape casting. *J. Eur. Ceram. Soc.* **18**, 1281–1285 (1998).

65. Fujii, T., Tohgo, K., Isono, H. & Shimamura, Y. Fabrication of a PSZ-Ti functionally graded material by spark plasma sintering and its fracture toughness. *Mater. Sci. Eng. A* **682**, 656–663 (2017).

66. Chaubey, A. K. *et al.* Fabrication and characterization of W-Cu functionally graded material by spark plasma sintering process. *Fusion Eng. Des.* **135**, 24–30 (2018).

67. Feng, H., Meng, Q., Zhou, yu & Jia, D. Spark plasma sintering of functionally graded material in the Ti–TiB 2 –B system. *Mater. Sci. Eng. -Struct. Mater. Prop. Microstruct. Process. - MATER SCI ENG -STRUCT MATER* **397**, 92–97 (2005).

68. Reichardt, A. Additive Manufacturing of Metal-based Functionally Graded Materials. (UC Berkeley, 2017).

69. Articek, U., Milfelner, M. & Anzel, I. Synthesis of functionally graded material H13/Cu by LENS technology. *Adv. Prod. Eng. Manag.* **8**, 169–176 (2013).

70. Nemat-Alla, M., Ata, M., Ragab, M. & Khair-Eldeen, W. Powder Metallurgical Fabrication and Microstructural Investigations of Aluminum/Steel Functionally Graded Material. *Mater Sci Appl* **2**, (2011).

71. Bhavar, V., Kattire, P., Thakare, S., patil, S. & Singh, R. A Review on Functionally Gradient Materials (FGMs) and Their Applications. *IOP Conf. Ser. Mater. Sci. Eng.* **229**, 012021 (2017).

72. Bobbio, L. D. *et al.* Characterization of a functionally graded material of Ti-6Al-4V to 304L stainless steel with an intermediate V section. *J. Alloys Compd.* **742**, 1031–1036 (2018).

73. Carroll, B. E. *et al.* Functionally graded material of 304L stainless steel and inconel 625 fabricated by directed energy deposition: Characterization and thermodynamic modeling. *Acta Mater.* **108**, 46–54 (2016).

74. Bobbio, L. D. *et al.* Additive manufacturing of a functionally graded material from Ti-6Al-4V to Invar: Experimental characterization and thermodynamic calculations. *Acta Mater.* **127**, 133–142 (2017).

75. Ho, Y.-H. *et al.* Transparent and conductive metallic electrodes fabricated by using nanosphere lithography. *Org. Electron.* **12**, 961–965 (2011).

76. Yeom, J., Ratchford, D., Field, C. R., Brintlinger, T. H. & Pehrsson, P. E. Decoupling Diameter and Pitch in Silicon Nanowire Arrays Made by Metal-Assisted Chemical Etching. *Adv. Funct. Mater.* **24**, 106–116 (2014).

77. Jang, D. *et al.* Force-assembled triboelectric nanogenerator with high-humidity-resistant electricity generation using hierarchical surface morphology. *Nano Energy* **20**, 283–293 (2016).

78. Colson, P., Henrist, C. & Cloots, R. Nanosphere Lithography: A Powerful Method for the Controlled Manufacturing of Nanomaterials. *Journal of Nanomaterials* (2013). doi:10.1155/2013/948510

79. Zhang, C., Cvetanovic, S. & Pearce, J. M. Fabricating ordered 2-D nano-structured arrays using nanosphere lithography. *MethodsX* **4**, 229–242

80. Sirotkin, E., Apweiler, J. D. & Ogrin, F. Y. Macroscopic Ordering of Polystyrene Carboxylate-Modified Nanospheres Self-Assembled at the Water−Air Interface. *Langmuir* **26**, 10677–10683 (2010).

81. Gillibert, R., Qi Huang, J., Zhang, Y., Ling Fu, W. & Lamy de la Chapelle, M. Explosive detection by Surface Enhanced Raman Scattering. *TrAC Trends Anal. Chem.* **105**, (2018).

82. Xia, Y. & Whitesides, G. M. Soft Lithography. *Annu. Rev. Mater. Sci.* **28**, 153–184 (1998).

83. Qin, D., Xia, Y. & Whitesides, G. M. Soft lithography for micro- and nanoscale patterning. *Nat. Protoc.* **5**, 491–502 (2010).

CHAPTER 2

A BINDER JET PRINTED, STAINLESS STEEL PRECONCENTATOR AS AN IN-LINE INJECTOR OF VOLATILE ORGANIC COMPOUNDS

2.1 Introduction

Monitoring volatile organic compounds (VOCs) plays an import role in many application fields such as environment monitoring, industrial safety, plant health, and human disease diagnosis[1–8]. A state-of-the-art approach for VOC analysis is gas chromatography[9] (GC) coupled with mass spectrometer (MS)[10] or other GC detectors thanks to their ultrahigh sensitivity, selectivity, and reliability in analyte identification. Solid-phase microextraction (SPME)[11] and adsorbent-based devices[12,13] are also used to sample VOCs in the field condition in conjunction with GC-MS. The miniaturized version of GC, also known as micro-GC, has received increasing attentions in the last two decades[14–17] due to its increased portability, high response time, and small dead volume. Since the first demonstration by Terry and co-workers[18], numerous efforts have been made to develop the miniaturized GC system on a basis of silicon micromachining and microelectromechanical system (MEMS) technologies[18,19]. The key components of a micro GC system include preconcentrators[20–22], separation columns[23–25], micropumps[26], microvalves[27,28] and various GC detectors[29–31]. Among these components, a miniaturized preconcentrator (denoted as micro-PC) increases the effective concentration of analytes and improves the overall detection limit and sensitivity of micro GC systems with nominal sensing technologies. Micro-PCs work by trapping the target analytes in high surface-area adsorbents for a period of time and rapidly releasing the trapped analytes via thermal desorption[32] in a narrow band. This narrow desorption peak with increased concentration would effectively enhance the separation efficiency of micro separation column and also increase the sensitivity of analysis. Another important functionality of

micro-PCs is that it can be used as an in-line injector. Adsorbed species can be injected into a column or detector without complex plumbing such as valves[33].

Numerous developments have been reported on the miniaturization of PCs in micro GC system. Manginell *et al*. from Sandia National Laboratories reported a microfabricated planar PC incorporating a surfactant templated sol gel adsorbent layer to achieve efficient analyte collection with rapid, efficient thermal desroption[34]. Alfeeli *et al*. presented a microthermal PC device with high-aspect-ratio 3D structures coated with a uniform polymer adsorbent film, which has sharp reproducible desorption peak[35]. Lang *et al*. developed a micromachined PC consisting of 16 silicon micro channels loaded with Carboxen® 1000 adsorbents to monitor a 100-ppb-level of ethylene[36]. Zellers and coworkers[37,38] developed a sophisticated monolithic and multiple microfabricated PC-focuser for the analysis of complex vapor mixtures to improve the thermal desorption performance based on advanced Si-based MEMS technology. The Agah's group reported a new approach of enhancing the adsorption capability of the widely used polymer adsorbent Tenax TA poly(2,6-diphenylene oxide) through its deposition on a nano-structured template due to higher surface area of modified interior surface[39]. The Kurabayashi's group demonstrated a micromachined-Si passive vapor PC to analyze organic vapor mixtures. Toluene at concentration of ~1 ppm was captured by means of passive diffusion and have more than 95% thermal desorption efficeiency[40]. Finally, the Shannon's group reported an integrated micro gas PC and this integration system has an ultra-small preconcentrator volume and microvalves for fast injection speeds[32].

Most of the approaches to fabricating micro PCs mentioned above were based on the Si-based MEMS technology, in which photolithography and bulk Si etching technique like deep reactive ion etching (DRIE) were used to create desired 3D structures. The small-scale device produced by the MEMS technologies has advantages such as low dead volumes and thermal mass,

leading to a higher analysis speed and less energy/power consumption. However, micro PCs have critical challenges that are common in other MEMS-based chemical devices for gas flows and medium-to-high temperature applications. First, MEMS fabrication typically involves multiple cleanroom-based processes of photolithography, oxidation, reactive ion etching, bonding, etc., and some of these processes are very expensive or time-consuming. Furthermore, fluidic interconnections often based on glass capillary tubing need to be established between micro PCs and other components when they are integrated in a modular fashion. One of the common approaches is to use high-temperature glue for sealing the connections, but they tend to fail because of repeated thermal cycling and lack of robust commercial connection solution. Therefore, developing a straightforward approach to fabricating small-scale PCs with better fluidic interconnection is highly desirable. Here we propose to use metal 3D printing approach to fabricate PCs and demonstrate its applicability.

Numerous microfluidic and micro-chemical systems have been fabricated using various 3D printing technologies[41,42], but most of them were made of photosensitive polymers that cannot survive in the medium-to-high working temperatures and thus make it impractical to be used in applications such as micro-PCs. For medium-to-high temperature applications, metals and ceramics are good candidate materials for 3D printing. However, much less work has been reported for microfluidic or microchemical systems made from metal or ceramic 3D printing, also known as additive manufacturing (AM). Gupta *et al*. explored compact titanium alloy chromatography columns with an internal monolithic phase for use with real time bidirectional temperature modulation capability[43]. Sandron *et al*. reported coiled planar capillary chromatography columns which were 3D printed in stainless steel or titanium alloy and showed the potential application of these 3D printed columns in future portable chromatographic devices[44]. To our knowledge, no

work has been presented to create 3D printed PCs for GC applications. Moreover, metal devices printed for fluidic applications have been fabricated mainly using selective laser sintering processes, in which a removal of loose powder can be challenging for long, tortuous microchannel geometries.

In this report, we develop a binder jet printing (BJP) approach to fabricating stainless steel (SS) PCs by leveraging boron nitride sintering additives for high-density parts with internal conduits. Design and material flexibility offered by BJP allows us to create sophisticated features inside a SS channel and machine the inlet and outlet of the device for simple and robust fluidic interconnects. The 3D-printed SS PC along with the commercial connectors were tested for gas-tight leakage under high operating pressure. The flexible membrane heater and temperature sensor were integrated with the 3D-printed SS PC for rapid heating with a controlled ramping rate. The SS PCs filled with high surface area adsorbents were tested as an inline injector for trapping a model volatile organic compound and thermally desorbing it at a higher concentration. We also studied the effect of device thermal mass, level of insulation, and heating rate on PC performance. The resulting device can serve as a front-end injector for portable and real-time gas sensing applications.

2.2 Device Fabrication and Experimental Details

Design of 3D-printed SS PCs and fluidic interconnection: Figure 2.1 shows the cross-section view of the 3D-printed SS PC design along with commercial fluidic connectors. A hollow cylinder of 10 mm in outer diameter and 38.68 mm in length has a fluidic conduit in the center with an array of cylindrical posts (0.75mm in diameter) to improve heat transfer characteristics. The post gap (separation) is related to the minimum printing resolution as well as the pressure drop and heat

conduction. Adsorbents are thermally insulating, so in order to uniformly heat the adsorbents, the post array is placed to distribute heat more uniformly across the adsorbent bed. The center hollow part of the device is to be filled with solid adsorbents (HayeSep D, Sigma Aldrich) to trap volatile compounds (toluene) for PCs. On both sides of the open ends, 10-32 standard port thread was made for suitable commercial fitting for strong fluidic interconnection with small Teflon (1/16" OD) or glass capillary tubing (530 μm OD). PEEK (polyetheretherketone)-based fittings from IDEX Health & Science provides gas-tight fluidic connections that can operate under pressure up to 1 MPa and temperature up to 343°C.

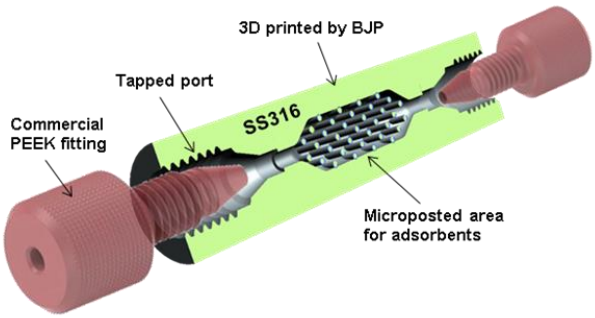

Figure 2.1 A schematic of the proposed stainless steel (SS) preconcentrator (PC) with commercial PEEK fitting for fluidic interconnects.

Fabrication of SS PC via BJP: Samples were fabricated using a binder jetting printing (BJP) machine (X1-Lab, ExOne Inc., Huntington, PA) from stainless steel 316 (SS316) powder (OERLIKON Metco (US) Inc., Troy, MI) and boron nitride (BN) sintering additive (Sigma-Aldrich). BJP is one of the oldest metal 3D printing technologies that print structures by joining metal powder with polymeric binder droplets in a layer-by-layer fashion. The inkjet-like head locally delivers a binder solution to desired locations on the powder bed. The whole process can be broken into several steps as shown in Figure 2.2. First, a 3D drawing of the device design (Figure 2.1) was created using CAD software and imported into the BJP machine. A mixture of

SS316 powder (average particle size ~ 14 μm) and 0.25 wt% BN sintering additive powder (average particle size ~ 1 μm) was fed to both build bed and powder supply bed. A roller ran across from the powder bed to the build bed and spread the powder mixture uniformly (Fig. 2.2a). Polymeric binder droplets were deposited onto the designated area of the build bed (Fig. 2.2b). The powder spreading and binder phase printing steps were repeated (Fig. 2.2c) in a layer-by-layer fashion (after each layer, the build bed stage is lowered while the supply bed stage is raised) till the part was fully printed. Upon the completion of the printing, the build bed along with the printed part was put into an oven to cure the binder phase at 195°C for 2 hours (Fig. 2.2d). After loose powder was removed, the printed part was again put into an oven this time at 460°C for 2 hours to decompose the remaining binder phase (Fig. 2.2e). At this point, the part was fragile and therefore should be carefully transported to a high-temperature vacuum oven (Model G-3000, Materials Research Furnaces, Allenstown, NH) for sintering at 1250°C for 6 hours. The vacuum pressure was maintained at 1.33 Pa, better consolidating powder particles and helping to achieve near full-density parts.

Membrane heater fabrication: Instead of using a built-in thermal desorption unit (TDU) in GC, we developed a membrane heater and temperature controller to heat the SS PCs with reasonable speed and power consumption. A membrane heater was made by sandwiching a serpentine pattern of a thin NiCr wire (40 AWG, Coil Society Online) between two Kapton tapes (50 μm thick, Uline Inc.). The nominal resistance of the membrane heater was around 245.7ohm. To monitor the temperature, another serpentine pattern of a metal wire with a high temperature resistance of coefficient (TCR) was placed on top of the heater membrane, serving as resistance-temperature detectors (RTDs). Nifethal 70 (40 AWG, Coil Society Online) was chosen for this purpose as its TCR is around 5.25×10^{-4}/°C, which is high enough to produce sufficient resistance differences

upon mild temperature change. The RTD resistances were measured as a function of temperature to verify the TCR values.

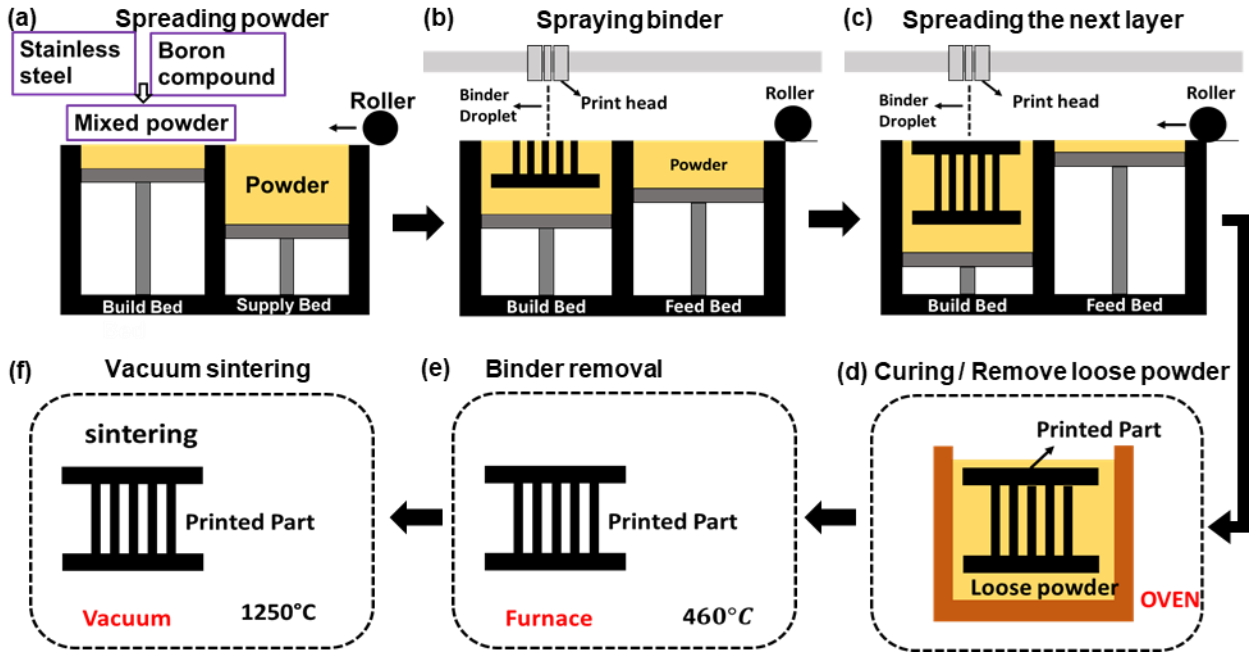

Figure 2.2 Schematics of the binder jet printing (BJP) process flow: (a) delivering and spreading SS powder from the feed bed to the build bed, (b) spraying binder phase in the build bed according to the design, (c) delivering and spreading the next layer of SS powder and repeat (b) and (c) until the part is fully printed, (d) curing the part and remove loose powder, (e) burn out binder phase in an air furnace, (f) sintering the part in a vacuum furnace.

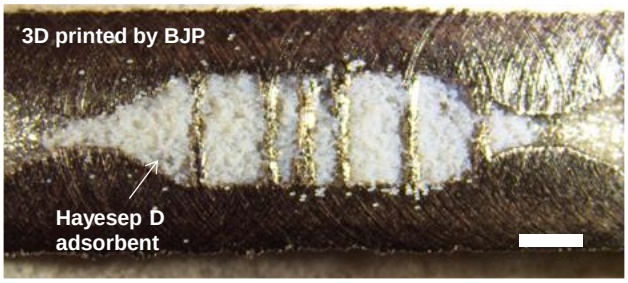

Figure 2.3 A photograph of the cross-sectional view of the SS PC (SS316 and BN) filled with the porous polymer adsorbent, Hayesep D. Scale bar = 3 mm.

Preconcentrator testing: The adsorbent material, Hayesep D (100/120 mesh, Supelco, Bellefonte, PA), is a porous polymer with a specific surface area of 795 m^2/g. First, a small quantity of glass wool was inserted at one end of the device. The adsorbent particles were poured into the PC chamber from the other end with light tapping until it was tightly filled (see Figure 2.3). Glass wool was also inserted at the other end serving as a placeholder for the adsorbents. Hayesep D is a suitable candidate for trapping volatile organic compounds (VOCs) due to its high surface area. In this study, toluene was selected as a model VOC to test the performance of SS PCs. Figure 2.4 shows the sampling/desorption configuration used for PC testing. In the sampling stage (Fig. 2.4a), a diluted toluene vapor (0.6% of headspace) was charged into a SS PC using a syringe pump (Harvard Apparatus) through a 4-port valve (VICI, Inc.). The outlet of the SS PC was connected to the mass spectrometer (MS) through an uncoated, passivated column (50-m long) to minimize surface adsorption inside tubing during sample transport. A sampling volume of 10 mL was passed through the SS PC, so that the adsorbents were charged with toluene. No breakthrough of toluene was observed in the GC-MS instrument (Agilent GC-MS L). The diluted toluene sample was prepared in a Tedlar bag by inserting 6 mL of the headspace of toluene into 10 L of clean, dry nitrogen. In the next step (Fig. 2.4b), the 4-port valve switched its position such that a carrier gas of Helium (a flow rate of 0.5 mL/min) flushed any residual toluene vapor in the transfer lines and the dead volume of the SS PC, and the baseline signal of the GC-MS instrument (Agilent GC-MS L) was obtained. In the final step (Fig. 2.4c), while the carrier gas was flowing, the SS PC was rapidly heated to the target temperature (180°C) to thermally desorb the trapped toluene from the adsorbents. These desorbed species were eluted and detected by GC-MS. In order to prevent heated, desorbed toluene from being condensed inside the capillary tubing, the segment of tubing from the

SS PC and the GC-MS oven was heated to 110°C with a custom-made heating jacket. The GC-MS oven was also maintained at 110°C.

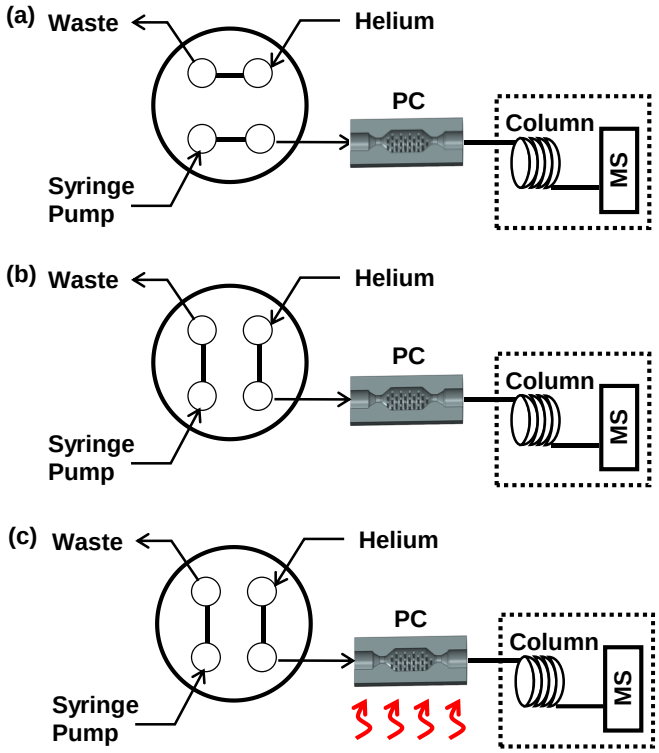

Figure 2.4 Schematics of sampling and injection steps using a 4-port valve: (a) in a sampling step, a diluted toluene is trapped in a PC, (b) as a valve position is switched, a carrier gas of helium flushes residual toluene in the transfer lines and PC, and (c) thermal energy is applied to the adsorbents to release trapped toluene to GC/MS for detection.

2.3 Results and Discussion

2.3.1 Device design and fabrication results

Several important design and operational considerations for SS PCs include a PC volume (i.e., adsorbent volume and surface area), dead volume, thermal mass, level of thermal insulation, heating rate, etc. First, a PC volume is an enclosed volume occupied by adsorbents that typically possess high surface areas per unit volume. A small PC volume means a low adsorption capacity and is susceptible to analyte breakthrough. A large PC volume, however, takes too much time or

power to desorb and can saturate column (or degenerate separation efficiency). Therefore, the PC volume can be determined based on the desirable applications. Thanks to their small sizes, the microfabricated MEMS PCs have very small PC volumes suitable for focusing and injection for column separation. Conversely, SS PCs have a relatively large PC volume because the printing resolution of BJP is limited to a few hundreds of microns and the features as small as ones found in the MEMS PCs cannot be printed. Here, the PC chamber volume of our work is around 117.7 mL and the thermal mass is 119.9 mg, and thus we consider it useful for an in-line injection application. Secondly, a dead volume is another important parameter influencing the preconcentration factor because, if there is any dead volume, the desorbed species become diluted and the PC performance degenerates. In our work, the dead volume is not an issue as the PC is used as an in-line injector (to be discussed later). Thirdly, thermal mass and level of thermal insulation are design parameters and affect the heating and cooling rates and power consumption during the operation. Thermal mass should be minimized to increase both heating and cooling rates and decrease power consumption. The wall thickness of the SS PCs cannot be arbitrarily small, since the BJP parts are known to be porous (even after using sintering additives) and the thin wall may result in gas leakage. Therefore, we explored a few different wall thicknesses to test the effect of thermal mass for heating performance of the SS PCs. Finally, the heating rate is an operational parameter that influences the speed of analyte desorption, i.e., the peak height and width. Therefore, a higher heating rate should provide a higher preconcentration factor for the PC with the same adsorption capacity. SS316, which is the PC material in our work, has a higher thermal conductivity (k = 13~17 W/m-K) than most polymeric materials (k < 0.5 W/m-K), and thus spreading heat from the heating element can take place more quickly and uniformly in the SS part. However, the adsorbent materials have low thermal conductivity, (in case of porous polymer, k =

0.01~0.03 W/m-K), so we put an array of cylindrical posts within the PC chamber to better distribute thermal energy.

Figure 2.5a and 2.5b shows the photographs of two SS PCs of the same design: one made of SS316 powder only and the other made of SS316 powder and BN additives. By inspecting the appearance of these two PCs, we observe that the PC with SS316 and BN is smaller in size and shinier (more silvery) than one with SS316 only. The diameter of as-printed SS PCs was 10.42 (note that the designed diameter is 10 mm). After sintering them at 1250°C for 6 hours, the diameter of the resulting devices was 9.79 mm for the 3DP PC with SS316 only and 9.3 mm for the 3DP PC with SS316 and BN. A smaller size of the 3DP PC with SS316/BN can be attributed to the fact that the sintering additive, BN, reduces the liquidus temperature of SS316 and increases the part's density, leading to the smaller size. It is well known that BN reduces the temperature at which liquid phase of SS is formed, but the extensive formation of liquid phase due to a larger BN quantity can substantially distort the shape of the part. A similar shape distortion can happen if the part is sintered at temperatures higher than the desired level. In our previous work[45,46] , the optimal quantity of sintering additives at various sintering temperatures was determined to maximize the density of SS420 and SS316 parts without noticeable distortion of the part shape. Therefore, the sintering condition used in this work was based on those previous works. Another reason that the sintering additives can increase the part's density is a large difference in particle size. The size of BN powder particles is around 1 μm while that of SS316 powder is around 14 μm. Therefore, when two powder particles are well mixed, the BN powder particles penetrate into the interstitial spaces between SS316 powder particles and fill in the gap, effectively decreasing the porosity and improving the density. The incorporation of BN into SS316 also helps to improve the surface

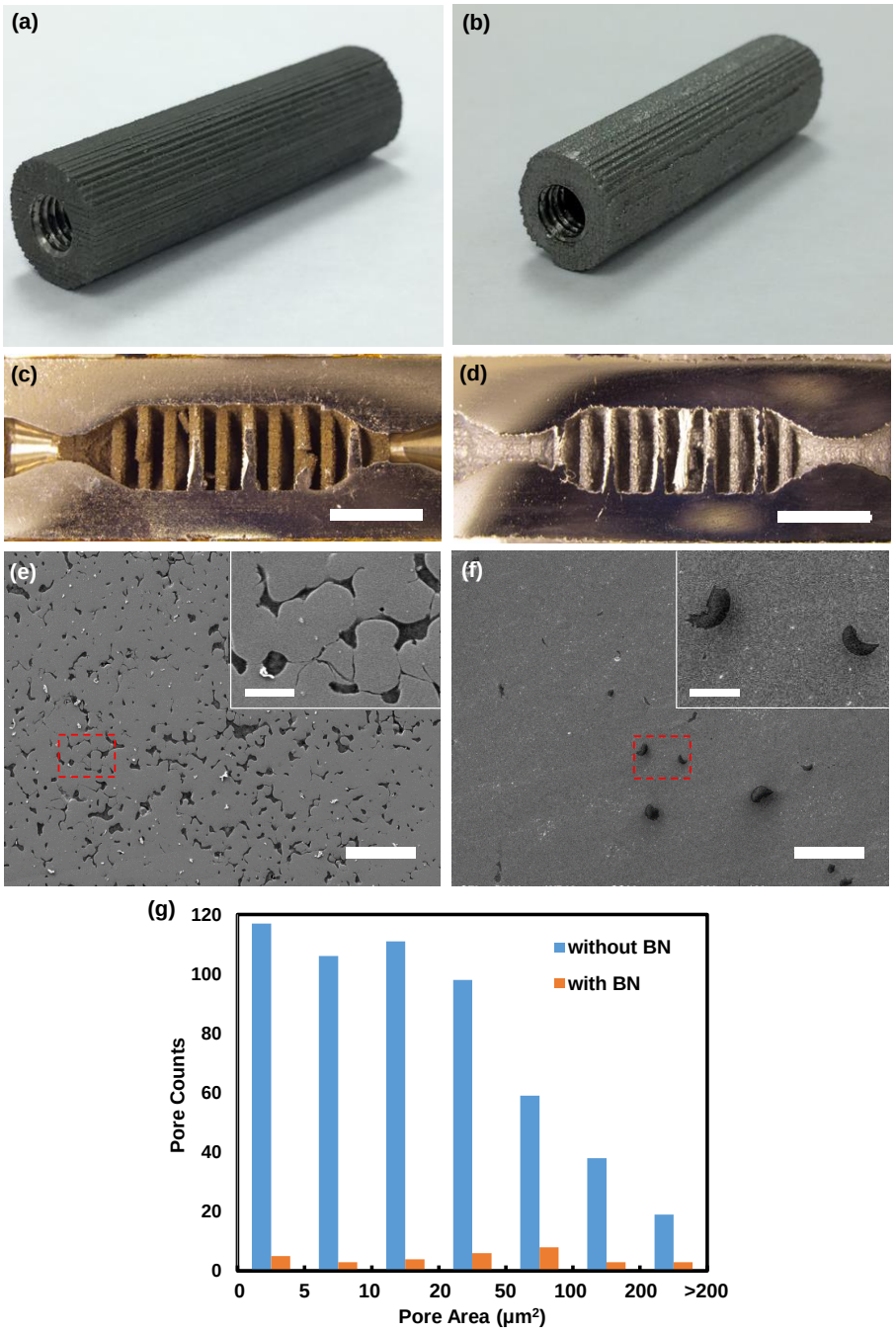

Figure 2.5 Photographs of the as-sintered PCs (10-mm in diameter and 38.68-mm in length) with (a) SS only and (b) SS and BN; optical microscope images of the cross-sections of the as-sintered PC with (c) SS only and (d) SS and BN, scale bar=5000μm; SEM images from the cross-sections of the as-sintered PC with (e) SS only and (f) SS and BN, scale bar = 100 μm, (inset) zoomed-in images of the red-marked area, scale bar = 10 μm; (g) histogram of pore areas in the images (e) and (f).

smoothness of the fully-sintered part[45,46]. The shinier (more silvery) surface of the 3D-printed PC with SS316/BN (see Figure 2.5b) results from the better surface smoothness[46].

The porosity level of the BJP parts can be estimated by directly visualizing their cross-section and performing image analysis. The samples were cut in half and polished using a lapping film with 1-μm grit. The optical images of the cross-sectional views of both samples (3D-printed PCs with SS316 only and with SS316/BN) can be found in Fig. 2.5(c) and 2.5(d). The SS316/BN PC exhibits more reflective surface than the SS316-only PC, indicating that the former sample is less porous and has fewer light scattering pits. The scanning electron microscope (SEM) images in Fig. 2.5(e) and 2.5(f) show the porosity level in details for both samples. The SS316-only PC shows significantly more pores (darker regions corresponding to the pores in the structure) than the SS316/BN PC. Specifically, four SEM images from various regions of the samples were analyzed to estimate the percent porous areas, revealing that the areal porosity is about 8.05% and 0.92% for the SS-only PC and SS316/BN PC, respectively. This means the SS316/BN PC is denser than the SS316-only PC, corroborating the size difference of the sintered parts. The porosity of the 3D-printed PCs is particularly important in device testing and performance because it influences gas leakage through the device walls. While the porosity of 8.05% in a structure may not cause a leakage (in case spherical pores are randomly distributed), as the inset image of Fig. 2.5(e) displays, the pores were formed at powder boundaries during sintering and are highly elongated and connected. Therefore, one can perceive that there may be a percolation path of gas molecules through the structure even with a relatively low porosity. When BN is incorporated in the SS structure, those elongated pores mostly disappeared (see Fig. 2.5(f)) and the observed pores were more isolated and rounded, suggesting that a gas leakage is less probable through the structure. Figure 2.5(g) shows the pore area distributions of both samples for the same-size imaging area

(using Fig. 2.5(e) and 2.5(f)). It clearly demonstrates that the total number of pores is far fewer for the SS316/BN PC. In addition, it is shown that there are many more small-size pores in the SS316-only PC, but the small-size pores tend to merge favorably when BN is present in the powder mixture.

2.3.2 Fluidic interconnect and leak test

In order for micro-PCs to function in chemical analysis system, they need to be connected to other components such as separation columns and sensors. Unless monolithically integrated[18] , each of these components is modularly integrated and typically connected via polyimide-coated glass capillary tubing[47,48] . The majority of micro-PCs are based on Si, which is brittle and difficult to be machined for fluidic connections. Therefore, capillary tubing was attached to the inlets and outlets of Si devices with the help of high-temperature glues or adhesives[37,38]. Such approaches are not sufficiently robust for many temperature cyclic operations causing mechanical/thermal stresses and can be susceptible to contamination and large dead volumes. In our case, the 3D-printed PCs are easily machinable because the part was made from SS; and therefore commercial compression fitting can be used to create leak-tight, robust and low dead volume connection to capillary tubing. It is also important to point out that, unlike the gluing approach, the compression fitting can support much higher pressure operation and tubing can be easily replaced.

Typically, metal additive manufacturing (AM) techniques including BJP provide near net shapes of desirable parts and thus should be able to generate threaded holes for compression fittings for the SS PCs. But the surface roughness inherent to BJP (in fact, other AM techniques also suffer from the surface roughness issue) is too high to provide a leak-tight seal with fittings. Post-processing steps including polishing or tapping can be used to generate smooth surface for fittings. In the beginning, we attempted to fabricate the PCs from both SS420 and SS316 powders.

While SS 300 and 400 series are generally machinable, we found that SS420 parts became difficult to be machined because residual carbon remaining from the binder burnout process got incorporated into SS420 during sintering, rendering the part to be hardened (i.e., becoming martensitic) and making it difficult to be machined. Therefore, we fabricated SS316 PCs and tapped inlet and outlet holes for 10-32 port fitting. PEEK fitting was then used to connect capillary tubing with the SS PCs (see Figure 2.6) as the plastic material has low thermal conductivity and reduces heating budget.

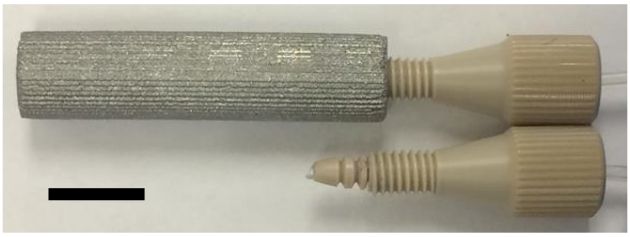

Figure 2.6 A photograph of the SS PC (with BN) connected with the commercially available PEEK fitting (for 1/16" tubing, IDEX Health & Science). Scale bar = 1 cm.

Leak testing was performed for two SS316 PCs with and without BN sintering additives. After the PEEK fitting and tubing were inserted into the inlet and outlet of the PC, the assembled part was immersed into an isopropyl alcohol (IPA) bath. The presence of leaks upon a gas flow would form bubbles in the solution. Figure 2.7a in Supplementary Information shows that no bubble was observed (meaning no leakage) when an air pressure up to 500 kPa was applied to the dead end through the SS316/BN PC. Conversely, significant air leak was observed from the SS316-only PC (see Fig. 2.7b) when a small air pressure (~ 64 kPa) was applied. This observation is consistent with the porosity levels seen from the SEM images in Fig. 2.5 and image analysis results discussed thereafter. The video clips of leakage testing of these two SS PCs are available in Figure 2.8 and Figure 2.9. It is also important to note that no apparent leak was observed from

the PEEK connection area. Since the device with no leakage is desired for the PC application, we only consider the SS316/BN PC for the rest of the work.

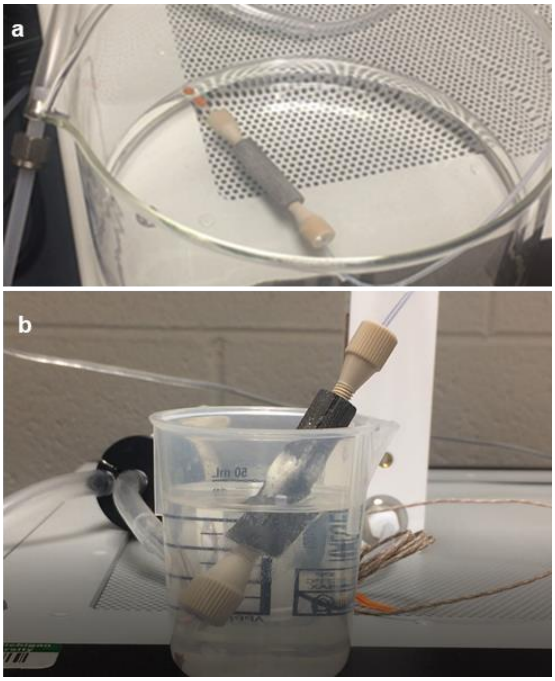

Figure 2.7 Leak test of air applied to the dead end through the SS PCs with a) SS316 with BN and b) SS316 only. The PCs were immersed in an IPA solution.

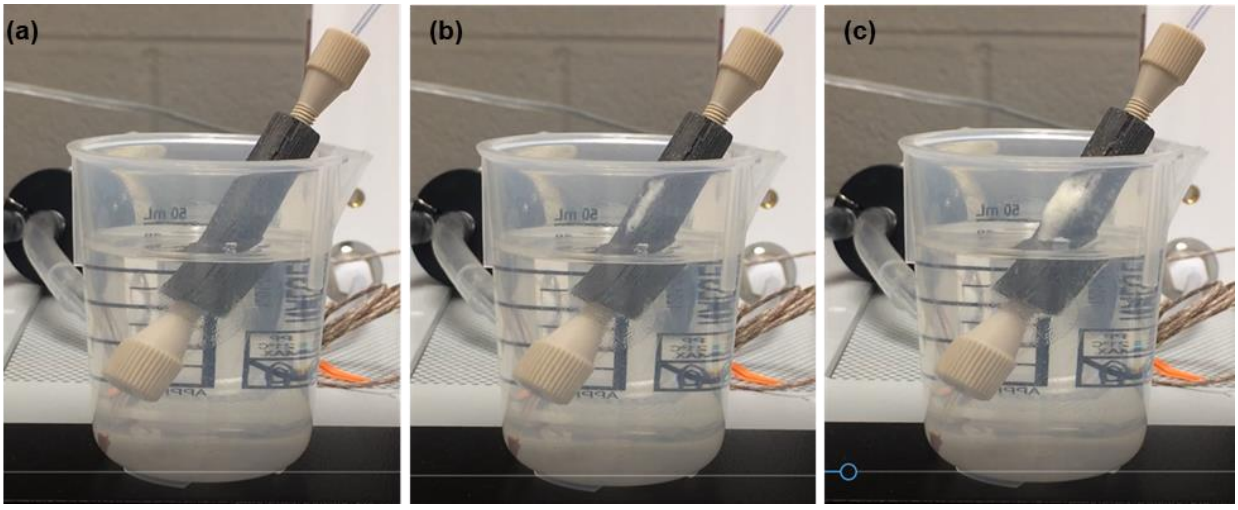

Figure 2.8 Video clip of leak test for SS316 only sample: when N_2 go through the SS316 only sample with small pressure (~64kPa), a big leak (bubbles) was observed (a-c) on the surface of the sample wall, meaning high porosity of the sample.

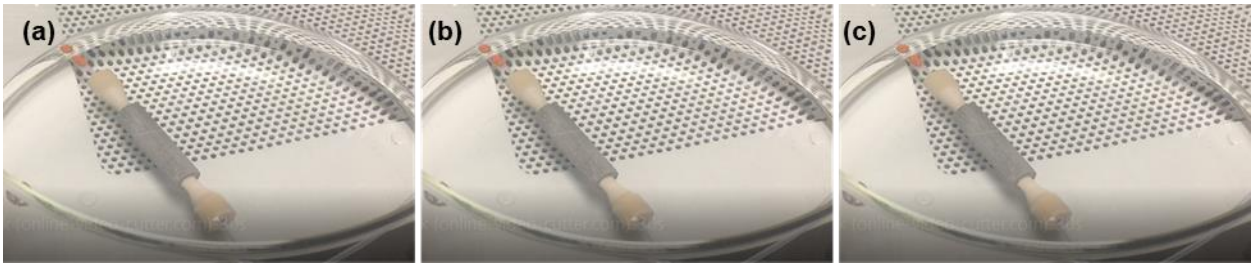

Figure 2.9 Video clip of leak test for SS316/BN sample: 500kPa pressure of N_2 was flowing to dead end PC (SS316 with BN) system and no leak (bubble) was found in the 3DP sample and connection between sample with tubing. This leak-tight results attribute to the near full dense structure when BN was used to improve the dense of sample after sintering.

2.3.3 Membrane heater and RTD sensor characterization

Release of adsorbed species from the PC is typically accomplished by thermal desorption. In this work, a custom-built heater was fabricated and attached to the PC to increase the unit temperature. In order to minimize the form factor (and in turn the associated thermal mass), we have developed a thin, flexible membrane heater that wraps around the SS PC. A heating rate and final PC temperature are important experimental parameters; therefore, a thin, flexible temperature sensor was also developed and integrated to the heater/PC for feedback control of temperature. Figure 2.10(a) shows a schematic of the membrane heater/sensor stacked on top of each other between the thin polyimide membrane (Kapton® tape). The heater layer was made of a serpentine pattern of a thin nickel chrome (NiCr) wire (80 μm in diameter) while the sensor layer was made of the similar serpentine pattern of a thin nickel-iron (NiFe) wire (80 μm in diameter). NiCr has a small coefficient of thermal expansion (CTE, $\alpha = 1\sim15 \times 10^{-6}$ /K), which is suitable for heating application because the resistance of the wire resistor does not vary significantly upon heating. Conversely, NiFe70 has a relatively large CTE value ($\alpha = 4000\sim4500 \times 10^{-6}$ /K), making it feasible to be used as a resistance-temperature detector (RTD) because a small change in temperature can cause a measurable response in wire resistance. Figure 2.10(b) shows the top-down view of the

fabricated heater/sensor stack. The wire was closely weaved in a serpentine pattern with a uniform pitch to increase the total resistance value (resulting in a higher response for RTD) as well as to achieve more uniform heating. When 14.6 W of power was applied to the heater, the stack was rapidly heated to 315°C in 12 sec. The uniformity of the temperature distribution across the membrane heater/sensor can be seen in Fig. 2.10(c). Figure 2.10(d) shows the SS PC wrapped with the membrane heater/sensor and assembled with two PEEK fittings. The thermal conductivity of PEEK is much lower than SS, so during the heating period, we assume that the conduction loss to the fittings is not as significant as the convective loss through the outer heater surface. Finally, the resistance (R) of the RTD sensor was measured as a function of temperature (T) to obtain the actual CTE value. Figure 2.10(e) shows the linear behavior of the R-T relationship with fitting parameters of the slope of 0.0865 and the intercept of 19.9. The CTE, α, of the RTD sensor was computed by taking slope/intercept, which is 0.00435. This value is within the range of the NiFe's CTE. Either fitted line or calibrated R-T data is used in monitoring the temperature of the SS PC simply from reading the resistance value of the RTD sensor.

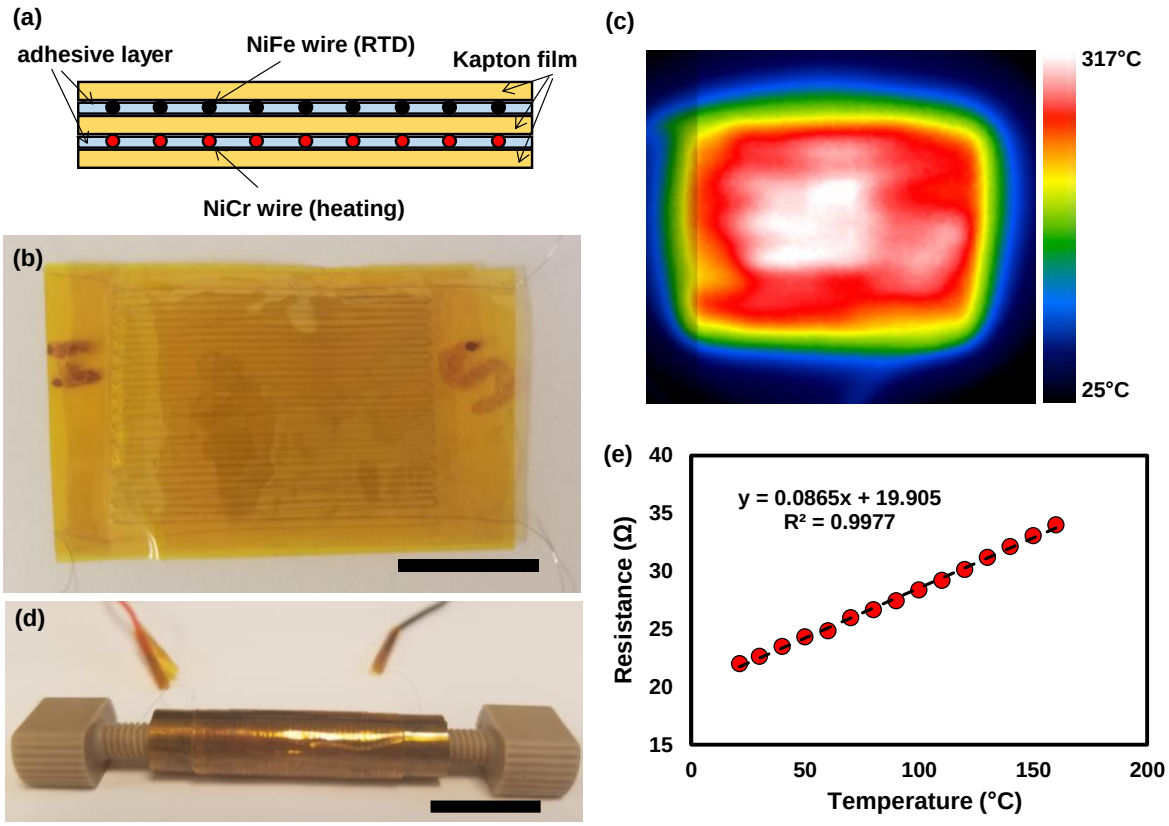

Figure 2.10 (a) A schematic diagram of a flexible membrane heater and resistance-temperature detector (RTD), (b) a photograph of the fabricated membrane heater and RTD using the Kapton® films, NiCr and NiFe wires; wires were weaved in a serpentine pattern to increase the overall length and resistance, scale bar = 10 mm, (c) an IR image from a thermal camera when 14.6 W of power is applied to the heater, (d) a photograph of the SS316/BN wrapped with the heater/RTD, scale bar = 15 mm, (e) a calibration curve for the RTD sensor.

2.3.4 In-line injection performance of the 3DP PCs

The proposed SS PC works by sorption trapping followed by thermal desorption of high surface area adsorbents. Before testing the device for in-line injection performance, we need to ensure that the adsorbents can be heated to the target desorption temperature, which is about 180°C for Hayesep D. We also note that the temperature of the membrane heater can be monitored via the RTD sensor, but not the SS PC itself. Once the SS PC is attached to the heater, the overall thermal mass increases significantly, slowing down a heating rate and reducing the final achievable temperature. In addition, a carrier gas flowing inside the SS PC reduces the device temperature

further. Therefore, a series of experiments was conducted to find the appropriate membrane temperature that provides sufficient heating power for the SS PC to reach 180°C for a given flow rate. Our experiments showed that when the membrane heater was heated to approximately 350°C, the center region of the SS PC (measured by a thermocouple probe) reached 183°C for a constant helium flow rate of 0.5 mL/min.

A heating rate, i.e., how rapidly the SS PC reaches the target temperature, depends on thermal mass, applied power, and level of thermal insulation. Smaller thermal mass is more beneficial in terms of thermal performance metrics such as ramp-up time and powder consumption. Our approach to reducing thermal mass is to remove the outer materials of the fully sintered SS316/BN part by means of machining. The diameter of the SS PC was reduced from 9.3 mm to 7.69 mm, reducing thermal mass from 13773 mg to 9373 mg. We also tried to print SS PCs with thinner wall, but the parts became too fragile to be handled during the powder removal and curing steps. Figure 2.11(a) shows the temperature profiles as a function of time when the membrane heater was heated to the same target temperature (and same ramping rate) for 3 minutes to each PC of two different thermal mass. The temperature of the SS PC with smaller thermal mass was raised to 180°C in about 85 sec while one with larger thermal mass reached the maximum temperature of 160.5°C in about 370 sec. Therefore, for the rest of the study, we present the experimental results from the PC with smaller thermal mass.

Another important factor in heater/PC performance is thermal isolation. There are three main heat loss in the PC: convective and radiative losses around the surface area of the membrane heater and conductive loss to the fluidic connectors at both ends. We use PEEK fittings to minimize the conductive loss, and further improvement in thermal isolation to the sides is difficult to be achieved. But the convective/radiative loss around the membrane heater can be significantly

reduced by wrapping a high-temperature insulation mat around the PC. A thin Al foil was sandwiched between two layers of insulation mat to further prevent a radiative loss. Figure 2.11(b) shows the different temperature responses of the same SS PC with different thermal insulation condition - no insulation vs an insulation layer. The same power of 4.5 W was applied to heat the SS PC. We can observe that the center region of the SS PC can heat up to around 180°C in 15 mins

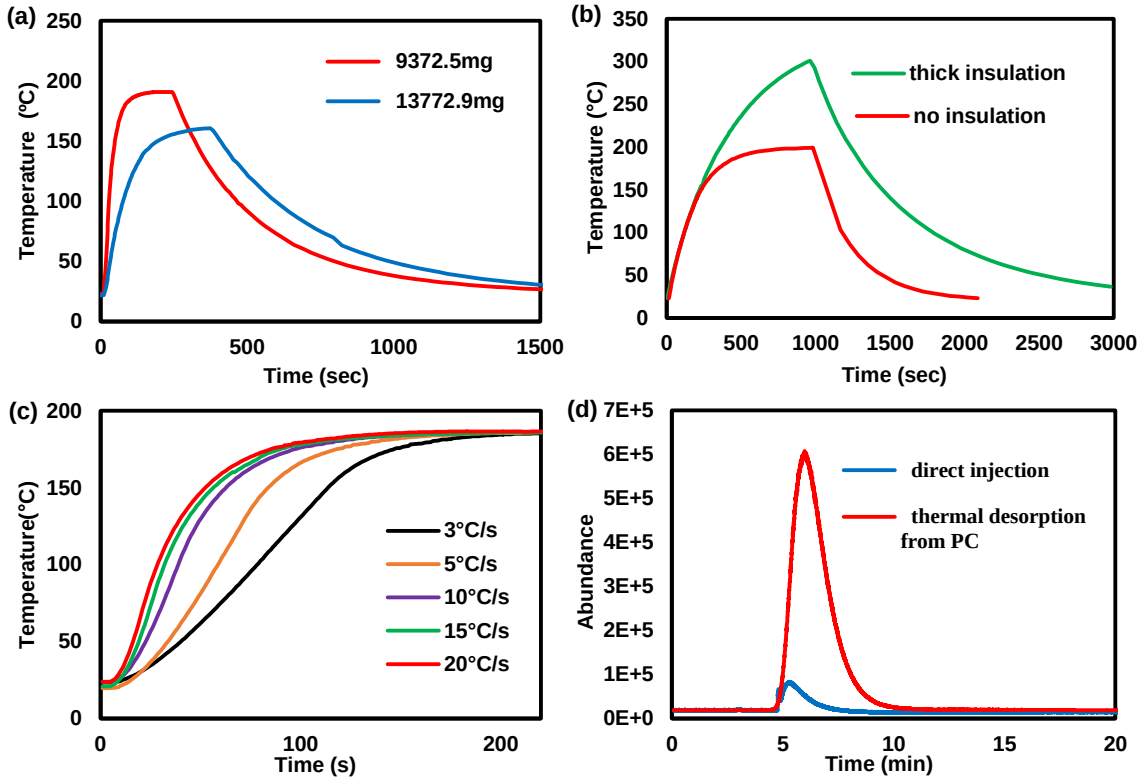

Figure 2.11 Temperature profiles of the SS PC (SS316/BN) (a) with different thermal mass (no insulation); (b) with and without thermal insulation (9372.5 mg sample); (c) a family of the temperature profiles of the SS PC with different heat ramping rates; (d) the mass spectrometer responses for the direct splitless injection of 0.5 mL of 0.6% headspace toluene (blue line) and for the thermal desorption peak of toluene after sampling of 10 mL of 0.6% headspace toluene into the SS PC.

without insulation while the temperature of the center region rises to 320°C in 15 min. This means that thermal insulation allows the PC to reach the target temperature more rapidly or with less

power consumption. However, the insulation layer impedes a cooling process, represented by the slower decay of the temperature in Figure 2.11(b). This means that one has to wait longer before the next run can be initiated. Therefore, a decision of whether thermal insulation should be integrated depends on the operational requirements (power consumption vs. speedy recovery).

The center hollow part of the device is to be filled with solid adsorbents (HayeSep D, Sigma Aldrich) to trap volatile compounds (toluene) for PCs (see Fig. 2.3). When the adsorbent materials such as Hayesep D are subject to the temperature beyond the suggested level (~ 180°C), they start to degrade and lose the adsorption capacity. Therefore, an open-loop control of temperature (i.e., the PC temperature simply controlled by the level of constantly applied power) may be inappropriate for a long-term use of the porous polymer adsorbents. We use the integrated RTD sensor to maintain the PC temperature at the target level by means of feedback control. Figure 2.11(c) shows the temperature profiles of the SS PC with various heating rates from 3°C/s to 20°C/s. The highest heating rate (20°C/s) can have the absorbents reach the desorption temperature (180°C) in about 100 sec. With the other heating rates of 15, 10, 5, and 3°C/s, the time it takes to 180°C is 110, 117, 136, and 166 sec, respectively. For the desorption testing, we chose 20°C/s for heating rate for a fast response. In the future, we can further reduce the thermal mass of sample through changing the design or machining out more mass of sample, which is also an advantage of 3D printing technology for fabricating PCs.

Finally, the role of the SS PC as an inline injector is demonstrated using toluene as a model volatile organic compound. When 0.5 mL of 0.6% diluted toluene from the headspace in the sampling bag was directly eluted to the GC/MS via splitless injection, the relatively small peak was observed (blue line) in Fig. 2.11(d). To enhance the detector's response, we sampled 10 mL of the same diluted toluene (0.6%) into the SS PC. We observed the toluene peak during the

sampling process, meaning that the adsorbents were fully charged. Upon the heating of the PC to the target desorption temperature (for Hayesep D, 180°C), the trapped toluene would be released in a relatively short time period and the concentrated pulse would be delivered to the detector by the carrier gas. The red line in Figure 2.11(d) shows the concentrated toluene peak after thermal desorption (see Fig. 2.12 for the toluene verification by the mass spectrometer). The area under the curve in the chromatogram can be related to the amount of the detected molecules. The ratio of the peak areas for both signals was estimated to be 14.2, which is less than the sampling volume ratio of 10/0.5 = 20. It can be attributed that some toluene may have been lost during the purging step and by condensation inside the connectors/tubing. In the end, if the SS PC is placed in front of a gas detector, it can be used to trap VOCs of low concentration and make an injection of more concentrated analytes at any desirable time without resorting to valve operation.

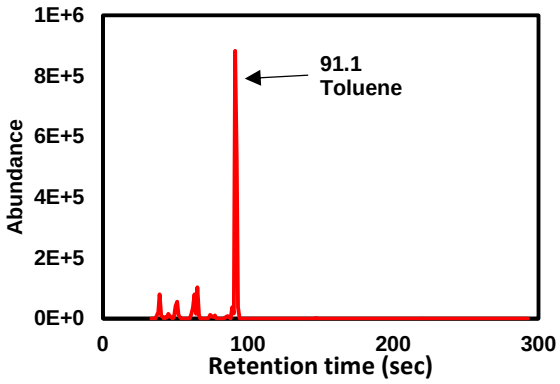

Figure 2.12 Mass-spectrometer signal of the desorbed analyte from the SS PC, confirming that the peak is associated with toluene.

2.4. Conclusion

Recent advances in additive manufacturing (AM) or metal 3D printing technology have enabled the fabrication of freeform metallic parts with intricate features. However, metallic parts with the complex internal features for microchannel/microreactor applications are difficult to be

achieved by the more common AM technologies such as selective laser sintering and selective laser melting due to difficulties associated with powder removal from the internal cavities. Binder jet printing (BJP), one of the oldest AM methods, offers advantages including easier powder removal and less built-in stress in the sintered parts and can be used to make microchannel or microreactor parts for medium-to-high-temperature applications. The key challenge is that metal parts built from BJP are highly porous upon sintering and not suitable for fluidic applications. In this paper, we show that the addition of sintering additives such as boron nitride (BN) can facilitate the sintering of stainless steel (SS) to create near fully-density SS parts. Reduction in porosity by BN has been visualized and quantified via image analysis. The proof-of-the-concept device, namely preconcentrator (PC), has been built for preconcentration and inline injection of volatile organic compounds. Unlike the miniature or microscale PCs that were commonly built on silicon, the SS PCs can be machined to be compatible with commercially available fittings, which enables long-term, robust fluidic connections suitable for medium-to-high-temperature applications. We have shown that the SS PC filled with the Hayesep D adsorbent can trap low-concentrated toluene and enhance the detector signal by more than 10 times. In future, more work is geared toward to reduce the thermal mass of the device by optimizing the BJP process, and smaller thermal mass will allow a faster heating rate, which will sharpen a desorption peak and improve the overall detection response.

REFERENCES

REFERENCES

1. Mirzaei, A., Leonardi, S. G. & Neri, G. Detection of hazardous volatile organic compounds (VOCs) by metal oxide nanostructures-based gas sensors: A review. *Ceram. Int.* **42**, 15119–15141 (2016).

2. Szulczyński, B. & Gębicki, J. Currently Commercially Available Chemical Sensors Employed for Detection of Volatile Organic Compounds in Outdoor and Indoor Air. *Environments* **4**, 21 (2017).

3. Spinelle, L., Gerboles, M., Kok, G., Persijn, S. & Sauerwald, T. Review of Portable and Low-Cost Sensors for the Ambient Air Monitoring of Benzene and Other Volatile Organic Compounds. *Sensors* **17**, 1520 (2017).

4. Rufo, J. C., Madureira, J., Fernandes, E. O. & Moreira, A. Volatile organic compounds in asthma diagnosis: a systematic review and meta-analysis. *Allergy* **71**, 175–188 (2016).

5. Sun, X., Shao, K. & Wang, T. Detection of volatile organic compounds (VOCs) from exhaled breath as noninvasive methods for cancer diagnosis. *Anal. Bioanal. Chem.* **408**, 2759–2780 (2016).

6. Tripathi, K. M., Kim, T., Losic, D. & Tung, T. T. Recent advances in engineered graphene and composites for detection of volatile organic compounds (VOCs) and non-invasive diseases diagnosis. *Carbon* **110**, 97–129 (2016).

7. Lee, S., Yap, M., Behringer, G., Hung, R. & Bennett, J. W. Volatile organic compounds emitted by Trichoderma species mediate plant growth. *Fungal Biol. Biotechnol.* **3**, 7 (2016).

8. Miyake, Y., Tokumura, M., Wang, Q., Wang, Z. & Amagai, T. Comparison of the volatile organic compound recovery rates of commercial active samplers for evaluation of indoor air quality in work environments. *Air Qual. Atmosphere Health* **10**, 737–746 (2017).

9. Vesely, P., Lusk, L., Basarova, G., Seabrooks, J. & Ryder, D. Analysis of Aldehydes in Beer Using Solid-Phase Microextraction with On-Fiber Derivatization and Gas Chromatography/Mass Spectrometry. *J. Agric. Food Chem.* **51**, 6941–6944 (2003).

10. López, R., Aznar, M., Cacho, J. & Ferreira, V. Determination of minor and trace volatile compounds in wine by solid-phase extraction and gas chromatography with mass spectrometric detection. *J. Chromatogr. A* **966**, 167–177 (2002).

11. Lattuati-Derieux, A., Bonnassies-Termes, S. & Lavédrine, B. Identification of volatile organic compounds emitted by a naturally aged book using solid-phase microextraction/gas chromatography/mass spectrometry. *J. Chromatogr. A* **1026**, 9–18 (2004).

12. Alfeeli, B., Cho, D., Ashraf-Khorassani, M., Taylor, L. T. & Agah, M. MEMS-based multi-inlet/outlet preconcentrator coated by inkjet printing of polymer adsorbents. *Sens. Actuators B Chem.* **133**, 24–32 (2008).

13. Ghoshal, A. K. & Manjare, S. D. Selection of appropriate adsorption technique for recovery of VOCs: an analysis. *J. Loss Prev. Process Ind.* **15**, 413–421 (2002).

14. Jian, R.-S., Huang, R.-X. & Lu, C.-J. A micro GC detector array based on chemiresistors employing various surface functionalized monolayer-protected gold nanoparticles. *Talanta* **88**, 160–167 (2012).

15. Bae, B. *et al.* Development of a portable gas analyzer using a micro-Gas Chromatograph/Flame Ionization Detector (micro-GC/FID) for NASA's environmental missions. in *42nd International Conference on Environmental Systems* (American Institute of Aeronautics and Astronautics, 2012). doi:10.2514/6.2012-3435

16. Azzouz, I., Marty, F. & Bourouina, T. Recent advances in micro-gas chromatography — The opportunities and the challenges. in *2017 Symposium on Design, Test, Integration and Packaging of MEMS/MOEMS (DTIP)* 1–5 (2017). doi:10.1109/DTIP.2017.7984485

17. Kawamura, Y., Konishi, S. & Nishi, M. Development of a micro gas chromatograph for the analysis of hydrogen isotope gas mixtures in the fusion fuel cycle. *Fusion Eng. Des.* **58**–**59**, 389–394 (2001).

18. Terry, S. C., Jerman, J. H. & Angell, J. B. A gas chromatographic air analyzer fabricated on a silicon wafer. *IEEE Trans. Electron Devices* **26**, 1880–1886 (1979).

19. Lu, C.-J. *et al.* First-generation hybrid MEMS gas chromatograph. *Lab. Chip* **5**, 1123–1131 (2005).

20. James, F. *et al.* Development of a MEMS Preconcentrator for Micro-gas Chromatography Analyses. *Procedia Eng.* **87**, 500–503 (2014).

21. Wong, M.-Y., Cheng, W.-R., Liu, M.-H., Tian, W.-C. & Lu, C.-J. A preconcentrator chip employing μ-SPME array coated with in-situ-synthesized carbon adsorbent film for VOCs analysis. *Talanta* **101**, 307–313 (2012).

22. Alfeeli, B. & Agah, M. Micro preconcentrator with embedded 3D pillars for breath analysis applications. in *2008 IEEE SENSORS* 736–739 (2008). doi:10.1109/ICSENS.2008.4716547

23. Bhushan, A., Yemane, D., Overton, E. B., Goettert, J. & Murphy, M. C. Fabrication and Preliminary Results for LiGA Fabricated Nickel Micro Gas Chromatograph Columns. *J. Microelectromechanical Syst.* **16**, 383–393 (2007).

24. Bhushan, A., Yemane, D., Trudell, D., Overton, E. B. & Goettert, J. Fabrication of micro-gas chromatograph columns for fast chromatography. *Microsyst. Technol.* **13**, 361–368 (2007).

25. Radadia, A. D., Masel, R. I., Shannon, M. A., Jerrell, J. P. & Cadwallader, K. R. Micromachined GC Columns for Fast Separation of Organophosphonate and Organosulfur Compounds. *Anal. Chem.* **80**, 4087–4094 (2008).

26. Laser, D. J. & Santiago, J. G. A review of micropumps. *J. Micromechanics Microengineering* **14**, R35–R64 (2004).

27. Galambos, P. *et al.* Active MEMS Valves for Flow Control in a High-Pressure Micro-Gas-Analyzer. *J. Microelectromechanical Syst.* **20**, 1150–1162 (2011).

28. Galambos, P. *et al.* Low leak rate mems valves for micro-gas-analyzer flow control. in *TRANSDUCERS 2009 - 2009 International Solid-State Sensors, Actuators and Microsystems Conference* 1658–1661 (2009). doi:10.1109/SENSOR.2009.5285749

29. Narayanan, S., Alfeeli, B. & Agah, M. Two-Port Static Coated Micro Gas Chromatography Column With an Embedded Thermal Conductivity Detector. *IEEE Sens. J.* **12**, 1893–1900 (2012).

30. Kaanta, B. C. *et al.* High Sensitivity Micro-Thermal Conductivity Detector for Gas Chromatography. in *2009 IEEE 22nd International Conference on Micro Electro Mechanical Systems* 264–267 (2009). doi:10.1109/MEMSYS.2009.4805369

31. Shopova, S. I. *et al.* On-Column Micro Gas Chromatography Detection with Capillary-Based Optical Ring Resonators. *Anal. Chem.* **80**, 2232–2238 (2008).

32. Yeom, J., Field, C. R., Bae, B., Masel, R. I. & Shannon, M. A. The design, fabrication and characterization of a silicon microheater for an integrated MEMS gas preconcentrator. *J. Micromechanics Microengineering* **18**, 125001 (2008).

33. Yeom, J. *et al.* Enhanced toxic gas detection using a MEMS preconcentrator coated with the metal organic framework absorber. in *2008 IEEE 21st International Conference on Micro Electro Mechanical Systems* 232–235 (2008). doi:10.1109/MEMSYS.2008.4443635

34. Manginell, R., CHARLES FRYE-MASON, G., Kottenstette, R., R. LEWIS, P. & Wong, C. Microfabricated planar preconcentrator. (2017).

35. Alfeeli, B., Cho, D., Ashraf-Khorassani, M., Taylor, L. T. & Agah, M. MEMS-based multi-inlet/outlet preconcentrator coated by inkjet printing of polymer adsorbents. *Sens. Actuators B Chem.* **133**, 24–32 (2008).

36. Alamin Dow, A. B. & Lang, W. A micromachined preconcentrator for ethylene monitoring system. *Sens. Actuators B Chem.* **151**, 304–307 (2010).

37. Tian, W.-C., Pang, S. W., Lu, C.-J. & Zellers, E. T. Microfabricated preconcentrator-focuser for a microscale gas chromatograph. *J. Microelectromechanical Syst.* **12**, 264–272 (2003).

38. Tian, W. C., Chan, H. K. L., Lu, C. J., Pang, S. W. & Zellers, E. T. Multiple-stage microfabricated preconcentrator-focuser for micro gas chromatography system. *J. Microelectromechanical Syst.* **14**, 498–507 (2005).

39. Akbar, M. *et al.* Improved performance of micro-fabricated preconcentrators using silica nanoparticles as a surface template. *J. Chromatogr. A* **1322**, 1–7 (2013).

40. Seo, J. H., Kim, S. K., Zellers, E. T. & Kurabayashi, K. Microfabricated passive vapor preconcentrator/injector designed for microscale gas chromatography. *Lab. Chip* **12**, 717–724 (2012).

41. Kitson, P. J., Rosnes, M. H., Sans, V., Dragone, V. & Cronin, L. Configurable 3D-Printed millifluidic and microfluidic 'lab on a chip' reactionware devices. *Lab. Chip* **12**, 3267–3271 (2012).

42. Comina, G., Suska, A. & Filippini, D. Low cost lab-on-a-chip prototyping with a consumer grade 3D printer. *Lab. Chip* **14**, 2978–2982 (2014).

43. Gupta, V. *et al.* 3D printed titanium micro-bore columns containing polymer monoliths for reversed-phase liquid chromatography. *Anal. Chim. Acta* **910**, 84–94 (2016).

44. Sandron, S. *et al.* 3D printed metal columns for capillary liquid chromatography. *Analyst* **139**, 6343–6347 (2014).

45. Do, T. *et al.* Additively Manufactured Full-Density Stainless Steel 316L With Binder Jet Printing. V001T01A017 (2018). doi:10.1115/MSEC2018-6681

46. Do, T., Kwon, P. & Shin, C. S. Process development toward full-density stainless steel parts with binder jetting printing. *Int. J. Mach. Tools Manuf.* **121**, 50–60 (2017).

47. Regmi, B. P. & Agah, M. Micro Gas Chromatography: An Overview of Critical Components and Their Integration. *Anal. Chem.* **90**, 13133–13150 (2018).

48. Bhushan, A. *et al.* Hybrid integration of injector and detector functions for microchip gas chromatography. *Analyst* **135**, 2730–2736 (2010).

CHAPTER 3

ADDITIVELY MANUFACTURING MICROREACTOR WITH EFFICIENT ELECTROTHERMAL CONVERSION

3.1 Introduction

Metal three-dimensional (3D) printing, also referred as additive manufacturing (AM), is considered an emerging, disruptive manufacturing technology, which has been increasingly adopted by industries for high value-added products such as aerospace components or in a low volume production such as customized biomedical implants. The selective deposition of metal powders in a layer-by-layer fashion to build 3D parts is radically different from the conventional manufacturing processes mostly designed for mass production. This technology allows the near net-shape fabrication of extremely complex designs that are difficult or impossible to fabricate with traditional manufacturing techniques. However, another breakthrough technology innately offered by the same metal 3D printing that has not been fully explored is in the fabrication of 'freeformed' heterogeneous materials. One important class of such materials is functionally graded materials (FGMs).

FGMs are advanced engineering materials in which the elemental composition or microstructure progressively varies as a function of position resulting in the gradation in the material properties. They are highly advantageous when the service conditions of a component change with position (or gradient loading) and thus, to become a highly effective media, the material requirements also locally vary accordingly. A notable example includes thermal barrier materials in extreme-environmental applications such as aerospace or nuclear power generation[1], where the structures are exposed to extremely gradient thermal loading within the part. Another example is an orthopedic or dental implant application in which the main body has high strength

and lightweight but its surface should be biocompatible and wear and corrosion resistant[2,3]. Numerous techniques have been developed to fabricate FGMs with compositional gradients, including chemical vapor deposition[4,5], thermal spraying[6,7], combustion synthesis[8,9], and other deposition methods[10,11]. These FGMs are in the form of surface coatings, well supporting gradients over length scales of less than 1 mm. However, these techniques cannot be implemented to fabricate any bulk FGM material made of ceramics and metals[12]. Metal/ceramic FGMs with the compositional variation over larger length scales entail completely different fabrication methods such as centrifugal casting[13,14], tape or slip casting[15–18], spark plasma sintering[19–21], and powder metallurgy[22–24]. A significant amount of research efforts have been made to address the material and processing incompatibilities (due to the thermal shrinkage or expansion mismatch) and residual stress issues. These bulk FGM structures are, without 3D printing technology, too simple in their shape and nearly impossible to attain more complex features and overall shapes that many modern engineering applications require. Recently, AM has received an increasing attention as a promising technique to create near net-shaped FGM structures[22]. Among the various kinds of AM, the directed energy deposition (DED) method, in which metal powder is fed into the melt pool under a moving laser[25] is most widely employed for the preparation of FGMs because the variation of powder composition among layers can be easily achieved by two or more powder feeders. The elemental composition and mechanical properties of such DED-enabled FGMs have been investigated for the various graded metal alloys from Ti-6Al-4V to pure V, 304L stainless steel (SS) to Invar 36[22], Ti-6Al-4V to 304L SS[26], 304L SS to Inconel 625[27], and finally Ti-6Al-4V to Invar 36[28]. The majority of these works are, however, focused on the feasibility of achieving gradual compositional changes in metals without any particular application in mind. The powder

bed systems such as BJP are ideal for the mesoscale fabrication meeting the accuracy and tolerance required for the proposed applications.

The binder jet printing (BJP) process is known to produce parts not suitable for most structural applications due to the insufficient consolidation of the powder in the finished part. In fact, the relative density of metallic parts attainable by BJP may range about 50–60% of a theoretical density, which is substantially lower than the green compacts (up to about 85%) produced by powder metallurgy (P/M) or other AM technologies. The final consolidation step in BJP typically requires the infiltration of a low melting-point metallic material like bronze, which fills the open pores of the printed powder. The presence of the low melting-point material deteriorates the mechanical properties of the printed part, limiting the applications of the BJP technology only for rapid prototyping. However, the disadvantages of BJP process can offer us the novel approach to obtaining metal-ceramic FCGs with tunable electrical, thermal, and mechanical properties combined with a selective-reactive sintering (SRS) process.

In this chapter, we present the combination of SRS combined with the BJP process with stainless steel (SS) to obtain the microreactor with tunable electrical resistivity which could be used as thermal heating component. The SRS process utilizes oxygen as a reactive gaseous environment during sintering and allows the metal powders to partially be converted into more resistive metal oxides. Porosity present in an as-printed BJP part facilitates diffusion of reactants allows them to reach inside the printed structures. The gradiency or heterogeneity in the material properties can be generated when diffusion of the reactants is controlled by the part's geometry or reaction conditions such as temperature and duration. The resultant metal/metal-oxide hybrid structures make the portion of the SS part more resistive, facilitating structural heating and more efficient electro-thermal conversion. A much higher temperature coefficient of resistance for the

metal/metal-oxide structure renders the microreactor to be highly sensitive to the temperature variation and used as a resistance temperature detector (RTD) and hot-wire anemometer for monitoring in-situ flow rates without integrating separate sensors.

3.2. Design considerations – theoretical study

One common microreactor design is shown in Fig. 3.1. An array of posts within the reactor is inserted in a cavity to enhance heat transfer and better distribute thermal energy within fluid stream. During a cold start or when reactions of interest are endothermic, process heating is required to preheat reactants and reactor chamber. Specifically, we are interested in a transient, high-temperature reaction in which rapid heating and cooling of the reactors are important. A good example is a micro preconcentrator (as discussed in Chapter 2) where rapid cyclic heating and cooling are needed for analyte sampling and desorption. Due to the convenience and portability, electrical heating is considered as the most popular heating method and therefore chosen with two possible heating scenarios (see Fig. 3.2): (1) external heating represented as a constant heat flux exerted on both top and bottom reactor surface (referred to as external heating) and (2) direct Joule heating of the post array structures represented as volumetric heat generation within them (referred to as structural heating). We conducted a theoretical investigation on the preferred heating scenario in terms of heating/cooling speed and energy efficiency. Both analytical and computational tools are used to verify the experimental outcome.

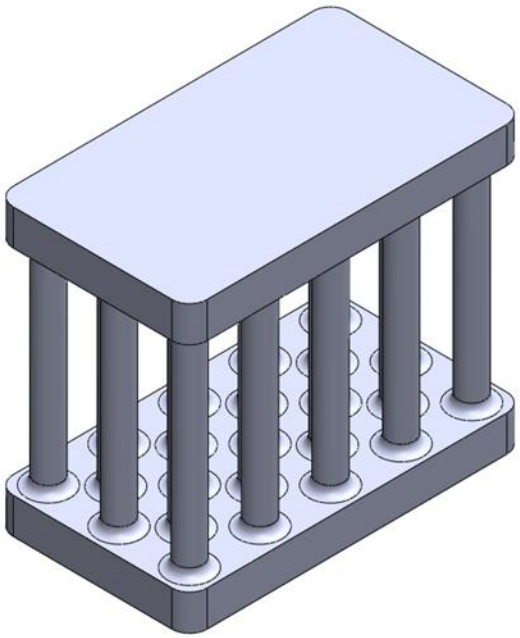

Figure 3.1 A schematic design of a posted microreactor

As for the analytical approach, we could simplify both heating scenarios by considering only a single post from the microreactor and approximating it to a 1-D fin problem. Since the boundary conditions are symmetric, only the half of the post is considered in the problem for both cases. The structural heating case, i.e., a Joule heating through the post, can be modeled by including a volumetric generation term in the governing equation with the top surface subject to a convective boundary condition (Fig. 3.2(a)). In the external heating case (Fig. 3.2(b)), a membrane heater is attached onto the top surface of the microreactor, which can be treated as a constant heat flux.

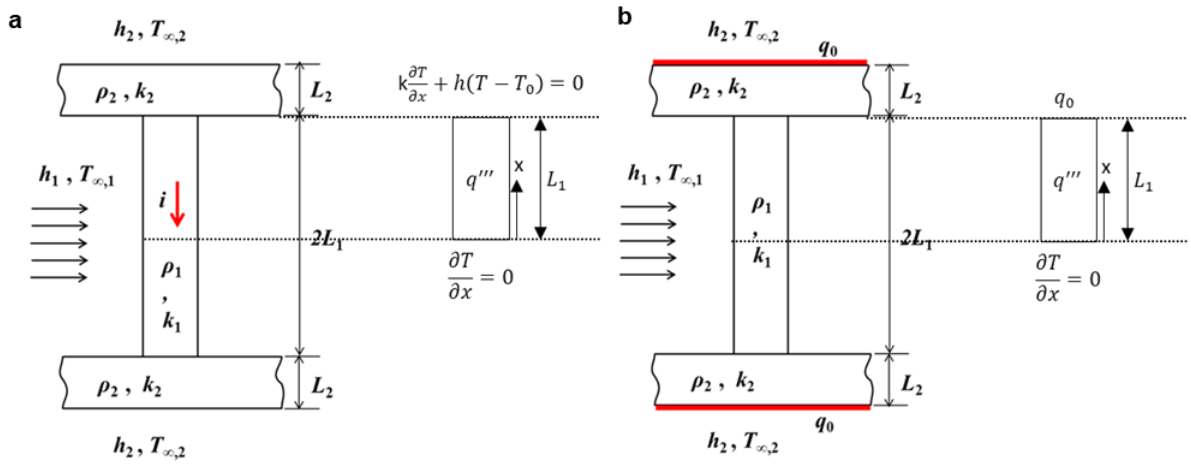

Figure 3.2 Schematics of two different heating scenarios for the posted microreactor: a) direct Joule heating by passing electrical current through the structure; b) external membrane heating at the tip surface

Case 1: Structural heating scenario

The dimensional governing equation is

$$\frac{\partial^2 T}{\partial x^2} - m^2(T - T_\infty) + \frac{q'''}{k} = \frac{1}{\alpha}\frac{\partial T}{\partial t} \qquad \text{in } 0 < x < L,$$

which is subject to the boundary conditions – at $x = 0$, $\frac{\partial T}{\partial t} = 0$ and at $x = L$, $k\frac{\partial T}{\partial x} + h(T - T_\infty) = 0$, and the initial condition, for $t = 0$, $T(x, 0) = T_\infty$. Here, T is the temperature distribution of the post, x is the distant measured from the center of the post, T_∞ is the fluid temperature to which the post is exposed, h is the convective heat transfer coefficient, k is the thermal conductivity of the post, q''' is a volumetric generation rate, and $m^2 = hP/kA_c$ ($P = \pi D$, $A_c = \pi D^2/4$). Using the following dimensionless variables, the dimensionless temperature $\tilde{T} = \frac{T - T_\infty}{(q'''L^2)/k}$, the dimensionless distance $\tilde{x} = x/L$, and the dimensionless time $\tau = \alpha t/L^2$, one can non-dimensionalize the governing equation and boundary/initial conditions. Therefore, the dimensionless mathematical description becomes

$$\frac{\partial^2 \tilde{T}}{\partial \tilde{x}^2} - M^2\tilde{T} + 1 = \frac{\partial \tilde{T}}{\partial t} \quad \text{in } 0 < \tilde{x} < 1,$$

subject to $\frac{\partial \tilde{T}}{\partial \tilde{x}} = 0$ at $\tilde{x} = 0$, $\frac{\partial \tilde{T}}{\partial \tilde{x}} + B_2\tilde{T} = 0$ at $\tilde{x} = 1$, and $\tilde{T} = 0$ for $\tilde{t} = 0$. Here $M = \sqrt{B_i}\left(\frac{L}{V/A_h}\right)$ and $B_i = \frac{h(V/A_h)}{k}$.

Using the separation of variables, one can obtain the following dimensionless temperature solution.

$$\tilde{T}(\tilde{x},\tilde{t}) = \frac{\left(\frac{M-B_2}{M+B_2}e^{-2M+M\tilde{x}} + e^{-M\tilde{x}}\right)}{M\left(1-\frac{M-B_2}{M+B_2}e^{-2M}\right)} - 2\sum_{n=1}^{\infty}\left(\frac{{\beta_n}^2 + {B_2}^2}{{\beta_n}^2 + {B_2}^2 + B_2}\right)\frac{\cos(\beta_n\tilde{x})}{M^2 + {\beta_n}^2}\exp[-(M^2 + {\beta_n}^2)\tilde{t}]$$

$$-\frac{B_2}{M^2(\sinh(M) + B_2\cosh(M))}\cosh(M\tilde{x}) + \frac{1}{M^2}$$

where $\beta_n$satisfies $\beta_n tan\beta_n = B_2$.

Case 2: External heating scenario:

The dimensional governing equation is

$$\frac{\partial^2 T}{\partial x^2} - m^2(T - T_\infty) = \frac{1}{\alpha}\frac{\partial T}{\partial x} \qquad \text{in } 0 < x < L,$$

which is subject to the boundary conditions – at $x = 0$, $\frac{\partial T}{\partial t} = 0$ and at $x = L$, $-k\frac{\partial T}{\partial x} = q_0''$, and the initial condition, for $t = 0$, $T(x,0) = T_\infty$.

Using the separation of variables, one can obtain the following temperature solution.

$$\mathrm{T(x,t)} - T_e = \frac{q_0 L}{k}\frac{\left(e^{-m(L+x)} + e^{-m(L-x)}\right)}{mL(1-e^{-2mL})} - \frac{q_0 L}{k}\frac{e^{-m^2\alpha t}}{m^2L^2}$$

$$- 2\frac{q_0 L}{k}\sum_{n=1}^{\infty}\frac{\cos\left({\beta_n(L-x)}/{L}\right)}{m^2L^2 + {\beta_n}^2}\exp\left[-\left(m^2L^2 + {\beta_n}^2\right){\alpha t}/{L^2}\right]$$

where $\beta_n = n\pi$.

Using the following dimensionless variables, the dimensionless temperature $\tilde{T} = \frac{T-T_\infty}{(q_0'' L)/k}$, the dimensionless distance $\tilde{x} = x/L$, and the dimensionless time $\tau = \alpha t/L^2$, one can non-dimensionalize the governing equation and boundary/initial conditions. Therefore, the dimensionless mathematical description becomes

$$\frac{\partial^2\tilde{T}}{\partial\tilde{x}^2} - M^2\tilde{T} = \frac{\partial\tilde{T}}{\partial t} \quad \text{in } 0 < \tilde{x} < 1,$$

subject to $\frac{\partial\tilde{T}}{\partial\tilde{x}} = 0$ at $\tilde{x} = 0$, $\frac{\partial\tilde{T}}{\partial\tilde{x}} = -1$ at $\tilde{x} = 1$, and $\tilde{T} = 0$ for $\tilde{t} = 0$. Here $M = \sqrt{B_i}\left(\frac{L}{{V}/{A_h}}\right)$ and $B_i = \frac{h({V}/{A_h})}{k}$.

The dimensionless temperature solution is

$$\tilde{T}(\tilde{x},\tilde{t}) = \frac{e^{-M-M\tilde{x}} + e^{-M(1-\tilde{x})}}{M(1-e^{-2M})} - \frac{e^{-M^2\tilde{t}}}{M^2} - 2\sum_{n=1}^{\infty}\frac{\cos\left(n\pi(1-\tilde{x})\right)}{M^2 + n^2\pi^2}\exp[-(M^2 + n^2\pi^2)\tilde{t}].$$

Figure 3.3 illustrates the whole package of the COMSOL simulations of temperature results in balance state for structure heating and external heating. When the same boundary condition, heat energy and same flow rate of gas were applied, the COMSOL results show the temperature

of sample is higher for structure heating approach than external heating. Figure 3.3 demonstrates that the relationship of sample temperature to time changes. From the figures, we could observe that structure heating could heat up the sample faster in a higher temperature than membrane heating approach and achieve the static temperature in short time.

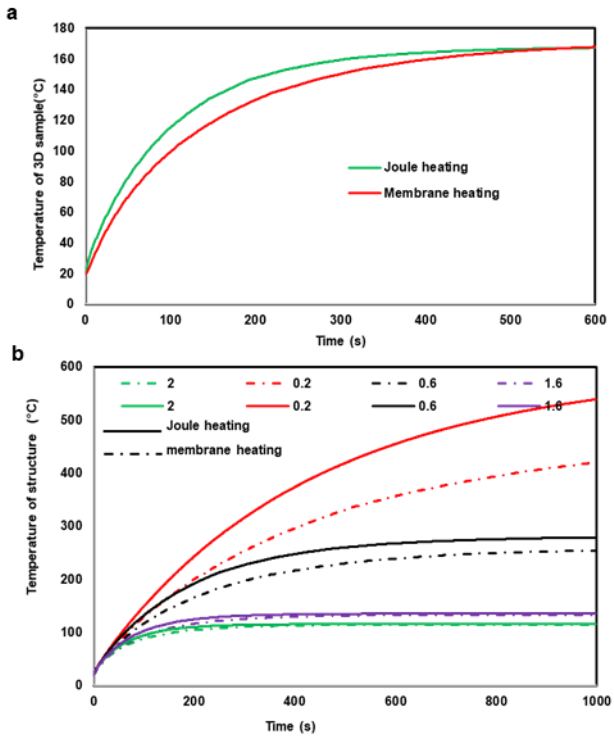

Figure 3.3 COMSOL simulation result for temperature of structure with time of (a) flow rate is 2L/min and power is 1W; (b) different power for different flow rate

3.3 Fabrication challenges and proposed fabrication scheme

3.3.1 Material and fabrication challenges

From the previous discussion, we have theoretically shown that the structural heating method is more energy-efficient and delivers heat to the target regions in the microreactor more rapidly. In order to concentrate heating in the micropost region for better heat transfer characteristics, the ideal design would be to have almost all voltage drops occur across the post

array, meaning that the electrical resistance of the microposts should be much higher than the rest of the structure and circuit. However, if one considers making microreactors out of metal, it is extremely difficult to produce metal microreactors with capability of structural heating because the electrical resistance of the microreactor would be very small. Specifically, considering that the minimum achievable feature size of the common AM equipment is on the order of a few hundred microns (200~500 μm), we will assume the following dimensions for the microreactor: 0.5~2 mm for diameters of each post, 20 ~ 100 for the number of posts, and 10~20 mm for the height of posts. To meet the optimal heater resistance of 20~100 Ω (which does not require high-voltage or high-current power supplies), the electrical resistivity (ρ_e) of the microreactor materials needs to be on the order of 0.1 Ω·m (or electrical conductivity, $\sigma_e \approx 1\sim10$ S/m). Figure 4 shows the electrical conductivities of the common engineering materials from conductors to insulators. The materials whose electrical conductivity falls between 1 and 10 S/m are indeed semiconductors such as silicon, germanium, gallium arsenide, etc. To our knowledge, AM technology for such semiconducting materials with tunable electrical properties has not been reported. If the common AM-compatible metal powders such as SS or Ti are used to build the microreactor of the same dimension, the overall resistance value would be below 0.001 Ω, which is not practical as a heating element. If the common ceramic materials such as alumina or zirconia are used, the resistance value would be too high (> 1 GΩ), which is again not practical. Therefore, lack of the proper resistive materials poses a significant challenge in producing the microreactors with more efficient structural heating capability.

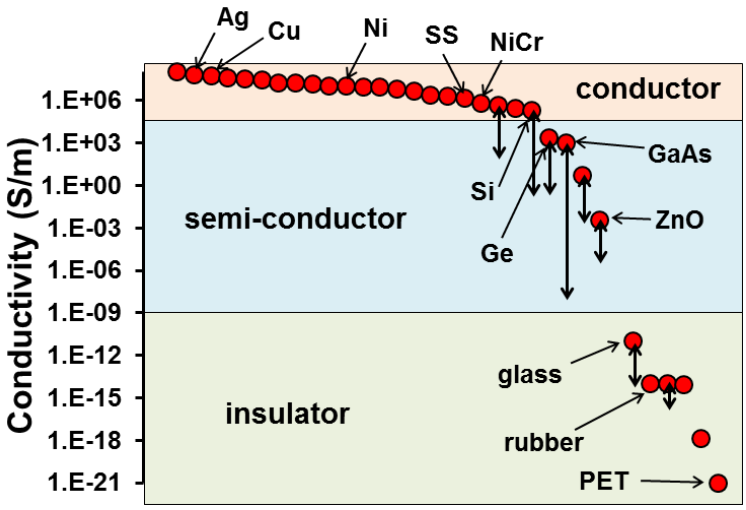

Figure 3.4 Plot of electrical resistivity for the common engineering materials.

3.3.2 Proposed approach – SRS

One potential approach is to employ the mixture of conducting (metallic) powder and insulating (ceramic) powder. This metal-ceramic composite approach to modulating electrical resistivity has been explored by many researchers[29]. There is an important issue when adopting this mixture method for AM. Generally, metal and ceramic powders have very different melting temperatures, i.e., the melting temperatures of the common ceramics like metal oxides/nitrides/carbides are several thousand degrees in Celsius, much higher than those of the raw metals or alloys. Because the sintering temperature is directly related to the melting temperature of the materials, this means that, if excessive energy is applied to sinter ceramic powder, a large amount of metals will evaporate from the melt pool and a net shape of the printed part would be significantly distorted. In case of PBF or BJP, the uniform delivery and spreading of the ceramic and metal powder mixture on a build bed would be also challenging due to the difference in the particle size distribution and its density discrepancy.

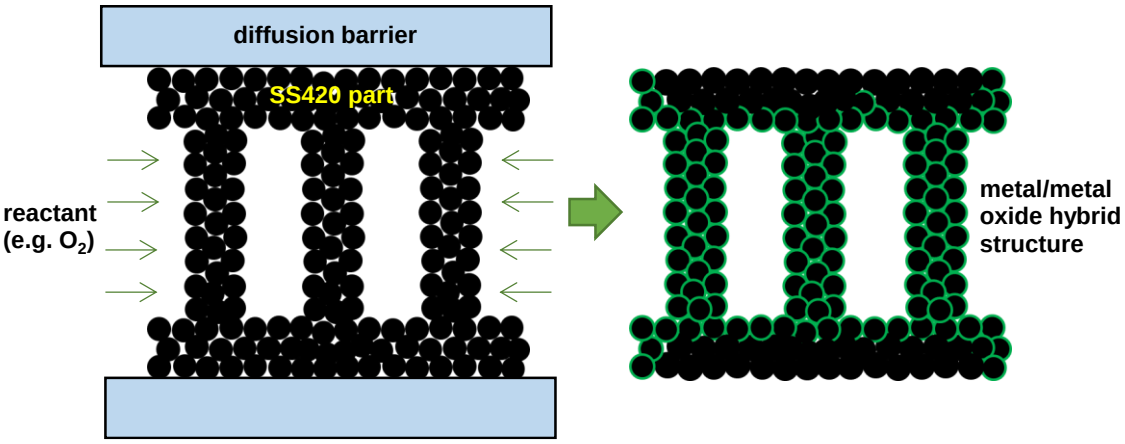

Figure 3.5 A schematic diagram of the selective reactive sintering (SRS) process, which allows the SS420 powder particles in the BJP-printed structure to react with reactive (e.g., oxygen) environment. The resulting structure is a metal/metal-oxide hybrid structure with new physical properties.

Therefore, in this work, we propose Selective-Reactive Sintering (SRS), also known as chemically-induced sintering (CIS), combined with the innovative BJP technique, to obtain metal-ceramic heterogeneous structures with tailored gradient electrical properties. SRS employs thermally-activated chemical reactions between metal powder particles within the printed structure and atmospheric gases. Figure 5 schematically shows the concept of SRS – selective nature of sintering can be realized by impeding reactant diffusion. It is important to note that the compositional gradient materials of the resulting structures (e.g., gradual change from metal to ceramic) can be easily realized by locally controlling the reactant diffusion. Let us take a single post with a circular cross section as an example. Each post consists of numerous microparticles with interstitial spaces that form open pores. A gaseous reactant first reacts with the microparticles situated at the exterior of the post. The material changes – from metal to ceramic - occur due to the chemical reaction while they are being sintered, reducing the porosity of the structure. The concentration of the reactant decreases towards the center of the post because of not only the mass transfer resistance but also the constant depletion of the reactant. Therefore, a progressive

compositional variation is naturally built in the radial direction, i.e., more metallic phase in the core and more ceramic phase in the shell (see the further discussion in later section). Also note that the similar diffusion-reaction phenomenon takes place at the individual particle level. The particle located close to the outer surface of the post is likely to be fully converted to the ceramic phase while that in the center of the post tends to remain more metallic. For example, in such arrangement, the electrical conductivity of the post is controlled by the size of the metallic core as well as the overall conversion.

3.4 Materials and methods

3.4.1 Fabrication procedure

Binder jetting printing (BJP) machine (X1-Lab, ExOne Inc., Huntington, PA) was utilized to fabricate the 3DP sample from stainless steel 420 (SS420) powder (Oerlikon Metco (US) Inc., Troy, MI). BJP is one of the oldest metal 3D printing technologies that print structures by joining metal powder with polymeric binder droplets in a layer-by-layer fashion. The inkjet-like head locally delivers a binder solution to desired locations on the powder bed. The entire process can be broken into several steps as shown in Fig. 3.6. First, a 3D drawing of the device design was created using CAD software and imported into BJP machine. SS420 powder (average particle size ~ 30 μm) was fed to both build bed and powder supply bed. A roller ran across from the powder bed to the build bed and spread the powder uniformly (Fig. 3.6a). Polymeric binder droplets were deposited onto the designated area of the build bed (Fig. 3.6b). The powder spreading and binder phase printing steps were repeated (Fig. 3.6c) in a layer-by layer fashion (after each layer, the building bed stage is lowed while the supply stage is raised) till the part was fully printed. Upon the completion of the printing, the build bed along with the printed part was put into an oven to cure the binder phase at 195°C for 2 hours (Fig. 3.6d). After the loose powder was removed, the

printed part was put in the furnace to decompose the remaining binder phase at 460°C for 2 hours. At this point, the structure is very fragile and could not be handled or used for any application due to the weak property. To perform the proposed SRS process, the 3DP sample was reacted with oxygen at 950°C to convert SS structures into various metal oxide phases (Fe_xO_y and/or Cr_xO_y). An extent of oxidation can be controlled by the oxidation temperature and duration, which drastically changes the structure's physical properties. During the oxidation, a slow ramping rate (1ºC/min) was used to ensure that oxygen diffuses into the inner powder particles in each post. To minimize oxidation of the top and bottom sides of the reactor, we placed the sample between quartz plates. While our intention was to selectively oxidize the post array, the quartz plates couldn't prevent oxidation from taking place on the top and bottom surfaces. Therefore, both surfaces of

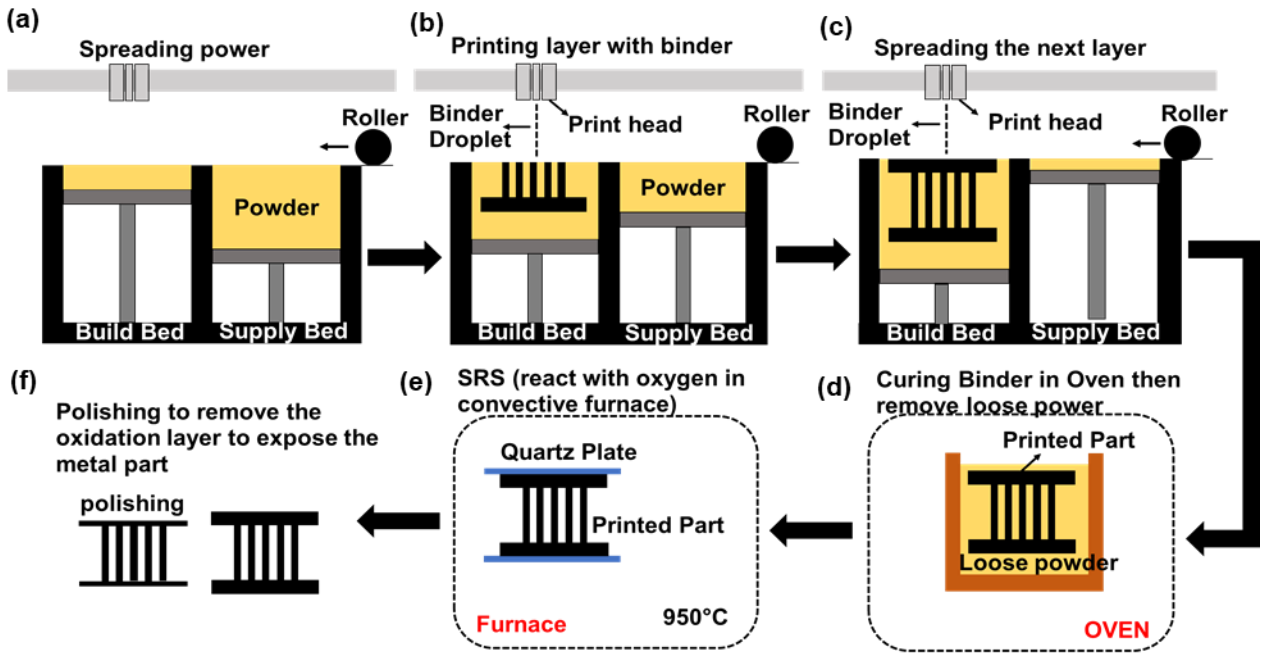

Figure 3.6 Schematic figure of BJP process of microreactor design and SRS process with oxygen.

the microreactor were polished to remove the surface oxide layers and expose the underlying metallic part for electrical contacts. To reduce the contact resistance, a thick layer (~ 5 μm) of copper was sputtered (~ 10^{-2} mbar of the background pressure) on both sides' surfaces. Electrical wires were soldered at the corner of the Cu layer for further testing.

3.4.2 Materials characterization

Scanning electron microscopy (JEOL 6610LV) was performed on the cross-section of the post after the SRS process to investigate an extent of the oxidation through the post and powder particles. Energy Dispersive X-ray Microanalysis (EDS) was also performed in the same instrument for elemental analysis and to obtain compositional mapping from the surface. X-ray diffraction (XRD, RIGUKA) was conducted to reveal the crystal structure and chemical composition of the metal oxide phases formed after the SRS process. The weight of the samples was measured using an analytical balance (XS205DU, Mettler-Toledo Inc.).

3.4.3 Heating experiments

External heating approach – The membrane heaters were fabricated by sandwiching a serpentine pattern of a NiCr wire (40 AWG, Coil Society Inc.) with two thin (~ 50 μm) layers of Kapton® tape (1-inch wide, U-Line). The heater temperature was monitored with resistance-temperature detectors (RTDs) that were also custom-made in a similar manner using a NiFe wire (40 AWG, Coil Society Inc.). The membrane heater and RTD were integrated by placing them on top of each other with an adhesive layer. The fabrication details for the heater and RTD can be found in Chapter 2. Each microreactor was sandwiched between two membrane heaters/RTD. The same power was applied to both heaters to be able to apply for the symmetric boundary condition.

Structural heating approach – Two wires (24 AWG, Belden Inc.) were soldered onto the copper layer of each side of the microreactor. Four wires were used for heating and sensing and also help

to reduce any potential contact resistance. A constant DC power supply (100 V, 3 A, Konrad Inc.) was connected through a custom-made PID circuit to maintain the microreactor temperature at a constant level. Since the microreactor temperature can be monitored by measuring a change in electrical resistance of the microreactor. The resistance-temperature relationship of the microreactor was separately calibrated in an oven.

Visualization – To reduce heat loss to ambient during visualization experiment, a 3D-printed plastic package along with a ceramic insulation mat was employed to insulate the five faces of the microreactor. In-situ variation of the microreactor temperature was visualized at the open side by means of an IR camera (SEEK Thermal Pro). The IR temperature was cross-checked by monitoring the resistance readings from the microreactor or RTD sensor.

3.4.4 Flow sensor experiments

The calibrated temperature-resistance relationship of the microreactor can be used for both temperature and flow rate sensors. The microreactor sample was placed in the flow-cell 3D-printed package (VeroWhite, Connex 350 3D printer) for fluidic connections. Insulation layers (ceramic fiber mat) were used between the microreactor and package to reduce the heat loss and protect the package from high-temperature working conditions. The package was designed with two separate parts that were assembled to fully enclose with inlet and outlet ports. The inlet port was connected to a flow meter (0 ~ 4 L/min, Omega Inc.) to control a dry N_2 flow (99.99%, Airgas Inc.). The outlet port was left open to ambient with the thermocouple inserted to measure the outlet temperature of the N_2 flow. Like hot-wire anemometers, the temperature of the microreactor would change as a function of the flow rates – the higher the flow rate, the cooler the reactor temperature for a given power. In fact, we explored two sensing modes: constant power vs. constant temperature. In the former mode, the electrical power applied to the heater was fixed, and the

reactor temperature was measured as a function of the flow rate. In the latter, as the flow rate changes, the power required to maintain the same reactor temperature was measured.

3.5 Results and Discussion

3.5.1 Fabrication results and resistivity measurements

Figure 3.7 shows the photographs of a SS420 microreactor at various stages of the sample preparation. An as-printed BJP part of the microreactor (whose overall dimension is 19 mm, 11 mm, and 16 mm) was shown in Fig. 3.7a. Once the binder phase was fully removed during the burn-out step, the sample became very fragile and weak due to a high level porosity and weak adhesion among powder. Figure 3.7b shows the sample after oxidation at 950°C for 6 hours. The dark teal color of the sample indicates that the surface level of the microreactor was fully oxidized. In order to make the sample oxidized uniformly, low ramping rate (1°C/min) was adopted to heat up 3DP part to 950°C for oxidation. The metal oxide was expanded to larger dimension (shows in Table 3.1, the diameter and the height of the post column were increased) and the color of microreactor became dimer (Fig. 3.7b) due to the oxidation of metal powder. At this point, the 3DP sample is completed with much stronger property and ready for further applications. From Figure 3.7c, surface polishing was needed to expose the metal part and make the connection with power supply for Joule heating approach. In order to have uniform connection for individual post to distribute the energy, thin layer of copper (~5μm) was coated on the top of the sample surface (Fig. 3.7d). Soldering was used to make the strong connection between the wire and 3DP to conduct the current so that transfer the heat.

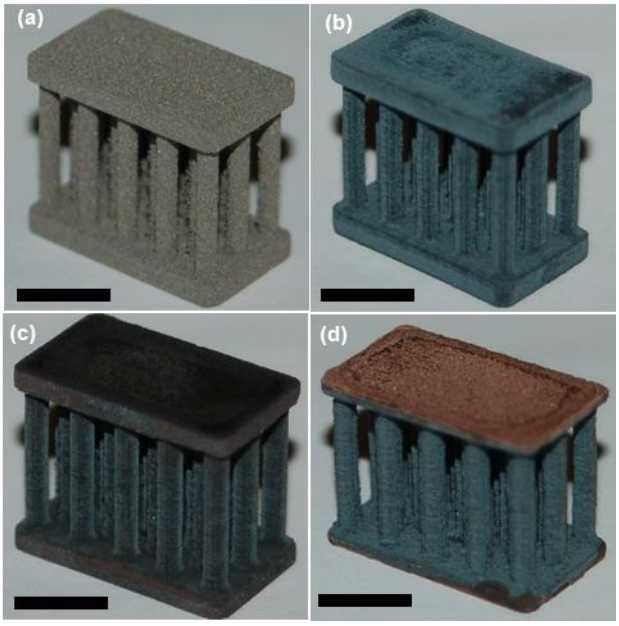

Figure 3.7 Photographs of a BJP-printed microreactor: (a) after printing, (b) after oxidation, (c) after polishing, (d) after copper coating for electrical contact. Scale bar: 1mm

Since the metal oxides (Fe_xO_y and/or Cr_xO_y) has a lower density than SS, the part expands upon oxidation. The resultant dimensional changes were monitored with the optical microscope (Nikon LV100) and shown in Table 1. About 9.2 ~ 16.5% of the size increase was observed, and the volume expansion would be related to the local conversion of metal to metal oxides.

Table 3.1 dimension of microreactor after printing and after oxidation

Sample dimension	Diameter of post (mm)	Length of post (mm)	Length of plate (mm)	Height of plate (mm)
Before oxidation	1.6	12.05	18.69	1.96
After oxidation	1.86	13.17	20.56	2.25
Dimension increase	16.5%	9.24%	10%	11.7%

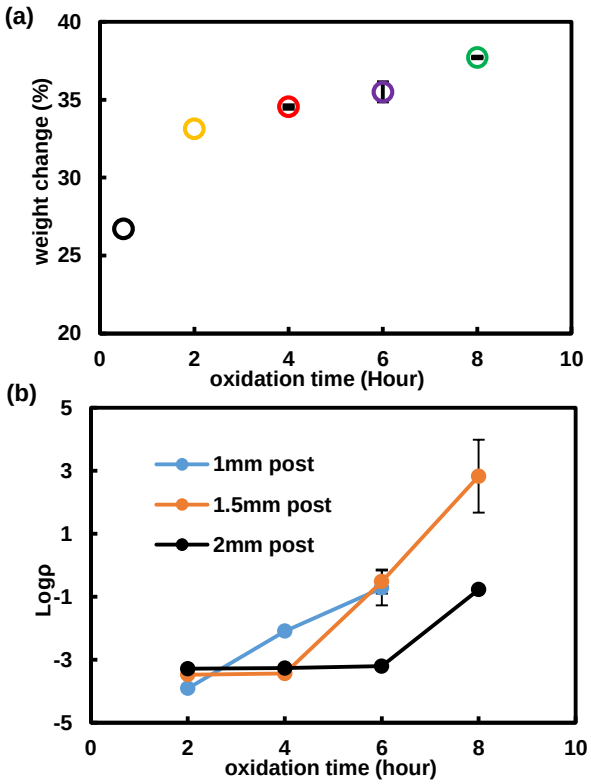

Figure 3.8 weigh change of microreactor at different oxidation time

Figure 3.8 shows the weight change of the microreactor samples as a function of different oxidation durations when the oxidation temperature was set at 950°C. After binder phase was completely burnt out, the structure became highly porous as reported by our previous study[30]. When this structure is exposed to the oxygen environment at elevated temperatures, oxygen molecules diffuse through the pores between powder particles and start to react with the particle surface. The sample weight increases by about 26.7% when oxidized for the initial 30 min at 950°C (ramping time included). The weight gain is around 33.1% for 2 hours of oxidation, indicating a continuous growth of the oxidation layer on the powder surface. However, the weight growth rate was significantly slowed down after 4 hours (i.e., around 34.55%, 35.5%, and 37.7% weight increase for 4, 6, and 8 hours of oxidation, respectively). The slower weight gain is expected

because the existing oxide layer acts as a diffusion layer to oxygen molecules, impeding further oxidation of the metal core.

An electrical resistivity change of the SRS sample is shown in Fig. 3.8(b) as a function of different oxidation durations. For the microreactor with the same post dimension, the resistivity increases with the oxidation duration, marking 6 orders of magnitude increase in resistivity in case of the 1.5-mm sample. The resistivity of the sample primarily depends on the extent of oxidation, i.e., the thickness of the metal oxide layer vs. the size of the metallic core. When a longer oxidation time was adopted, more powder particles were oxidized more extensively. As the metal oxide layer becomes thicker, it is harder for electrons to go through the depletion area (metal oxide layer), resulting in a larger electrical resistance. The post size influences the extent of oxidation. Figure 3.8b suggests that the resistivity of the 1.5- and 2-mm post structures does not change from 2 to 4 hours of oxidation time while that of the 1-mm sample increases significantly (2 orders of magnitude increase). An onset oxidation time at which the resistivity significantly changes depends on the post diameter. For the microreactor with a smaller post size, the metallic core gets converted at a shorter oxidation time. The onset oxidation times for the 1-mm, 1.5-mm, and 2-mm samples are 2, 4, and 6 hours, respectively. For the 1.5 mm post sample, the resistivity increases from 0.000338 Ω.m for 2-hour oxidation time to 0.0007247.1 Ω.m for 4-hour oxidation time while it jumps to 0.179 Ω.m for 6-hour oxidation time. This behavior of a sudden increase in resistivity may be related to the unoxidized (or less-oxidized) core size. Since the metallic core remains unoxidized (however small the metallic core is), the electron finds their way to flow (percolation network) without much resistance, i.e., relatively small electrical resistivity. When the oxidation duration is long enough to oxidize powder particles in the core/center of the post, the surface of the majority of metal powder particles within the post is essentially oxidized, leading to a

significant increase in resistivity. Therefore, a sharp increase in resistivity occurs at a point when the powder residing in the last conducting percolation path becomes oxidized on their surfaces. At this point, electrons are forced to conduct through the metal oxide barriers. The electrical conduction through the hybrid metal/metal-oxide structures (in a powder level, a metal core with an oxide shell) can be modeled as a series of parallel and series resistances. Since the resistivity of SS is 7~9 orders of magnitude smaller than that of iron oxides/chrome oxides, the total resistance will be dominated by the thickness of the oxide shell and the number of the oxide-oxide contact resistances. The contact area also needs to be factored in as the actual contact area is smaller than the nominal area. A quantitative modeling of the electrical behavior requires more in-depth study, and therefore, here we focus on the qualitative description of the SRS (oxidation) processes through the post structure and within SS powder.

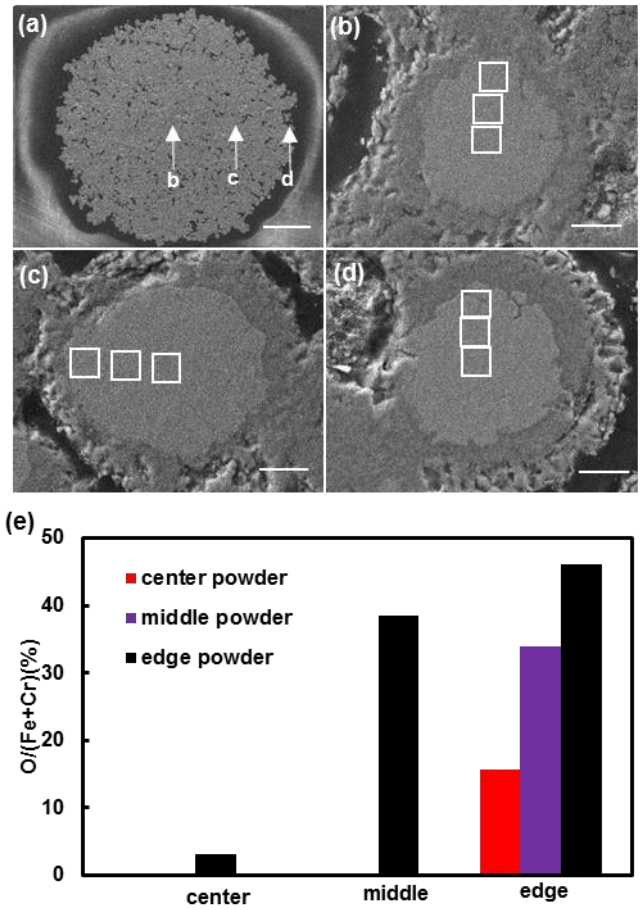

Figure 3.9 (a) SEM image of the cross-section of a BJP-printed SS420 column/post (1.5mm diameter) after the SRS process; SEM images of the single powder particle located in the center (b), middle (c), and at the edge (d) of the column in (a); (e) EDS elemental scan revealing the oxygen/(iron and chromium) ratio of each location for each powder, which proves the property control of the structure. Scale bar: a: 500 µm; b-d: 10 µm.

Figure3. 9(a) shows the SEM image of the cross-section view of the whole post column (1.5-mm sample) with the 2-hour SRS/oxidation process. It also shows the gap between the post and polymer encapsulating material. Each SS powder particle situated at different locations (indicated by the letters b, c, and d in Fig. 3.9(a)) is further focused – (b) powder in the center area of the post, (c) powder in the half-way between the center and edge of the post, and (d) powder in the edge area of the post. All of the images (b-d) show that the SS powder particles were oxidized

and converted to the hybrid structure with the metallic core and oxide shell. It also shows that the powder particles are connected by the oxide layer. The SEM images show that the powder surface was oxidized to form an oxidation shell. It was well established that there are internal and external growths for the oxidized layer when metal was oxidized[31–33]. The growth rate of the internal oxide layer depends on the rate of oxygen diffusion. For the powder at the edge area, oxygen was sufficient and most of them could diffuse into the oxide layer so that the growth rate of oxide layer was fast and the more internal powder was oxidized than the center powder since the oxygen was less surrounding the center powder. It could be predicted that the thickness of oxide layer of edge powder should be larger than the center powder. The EDS analysis supports this conclusion that the oxygen presents in the center part and middle part of the powder for the edge powder, indicating the oxide layer for edge powder includes the middle and center part, while the oxide layer is just the edge part of the powder for the center and middle powder. The oxygen ratio could be obtained from EDS results demonstrated highest at the outside oxidation shell, following the edge area and then middle area and center area. And for center powder and middle powder, there is no oxygen shown in the center area and middle area, indicating that just outside surface of powder was oxidized and no oxygen diffuse into inside of powder. For the edge powder (Fig. 3.9d), the O/(Fe+Cr) ratio is 3.08%, 38.46%, and 46.12% for the center area, middle area, and edge area, respectively. For the center powder (Fig. 3.9b) and middle powder (Fig. 3.9c), the O/(Fe+Cr) ratio is 0%, 0%, 15.58% and 0%, 0%, 34% for the center area, middle area and edge area. These analysis data are clearly proven the previous conclusion of diffusion theory of metal oxidation process.

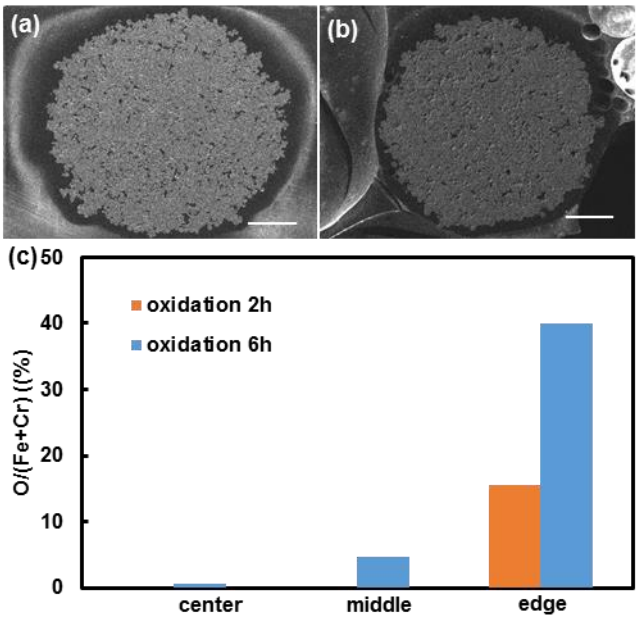

Figure 3.10 SEM images of the cross section view of SS420 post/column (1.5 mm diameter) for oxidation 2 hours (a) and oxidation 6 hours (b); (c) EDS elemental analysis of the oxygen/(iron and chromium) ratio of each location of the center powder for 2h and 6h oxidation. Scale bar: a and b: 500 µm.

As we demonstrated in weight change and resistance section, when oxidation time varies from 2 hours to 6 hours, the weight increase from 31.1% to 35.5%, while the resistance changes from 0.000338 Ω.m to 47.1 Ω.m. From Fig. 3.10a and 3.10b, we could observe that it is more porous of the 3DP for oxidation 2 hours and metal oxide layer would grow outside and fill in the pore with 6 hours oxidation. And Figure 10c shows that there is oxygen present in the center area and middle area of powder in the center of the post for 6 hours oxidation sample, which indicates the oxygen diffuse to the center area of the powder so more metal oxide in this sample. Our hypothesis is that the metal oxide layer would grow outside and merge together and oxygen would diffuse inside the powder to react with powder and form metal oxide with longer oxidation time. The small weight (4.4%) increase for longer oxidation time result from the growth of outside metal oxide layer which is small amount. For resistivity of sample, since the metal oxide layer was grown

outside and formation of metal oxide inside the powder, the thickness of the metal oxide increase of the powder is much thicker, which induce the hugh increase of the resistivity of microreactor.

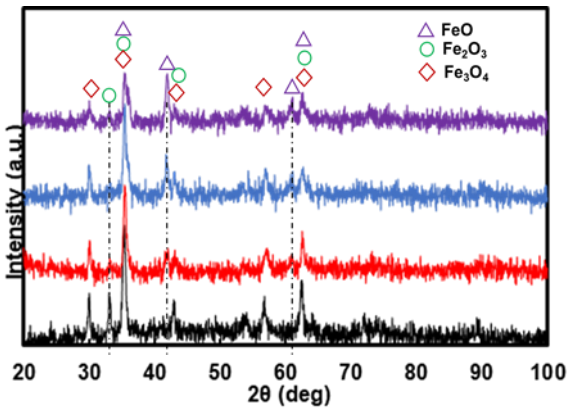

Figure 3.11 XRD pattern of Fe_3O_4 at different thickness of oxidation sample

Figure 3.11 presents the X-ray diffraction (XRD) pattern information of sample to demonstrate the oxidation level for the different area (center area, middle area and edge area) in the sample. From the patterns, a series of characteristic peaks (220), (311), (400), (422), (511), (440), which are in well accordance with the inverse cubic spinel phase of Fe_3O_4, were observed. In this sense, all the patterns are very similar, meaning crystallization of Fe_3O_4 is same at the different thickness level in sample. From edge to center, there are one peak disappear and two extra peak occur. The peak position shows that the disappeared peak is for Fe_2O_3 and the arising peak is for FeO. Based on the oxygen diffusion theory we hypothesized above, oxygen amount would decrease from edge surface part to center part, causing more metal oxide formed at the edge and less in the center, which was supported by XRD analysis. The peak represents the intensity of the material and large peak means more amount of the material. It is shown that the intensity of Fe_2O_3 was decreased from edge to center and FeO increased from edge to center.

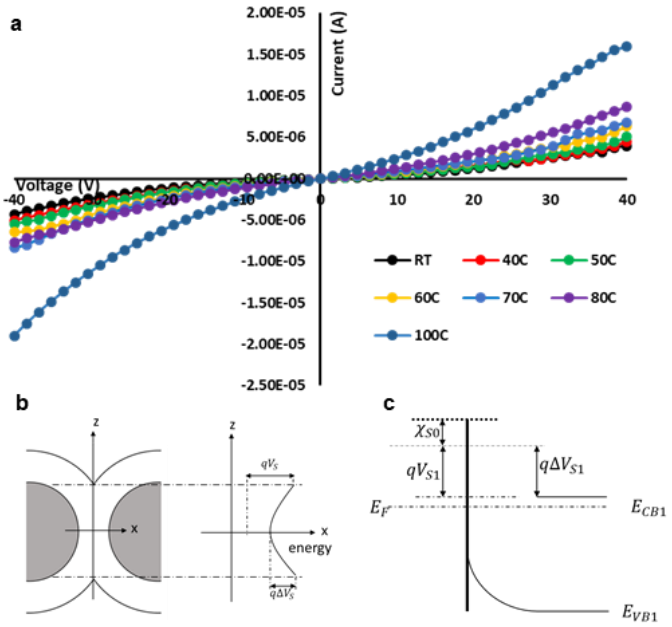

Figure 3.12 (a) I-V characteristics of the SS420 microreactor sample (1.5-mm diameter, oxidized for 6 hours) as a function of the sample temperature; (b) a schematic showing the interface between two metal/metal-oxide particles after the SRS process; (c) energy band bending after metal and metal oxide contact.

The graph in Figure 3.12a shows I-V characteristics of 3DP oxidized sample at different temperature condition. It presents the trend that the resistance was decreased from 9.35MΩ to 2.1MΩ when the temperature of sample heated from room temperature to 100°C, which illustrates the semiconductor behavior (resistance decreases with temperature increases). These I-V curves are symmetrical and nonlinear, implying that there is no bias and have Schottky barrier. With temperature increased, when the same voltage was applied, the current (I) passing through the Schottky barrier junctions is much more nonlinear function of voltage, meaning more semiconductor behavior was observed.

Figure 3.12b shows the situation of metal powder and metal oxide contact after oxidation. The XRD pattern shows the metal oxide is Fe_3O_4 so the metal-semiconductor contact is SS/Fe_3O_4

contact. When the metal powder and the semiconducting metal oxide layer are brought in contact, the electrons from the n-type Fe_3O_4 semiconductor are flowing to the metal powder resulting in an depletion layer at the interface in the semiconductor. From the energy band model point to view, this situation is described by the building of a band bending in the semiconductor ($q\Delta Vs$).

The I-V curves in Figure 3.12a result from back to back Schottky Barrier from the depletion layer (Figure 3.12b) in metal oxide part formed between metal powders. From SEM images, the metal oxide layer thickness (barrier width) is much larger than the mean free path of electrons, the conduction through this structure was dominated by diffusion theory. The current density J is given by

$$J = q[n(x)\mu_n E(x) + D_n \frac{dn(x)}{dx}]$$

Where $\mu_n = \frac{q}{k_0 T} D_n$ and $E(x) = -\frac{dV(x)}{dx}$, V(s) represents the electrostatic potential and n(x) the electron density at the distance x from the interface, μ_n is the carrier/electron mobility and q is the elementary charge.

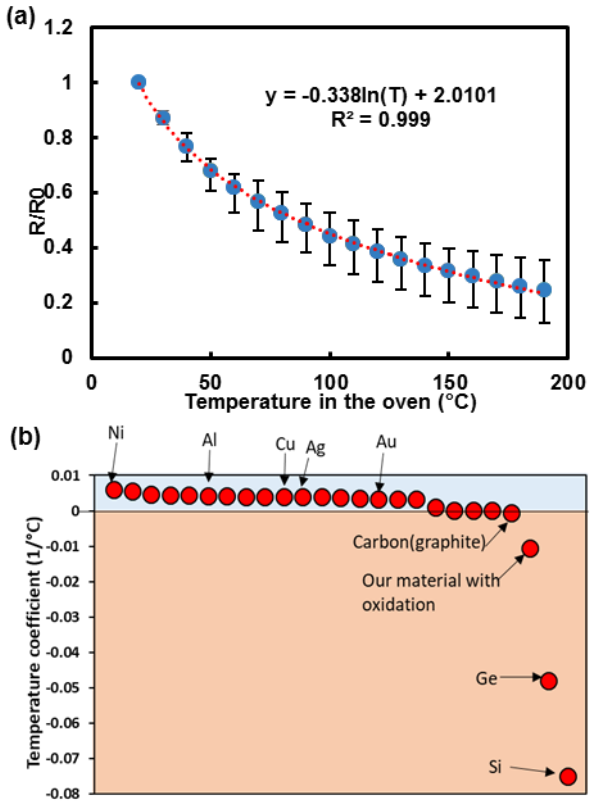

Figure 3.13 (a) Temperature-resistance relationship (calibration performed in an oven) of the microreactor sample (SRS conditions at 950C, 6 hours); (b) a plot of the TCR values for the common engineering materials

Figure 3.13a shows the resistance ratio (R/R_0) with temperature of different samples. With the temperature increased, the resistance of sample decreased, showing semiconductor behavior, opposite performance of metal. The curve is nonlinear which means the temperature coefficient of resistance (TCR) is variable with temperature change. The TCR α is given by

$$R = R_0[1 + \alpha(T - T_0)]$$

The trend relationship in the plot between R/R_0 to temperature could be obtained from the experiment results is

$$\frac{R}{R_0} = -0.338\ln(T) + 2.0101$$

Where R_0 is the original resistance at room temperature. This equation could be adopted to express the resistance with temperature relationship of this material, the obtained results calculated from this equation and from experiment is highly close (R^2=0.999). The resistance of sample could be predicted at higher temperature using this equation, for example, the R/R_0 would be 0.08222 when temperature is 300°C. Average TCR α of this material is around -0.0102(1/°C), which is much larger than TCR of Ni (~0.006 /°C) that is the largest TCR material among common engineering metal. Thanks to this high TCR, this material could be used as resistance temperature detector (RTD) to monitor the temperature change by measuring the resistance change. The measured temperature is within 1% of the experimental error measured in Celsius degree in the oven. The error bar in the plot represents R/R_0 deviation for different sample at certain temperature condition. With the temperature increase, the prediction of microreactor resistance would have more error deviation.

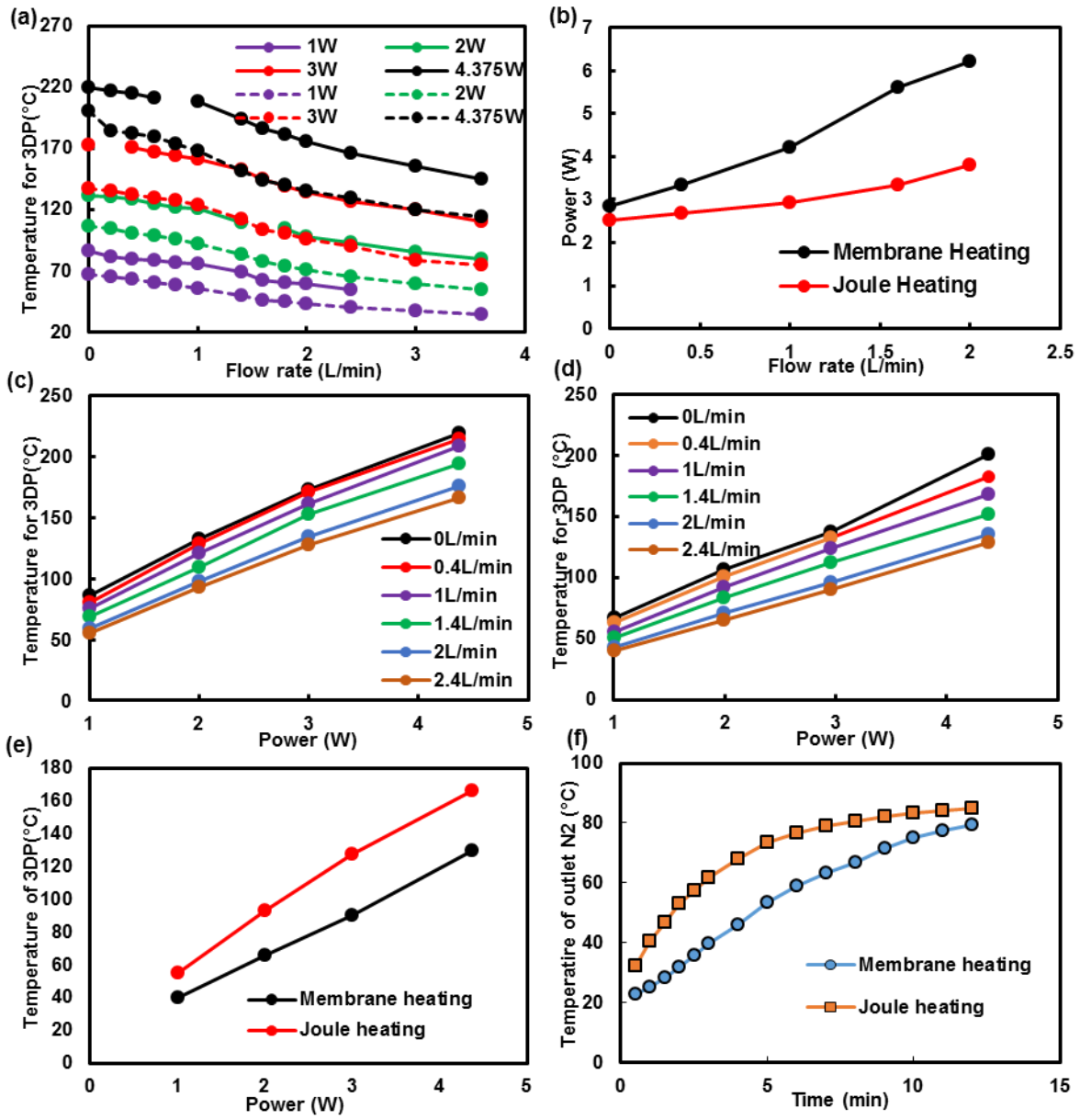

Figure 3.14 (a) A required power to maintain the same temperature of microreactor to different flow rate for two heating approach; (b) temperature of 3DP microreactor to different flow rate when different power was applied; (c) Temperature of 3DP microreactor to different power with different flow rate for Joule heating; (d) Temperature of 3DP microreactor to different power with different flow rate for membrane heating; (e) Temperature of 3DP microreactor to different power when flow rate is 2.4L/min for two heating approach; (f) dry N_2 temperature measurement at the exit of 3DP microreactor with insulated packaging (4.2W of applied power and 1L/min of the N_2 flow rate)

As we discussed in the previous section, membrane heating and Joule heating were adopted as heating scenarios for exchanging heat energy. Due to the high TCR, this material could be used as flow rate sensor. With the changing flow rate, the temperature of the sample would vary since heat capacity coefficient (h) changes. One key factor of heat efficiency is power consumption to heat up the sample at certain temperature. The relationship between temperature of 3DP sample and flow rate of dry N_2 was presented in Figure 3.14a when power was applied. The solid line represents Joule heating approach, which could obviously heat the sample into higher temperature compared with membrane heating (dash line) when same power was applied at the same flow rate. Same color line was known the same power. For example, when 3W power was applied to sample, the temperature of 3DP achieves around 134.8°C at flow rate of 2L/min while the temperature of 3DP obtains around 96.11°C at the same condition. From Figure 3.14a, we could observe that temperature of sample was higher when more power was applied to sample for both membrane heating and Joule heating approaches. With the flow rate of N_2 increased, the temperature of sample has the same decreased trend for both heating approaches because more heat energy was lost and purged away which increase the heat convection between 3DP sample and surrounding environment. The temperature of 3DP sample decrease from 121°C to 97.9°C when flow rate changes from 1L/min to 2L/min for Joule heating at 2W power, while temperature ranges from 92.3°C to 71°C for membrane heating at the same condition. Figure 3.14a obviously demonstrated that structure heating scenario has more efficiency to heat up the structure than membrane heating at the same flow rate and the temperature of sample could decrease with the flow rate increasing, which can be used as flow sensor to monitor temperature of sample and correlated to the flow rate.

Figure 3.14b demonstrates the power consumption applied to 3DP sample to maintain the temperature at 137°C when different flow rate of dry N_2 was purged to the sample. The result shows that the power consumption increased because more heat would be lost with larger flow rate. The power consumption by Joule heating is smaller than membrane heating when same flow rate was adopted, implying Joule heating is much more effective than membrane heating. For example, at 1L/min of flow rate, 2.92W was applied to sample for Joule heating to maintain temperature at 137°C while 4.21W was needed to apply for membrane heating. Figure 14b also present the power consumption difference between these two heating approach would be enlarged with increasing flow rate to maintain same temperature of sample, 0.314W difference at flow rate of 0L/min to 2.24146W difference at 2L/min. Therefore, with higher flow rate of gas, Joule heating would consume much less energy compared with membrane heating in order to obtain same temperature.

Figure 3.14c-d illustrate the sensitivity of flow sensor caused by Joule heating and membrane heating approaches. Sensitivity is a key criterion to distinguish the sensor how fast or how large the response or signal changes when the condition of sensor varies. From Fig. 14c and d, we could observe that the change of 3DP temperature is almost linear with the change of power applied to sample for flow rate from 0L/min to 2.4L/min, indicating the sensitivity is constant and the temperature of sample could be predicted with power changes. Figure 14e shows temperature of 3DP response to different powder when the same flow rate was adopted at 2.4L/min for two heating scenarios. The results demonstrated that the slope of the line for Joule heating is larger than membrane heating, which means the sensitivity is higher to monitor the 3DP temperature for Joule heating approach when the same power and same flow rate was applied to sample.

A constant flow of room-temperature N_2 was fed into the inlet, and N_2 temperature was measured at exit (shown in Fig 3.14f). This test manifests the effectiveness of the microreactor as a process unit. The Joule heating of microreactor is superior in terms of the transient response. After 3 min, the increase in N_2 temperature at exit was more than 100% larger for the Joule heating method (room temperature to 62°C) compared to the external membrane heating method (room temperature to 40°C).

3.6 Conclusion

A robust and facile approach was investigated by Binder Jet Printing (BJP) by stainless steel powder combined with selective reactive sintering (SRS) process in oxygen to fabricate 3DP microreactor with tunable electrical property which is critical for structure heating. The performance of the microreactor as a process heating unit in terms of steady-state and transient operation condition was studied from modeling and microstructure analysis for Joule heating and membrane heating. And the results demonstrate Joule heating was adopted as heating scenario to maximized the heat transfer rate. The growth of the metal oxide layer process with different oxidation time condition was studied and discuss hypothesis of the weight change and resistivity change during the oxidation process. Longer oxidation time make the microreactor showing more semiconductor behavior, resulting from the thick metal oxide. With long SRS process in oxygen, a microreactor with high temperature coefficient of resistance (TCR) (~-0.102/°C) was obtained and shows the electrical conductance of microreactor is highly sensitive to a temperature variation. Thanks to the high TCR, our fabricated microreactor was used as resistance temperature detector (RTD) at high temperature. By monitoring the resistance of microreactor, we can estimate the reactor temperature inside. Moreover, a change in a flow rate can be detected by measuring the

resistance change. If the microreactor is properly calibrated with various flow rates and heating condition, it can measure the absolute flow rate.

REFERENCES

REFERENCES

1. Zinkle, S. J. & Was, G. S. Materials challenges in nuclear energy. *Acta Mater.* **61**, 735–758 (2013).

2. Oshida, Y., Tuna, E. B., Aktören, O. & Gençay, K. Dental Implant Systems. *Int. J. Mol. Sci.* **11**, 1580–1678 (2010).

3. Navarro, M., Michiardi, A., Castaño, O. & Planell, J. . Biomaterials in orthopaedics. *J. R. Soc. Interface* **5**, 1137–1158 (2008).

4. Elkasabi, Y., Lahann, J. & Krebsbach, P. H. Cellular transduction gradients via vapor-deposited polymer coatings. *Biomaterials* **32**, 1809–1815 (2011).

5. Design of SiC/C Functionally Gradient Material and Its Preparation by Chemical Vapor Deposition. Available at: https://www.jstage.jst.go.jp/article/jcersj1988/97/1125/97_1125_539/_article/-char/en. (Accessed: 17th April 2019)

6. Sioh, E. L. & Tok, A. I. Y. Functionally Graded Materials using Plasma Spray with Nano Structured Ceramic. *J. Phys. Conf. Ser.* **419**, 012048 (2013).

7. Majumdar, J. D. & Manna, I. Development of Functionally Graded Coating by Thermal Spray Deposition. *Therm. Sprayed Coat. Their Tribol. Perform.* 121–162 (2015). doi:10.4018/978-1-4666-7489-9.ch005

8. Niedzialek, S. E., Stangle, G. C. & Kaieda, Y. Combustion-synthesized functionally gradient refractory materials. *J. Mater. Res.* **8**, 2026–2034 (1993).

9. Stangle, G. C. & Miyamoto, Y. FGM Fabrication by Combustion Synthesis. *MRS Bull.* **20**, 52–53 (1995).

10. Sattar, N. *A Review For Functionally Gradient Materials Manufacturing And Useful Application*. (2018).

11. Suryakumar, S. & Somashekara, M. A. Manufacturing of functionally gradient materials by using weld-deposition. in *Proceedings of the 1st International Joint Symposium on Joining and Welding* (ed. Fujii, H.) 505–508 (Woodhead Publishing, 2013). doi:10.1533/978-1-78242-164-1.505

12. Chmielewski, M. & Pietrzak, K. Metal-ceramic functionally graded materials – manufacturing, characterization, application. *Bull. Pol. Acad. Sci. Tech. Sci.* **64**, 151–160 (2016).

13. Rajan, T. P. D., Pillai, R. M. & Pai, B. C. Centrifugal casting of functionally graded aluminium matrix composite components. *Int. J. Cast Met. Res.* **21**, 214–218 (2008).

14. Xie, Y., Liu, C., Zhai, Y., Wang, K. & Ling, X. Centrifugal casting processes of manufacturing in situ functionally gradient composite materials of Al-19Si-5Mg alloy. *Rare Met.* **28**, 405–411 (2009).

15. Moya, J. S., Sánchez-Herencia, A. J., Requena, J. & Moreno, R. Functionally gradient ceramics by sequential slip casting. *Mater. Lett.* **14**, 333–335 (1992).

16. Navarro, A., Whatmore, R. W. & Alcock, J. R. Preparation of Functionally Graded PZT Ceramics Using Tape Casting. *J. Electroceramics* **13**, 413–415 (2004).

17. Yeo, J.-G., Jung, Y.-G. & Choi, S.-C. Design and microstructure of ZrO2/SUS316 functionally graded materials by tape casting. *Mater. Lett.* **37**, 304–311 (1998).

18. Yeo, J.-G., Jung, Y.-G. & Choi, S.-C. Zirconia-stainless steel functionally graded material by tape casting. *J. Eur. Ceram. Soc.* **18**, 1281–1285 (1998).

19. Fujii, T., Tohgo, K., Isono, H. & Shimamura, Y. Fabrication of a PSZ-Ti functionally graded material by spark plasma sintering and its fracture toughness. *Mater. Sci. Eng. A* **682**, 656–663 (2017).

20. Chaubey, A. K. *et al.* Fabrication and characterization of W-Cu functionally graded material by spark plasma sintering process. *Fusion Eng. Des.* **135**, 24–30 (2018).

21. Feng, H., Meng, Q., Zhou, yu & Jia, D. Spark plasma sintering of functionally graded material in the Ti–TiB 2 –B system. *Mater. Sci. Eng. -Struct. Mater. Prop. Microstruct. Process. - MATER SCI ENG -STRUCT MATER* **397**, 92–97 (2005).

22. Reichardt, A. Additive Manufacturing of Metal-based Functionally Graded Materials. (UC Berkeley, 2017).

23. Articek, U., Milfelner, M. & Anzel, I. Synthesis of functionally graded material H13/Cu by LENS technology. *Adv. Prod. Eng. Manag.* **8**, 169–176 (2013).

24. Nemat-Alla, M., Ata, M., Ragab, M. & Khair-Eldeen, W. Powder Metallurgical Fabrication and Microstructural Investigations of Aluminum/Steel Functionally Graded Material. *Mater Sci Appl* **2**, (2011).

25. Bhavar, V., Kattire, P., Thakare, S., patil, S. & Singh, R. A Review on Functionally Gradient Materials (FGMs) and Their Applications. *IOP Conf. Ser. Mater. Sci. Eng.* **229**, 012021 (2017).

26. Bobbio, L. D. *et al.* Characterization of a functionally graded material of Ti-6Al-4V to 304L stainless steel with an intermediate V section. *J. Alloys Compd.* **742**, 1031–1036 (2018).

27. Carroll, B. E. *et al.* Functionally graded material of 304L stainless steel and inconel 625 fabricated by directed energy deposition: Characterization and thermodynamic modeling. *Acta Mater.* **108**, 46–54 (2016).

28. Bobbio, L. D. *et al.* Additive manufacturing of a functionally graded material from Ti-6Al-4V to Invar: Experimental characterization and thermodynamic calculations. *Acta Mater.* **127**, 133–142 (2017).

29. Zhang, Z. *et al.* The peculiarity of the metal-ceramic interface. *Sci. Rep.* **5**, 11460 (2015).

30. Do, T., Kwon, P. & Shin, C. S. Process development toward full-density stainless steel parts with binder jetting printing. *Int. J. Mach. Tools Manuf.* **121**, 50–60 (2017).

31. Fromhold, A. T. J. Theory of metal oxidation. Vol. 2. (1980).

32. Wagner, C. Theoretical Analysis of the Diffusion Processes Determining the Oxidation Rate of Alloys. *J. Electrochem. Soc.* **99**, 369–380 (1952).

33. Cabrera, N. & Mott, N. F. Theory of the oxidation of metals. *Rep. Prog. Phys.* **12**, 163–184 (1949).

CHAPTER 4

PITCH CONTROL OF HEXAGONAL NON-CLOSE-PACKED NANOSPHERE ARRAYS USING ISOTROPIC DEFORMATION OF AN ELASTOMER

4.1 Introduction

Two-dimensional assemblies of colloidal particles have received tremendous interest as facile and inexpensive templates for a wide range of periodically-ordered submicron/nanoscale patterns[1–3]. In its simplest embodiment of so-called colloidal lithography, where colloidal nanospheres are crystalized into a hexagonal-close-packed monolayer on a substrate, an array of truncated tetrahedral nanostructures can be generated upon material evaporation through the interstitial sites between the neighboring colloidal spheres. Such nanostructure arrays, if constructed out of noble metals, exhibit plasmonic properties and optical (i.e., Raman, fluorescent) enhancements and are therefore widely used in sensing[4–7] and optoelectronic applications[8–10]. However, the type of the nanostructures derived from the close-packed array is rather limited, and more complex nanostructure array can be obtained by separating the spheres and carrying out additional processes such as soft lithography, (angled) evaporation, etching, and annealing[2]. Examples of the resulting nanostructures generated from the non-close-packed monolayers include honeycomb patterns[11,12], ordered porous films[13,14], and arrays of nanodiscs[15,16], nanorings[17,18], nano-crescents[19–21], nanocores and nanowires[22–24]. Non-close-packed monolayers significantly increase the versatility of colloidal lithography and the available types of nanostructures over structures derived from a closed-packed monolayer.

A number of methods to fabricate non-closed-packed monolayers using colloidal lithography have been proposed, with an emphasis on control over the interspacing of colloidal nanospheres. They can be categorized into four approaches[3]. First, direct crystallization of

colloidal particles at the oil/water interface can yield ordered non-closed-packed monolayers[2,25]. However, maintaining the ordered arrangements of the particles during the transfer process (from the oil/water interface to a solid surface) is challenging because the position of the particles can be easily disturbed during solvent evaporation. Second, a simple spin-coating technique has been used to fabricate non-closed-packed monolayers[26]. A solution containing monodispersed nanospheres is spin-coated over a flat surface, forming a non-close-packed array embedded in a polymer thin film. Upon removal of the polymer film, large-area, non-close-packed monolayers of colloidal nanospheres can be produced. Due to etching selectivity, colloidal nanospheres need to be inorganic, and thus only silica nanospheres have been utilized. Precise control over the interparticle distance is also difficult to obtain. In a related technique, polymer-grafted nanoparticles were self-assembled to create a 2D non-close-packed array with limited pitch control[27]. The third and fourth approaches convert closed-packed monolayers into non-close-packed architectures and are considered to be the most straightforward and effective because the periodicity of the non-close-packed array is somewhat guaranteed as long as the regularity of the close-packed monolayer can be maintained during the post-processing of taking nanospheres apart. The third approach is to etch highly-ordered close-packed monolayers and reduce the size of the nanospheres using reactive ion etching. The array pitch can be modulated by the initial nanosphere size. Despite its experimental simplicity, the etching approach presents some drawbacks, including the degeneration of the quality of the individual nanospheres (e.g., induced surface roughness and deviation from the spherical shape) and the disruption in array regularity[28,29].

The fourth approach, perhaps the most versatile approach to create non-close-packed monolayers, combines controlled deformation of elastomeric substrates with soft lithographic transfer[30–32]. After the close-packed nanosphere array is transferred onto the elastomer surface, its

initial pitch, which is the same as the diameter of the nanospheres, can be modulated by stretching or swelling of the substrate. Solvent swelling of the elastomer (e.g. polydimethylsiloxane (PDMS)) induces isotropic expansion of the substrate, increasing the array pitch while preserving the original hexagonal order. However, solvents used to swell PDMS are not compatible with the common polymeric nanosphere materials like polystyrene, limiting the choice of colloidal materials. The maximum strain realized by swelling is also constrained to < 50%, requiring multi-step swelling/transfer processes to achieve a large separation between nanospheres[30,31]. Mechanical deformation of the elastomer substrate via stretching offers better control of the lattice spacing and arrangements, but so far, is limited to uniaxial or biaxial stretching. Since the self-assembled 2D colloidal array is composed of numerous crystalline domains, with each domain possessing the hexagonal arrangement but pointing at random orientation, anisotropic deformation of uniaxial and biaxial stretching results in a non-close-packed array with broken hexagonal symmetry and non-uniform lattice structures. Therefore, fabrication of well-separated, non-close-packed monolayers with the original hexagonal arrangement is still difficult to realize[29], and a simpler approach is highly desirable to increase the flexibility of colloidal lithography and the type of accessible nanostructures.

In this chapter, we present a facile and robust method to create a highly-ordered, well-separated non-close-packed monolayer of colloidal nanospheres using soft-lithographic lift-up and transfer-printing techniques combined with radial stretching of an elastomer. A custom-made radial stretching stage enables the elastomer substrate to expand isotropically and allows the pitch of the non-close-packed nanosphere array to be accurately controlled, while preserving the original hexagonal arrangement. The non-close-packed nanosphere array picked up by the elastomer stamp can be transferred onto a variety of target substrates. Unlike the solvent-swelling approach, this

stretch-and-transfer (SAT) process is compatible with any colloidal material, and a pitch increase as large as 213% (490 nm original pitch increasing to 1532 nm) can be achieved in a single stretch-and-transfer step with accurate pitch control. Similar pitch control would require at least three cycles of the swelling-and-transfer process. The maximum pitch achievable in the single SAT process depends on the compliance/stretchablilty of an elastomer like PDMS, and its implication on the spatial uniformity and the nonlinear stretching behaviors will be discussed. In particular, the effect of the stretching direction on the resulting lattice structure will be investigated for uniaxial, biaxial, and radial stretching scenarios. These nanosphere arrays transferred onto the various receiving substrates (e.g., Si, quartz, plastics) modify the optical response of the substrate and serve as an etch mask or a mold for the subsequent generation of the nanostructures.

4.2 Experimental Details

Preparation of Nanosphere Arrays: The substrate preparation was similar to a previous report[29]. Briefly, a 22 mm square coverglass was ultrasonically cleaned in acetone and isopropyl alcohol for 5 min each. The coverglass was further cleaned in a piranha solution (H_2SO_4: H_2O_2 = 3:1) for 30 min and subsequently in a standard cleaning solution (H_2O_2: NH_4OH: deionized water= 1:1:5) for 30 min to render its surface hydrophilic. The coverglass was then thoroughly rinsed with DI water and stored in DI water until used. Polystyrene nanospheres with a nominal diameter of 490 nm were purchased from Polysciences Inc. and mixed with a 400:1 solution of methanol: Triton X-100 as 3:1 (3 parts of polystyrene nanosphere stock solution, 1 part of a mixture of methanol and Triton X-100). In order to form a hexagonally close-packed monolayer, the nanosphere solution was spin-coated onto each coupon at 400, 500, and 1400 rpm (for 30s, 2 min, and 10s, respectively). The nanosphere-coated substrates were then dried overnight.

Stretching and Transfer process: The NSs were etched in an RIE (Nordson March RIE-1701) to reduce the nanosphere size and separate them. The parameters for the RIE plasma were 10 sccm of pure O_2, 100 mTorr of a process pressure, and 30 W of the RIE power. Unless noted otherwise, the etching time was controlled to reduce the NS diameter to 250 ~ 280 nm. A 20-nm-thick Al layer was evaporated on top of the NS arrays in an Edwards Auto 306 Evaporator (background pressure about 8×10^{-7} Torr). Polydimethylsiloxane (PDMS) with different ratios of 10-to-1 to 50-to-1 (the weight ratio of the PDMS prepolymer to the curing agent) was mixed and molded to create a sheet of 2 mm thickness. It was cured for three hours at 60°C. A circle with a diameter of 30 mm was cut out from the PDMS sheet using a punch. This piece served as a PDMS stamp and was used to pick up the nanosphere array from the initially-deposited substrate. This was accomplished by pressing down the PDMS stamp on top of the array at 60°C and peeling it away from the substrate at a fast (> 10 cm/s) speed in order to ensure that most of the nanospheres were picked up. The PDMS stamp with the Al-coated nanosphere array was then placed in a home-made radial stretcher and stretched with a maximum strain of approximately 500%. Prior to the transfer, a target substrate was coated with a thin layer (< 100 nm) of the SU-8 adhesive (Microchem, SU-8 2100 diluted with a SU-8 thinner solution). The stretched PDMS was brought into contact with the adhesive-coated substrate at 95°C. Uniform pressure was applied until the SU-8 was cured by the heat. The PDMS was slowly peeled away from the target substrate, and the non-close-packed array was transferred to the new substrate.

Imaging and Analysis: SEM images were obtained using a Hitachi S-4700 II FESEM/Edax Phoenix EDS instrument. Image analysis was performed using ImageJ software. Transmission optical measurements were acquired using a Craic Microspectra 121 microscope with a 10x objective.

Nanoimprinting process: Once the PS nanospheres with an Al layer were transferred onto the SU-8-coated Si substrate from the stretched (~ 100%) PDMS membrane, RIE (Nordson March RIE-1701) was used to etch the SU-8 layer with the Al-coated nanospheres acting as an etch mask. The parameters for the RIE plasma were 10 sccm of pure O_2, 100 mTorr of a process pressure, and 30 W of an RIE power. After removing the SU-8 layer, another RIE recipe was used to etch the Si substrate to obtain the Si mold. The parameters for this recipe were 16 sccm of CF_4, 4 sccm of Ar, 50 mTorr of a process pressure, and 130 W of an RIE power. To promote the mold release after the nanoimprinting step, the Si mold surface was treated with Repel Silane (GE Healthcare Life Sciences Inc.). An adhesion promoter (ZAP-1020, Chemoptics Inc.) was applied onto the PET film. A few droplets of the UV polymer (ZPUA, Gelest Inc.) were placed on the surface of the Si mold, and a PET film was pressed on top of it. The PET-film/Si-mold stack was put under the UV light (400 W, 365 nm), and the UV polymer was cured through the transparent PET film. After a desired time lapsed for curing the UV polymer, the PET film was peeled off from the Si mold, and the inverse patterned (nanohole array pattern) was imprinted onto the UV polymer on the PET film. With the same nanoimprinting step repeated, the pattern of the original nanopillar array was transferred onto the receiving Si substrate.

4.3 Results and Discussion

Figure 4.1 outlines the procedure of the proposed SAT process to generate a non-close-packed hexagonal PS nanosphere array with a tunable pitch on various substrates. Briefly, a PS nanosphere solution is spin-coated on top of a cleaned, rigid substrate (e.g. cover glass or silicon) to obtain a hexagonally-ordered close-packed nanosphere array assembled by the intricate balance between centrifugal and evaporation-induced capillary forces[33,34]. Subsequently, Reactive Ion Etching (RIE) reduces the diameter of the prepared nanospheres by a small amount (< 35%) to

maintain the hexagonally-ordered arrangement and smoothness of the nanosphere surface. Extensive etching of PS nanospheres typically introduces undesirable features including the rough surfaces and shape irregularities[28,29]. Aluminum or silver is then evaporated on top of the reduced nanospheres. In the next stage, metal-coated nanospheres are transferred onto the surface of a PDMS elastomer sheet. This thin (~ 2 mm) PDMS stamp is highly compliant and thus can be brought into intimate contact with the nanospheres without applying significant pressure. Prior to detachment, heat (~ 60°C) is applied to the stack to improve the adhesion between the PDMS and nanospheres. Note that due to the kinetically adjustable adhesion of PDMS[35,36], a faster peeling speed is likely to pick up more nanospheres and improve the yield. The PDMS stamp with the transferred nanospheres is then placed onto a home-made stretcher device which can fix and stretch the PDMS stamp radially. This radial stretching process allows the PDMS membrane to be stretched equally in all in-plane directions, further separating the nanospheres while retaining their original hexagonal order. The maximum pitch of the nanosphere array depends on the compliance of the PDMS stamp, which can be controlled by a mixture ratio of the resin and its curing agent.

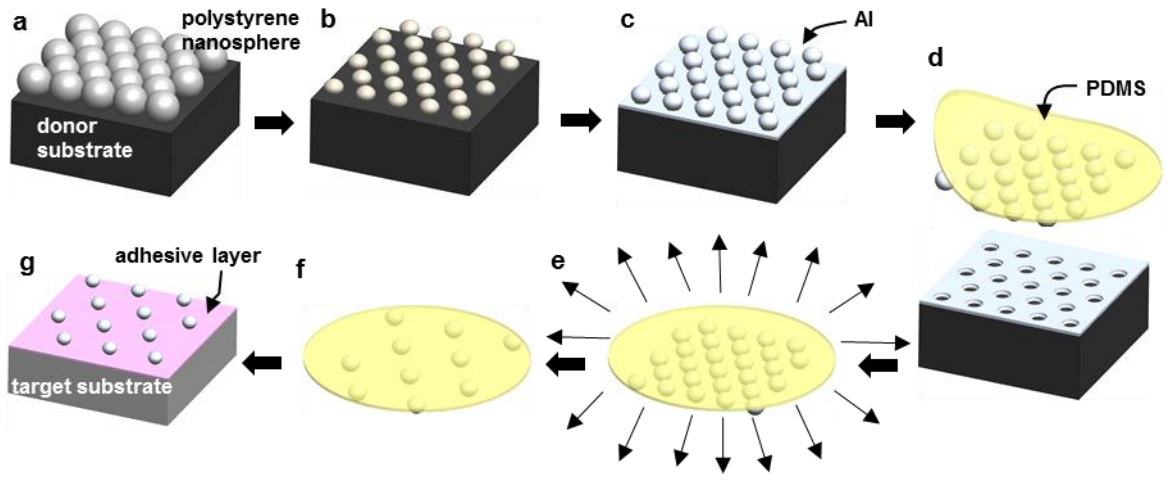

Figure 4.1 Schematic diagram of the PDMS-based stretching and transfer process used to fabricate variable pitch nanostructures with hexagonal order and constant diameter (ball: nanosphere, yellow: PDMS, white: aluminum layer, pink: adhesive layer)

After the PDMS stamp is stretched to a desired level, the array of the Al-coated nanospheres on the PDMS stamp is transferred into a target substrate coated with a thin adhesive layer. The adhesive layer provides stronger bonding to the nanospheres compared to PDMS, facilitating the 2nd transfer process. After the 2nd transfer, the Al-coated side of the nanospheres faces upward on the receiving substrate and can serve as an etch mask. A portion of the adhesive layer not covered by the nanosphere array can be etched in RIE to expose the underlying substrate. The metal films on the nanospheres are much sturdier as an etch mask than the polystyrene nanospheres, and therefore, a wider class of substrates can be etched in RIE. One critical point is that the thickness of the adhesive layer should be comparable to or smaller than the size of the nanospheres to ease the removal of the adhesive layer when necessary. In our study, a thin SU-8 layer (50~100 nm) was spin-coated onto the target substrate prior to the nanosphere transfer, significantly improving the transfer yield. The target substrate was heated to 95°C, which is the curing temperature of SU-8. Since the glass transition temperature of polystyrene is around 100°C, the PS nanospheres were not deformed during the transfer and retained their shape. From the SAT process, the nanospheres can be transferred from the originally-assembled substrate to any target substrate, while the array pitch can be modulated without disturbing the hexagonal order of the array. In the end, we can obtain patterned nanostructures with the nanospheres acting as a mask or mold in various substrate materials, such as silicon, glass, quartz, plastics, etc.

4.3.1 Array pitch control

Unlike the linear stretching stage that most research groups have employed, our custom-made stretcher (Figure 4.2a) was designed to radially stretch a thin elastomeric membrane up to 500% to preserve the hexagonal symmetry of the original nanosphere array. Figure 4.2b-4.2f

shows the radial stretcher in action: the PDMS membrane with an array of the Al-coated nanospheres was stretched at different nominal strains of 0%, 50%, 70%, 100%, and 200%, respectively. Here the strain ε is defined as $(D - D_0)/D_0$, where D_0 is the diameter of the suspended PDMS membrane in the unstretched state and D is the diameter after stretching. Dimmer color was observed for the nanosphere region in case of the larger strain and can be attributed to the larger separation between the nanospheres. After transferring the stretched nanosphere array in Fig. 4.2f (ε = 200%) onto a Si wafer (Fig. 4.2g), rainbow colors can be clearly observed due to a grating effect[37]. This vivid color also indicates that the hexagonal order arrangement of nanospheres has been well preserved during the double-transfer process.

Since the PDMS stamp is used to change the pitch of nanospheres, the extent to which the pitch can be controlled is related to the maximum strain achievable by PDMS. The amount by which PDMS can be stretched before failure depends on a mixture ratio of the PDMS prepolymer and curing agent as well as the stretching direction. Uniaxial stretching typically allows PDMS to be stretched more than biaxial or radial stretching. When the PDMS membrane is stretched uniaxially, it shrinks in the other two directions (width-wise and thickness-wise), which allows the stamp to be stretched further. But when it is stretched biaxially or radially, the expansion takes place in two dimensions (in-plane) and all the deformations need to be accommodated by thinning of the membrane, causing the membrane to fail at a lower strain. Over 125% stretching was reported for 10:1 PDMS (10 parts of prepolymer and 1 part of curing agent) when uniaxially stretched[38], but from our experiments, the PDMS membrane with the same mixture ratio failed around 89% of radial stretching.

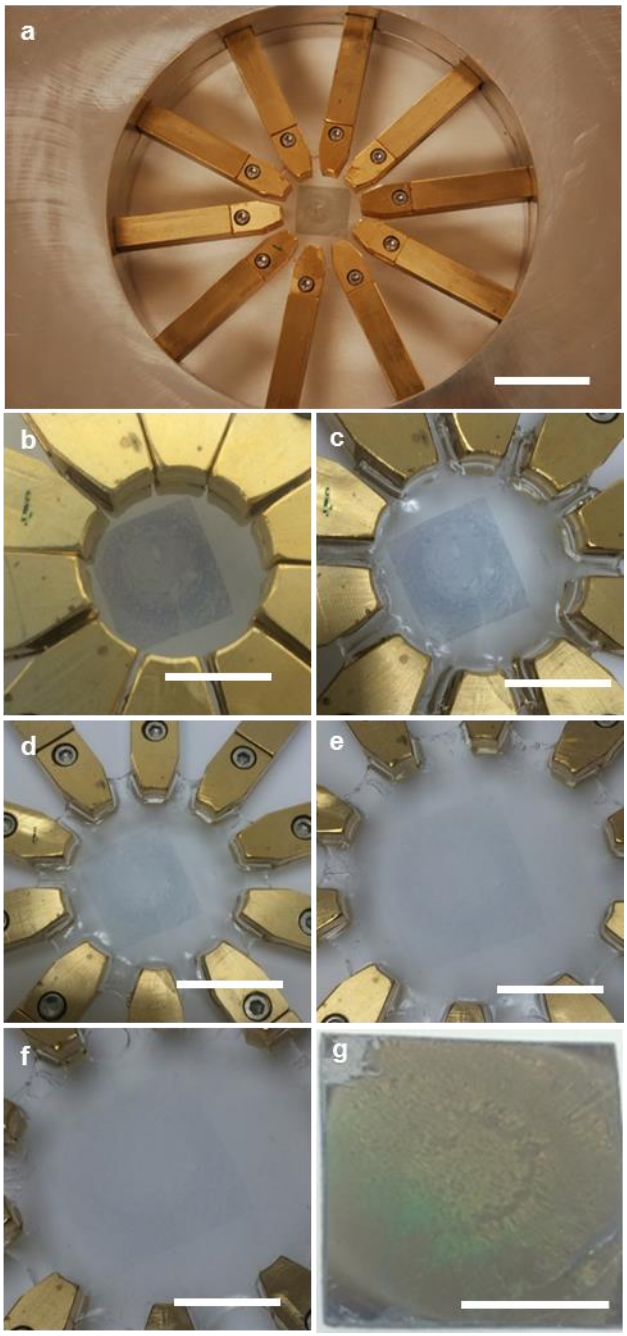

Figure 4.2 Camera images of (a) a radial stretching device on which a PDMS stamp with the Al-coated PS nanosphere array is mounted (the gray square pattern in the suspended PDMS sheet indicates the nanosphere array region); (b-f) the PDMS stretched at different strains at b. 0%, c. 30%, d. 70%, e. 100%, and f. 200%. (g) the 200% stretched sample of the nanosphere array transferred to the Si wafer. (Scale bar: a: 20 mm; b-c: 10 mm; d-f: 15 mm; g: 5 mm)

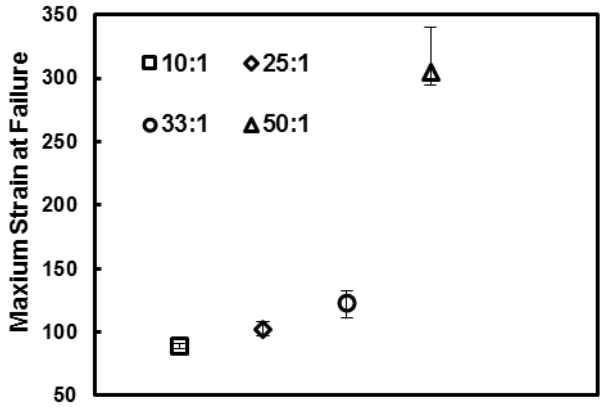

Figure 4.3 The maximum strain at failure (rupture) is plotted for various weight ratios of the PDMS prepolymer and curing agent. The strain is applied using a radial stretching apparatus, and the maximum strain by radial stretching is substantially smaller than that of the uniaxial stretching case.

More importantly, the maximum strain at which PDMS can tolerate without failing depends on the weight ratio of the prepolymer and curing agent[39,40]. In general, PDMS with a lower prepolymer-to-curing-agent ratio is more compliant, leading to a larger strain at failure. The maximum strain at which PDMS fails under radial stretching has not been reported; therefore, we carried out radial stretching test for several mixture ratios of PDMS and recorded the maximum strain for each condition (see Figure 4.3). The mixture ratio of 10:1, 25:1, 33:1, and 50:1 resulted in an average maximum failure strain of 89%, 102%, 123%, 305%, respectively. It was previously found that PDMS with less curing agent leaves a large portion of the prepolymer unreacted and less cross-linked, making it softer[41]. From our results, we conclude that the nanosphere array pitch can be extended by about three-fold (with a 50:1 mixture of PDMS) from the single SAT process. Further reduction in the amount of curing agent in the mixture may allow PDMS to be radially stretched more than 300% but would not work here due to the difficulty in transfer printing. Excessive unreacted prepolymer from the low prepolymer-to-curing-agent-ratio PDMS weakens

it mechanically and makes its surface extremely tacky. Therefore, after transferring the nanospheres to the target substrate, it is very difficult to peel off the PDMS membrane from the substrate without ripping its edge. Figure 4.4 shows that the PDMS residue remained on the surface of the target substrate after stretching and transferring with the 50:1 PDMS membrane. This limits the maximum pitch achieved by the single SAT process. In this work, we used a 33:1 PDMS membrane for the SAT process of up to 100% strain and the 50:1 PDMS membrane for over 100% strain.

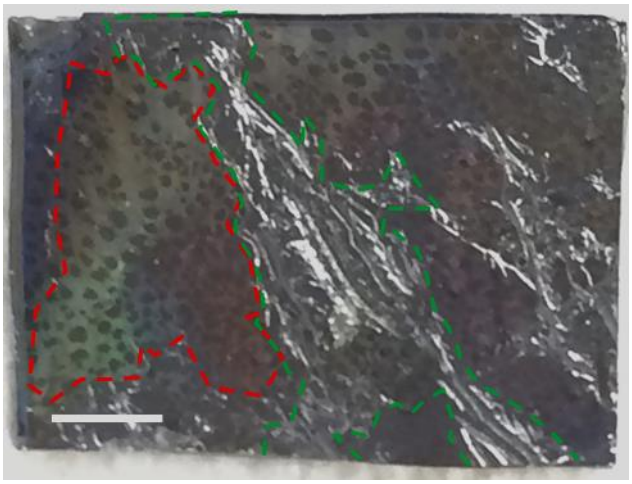

Figure 4.4 Camera image of the transferred nanosphere array from the 50:1 PDMS membrane onto the Si substrate. The green region shows the PDMS residue left after transfer printing of the nanosphere array. The red bounded region is the residue-free region showing the transferred nanosphere array. This result suggests that the 50:1 PDMS membrane or membranes with a lower prepolymer-to-curing-agent ratio is unstable and too sticky, making it extremely difficult to be peeled off after being brought into contact with the receiving substrate (Scale bar = 4 mm).

Figure 4.5 depicts the SEM images of the Al-coated nanospheres transferred onto the Si substrate with 8 different strains from 0% to 300%. Prior to the SAT process, all samples were identically etched in RIE and coated with Al, resulting in nanospheres with an average diameter of 342 nm arranged in a hexagonal lattice structure (see Figure 4.5a for the unstretched sample,

i.e., 0%). Nanospheres were etched in RIE to facilitate the initial pick-up process as the etched nanospheres exhibited a better adhesion to the PDMS membrane[22]. We also found that the etched nanospheres tend to move individually and independently during the stretching process, allowing the array to better preserve its regularity. The yield of the SAT process was estimated by counting the number of missing vs. transferred nanospheres in the array on the receiving substrate. The nanospheres that were successfully transferred but severely displaced from the hexagonal arrangement were treated as missing ones. Analysis of the multiple SEM images indicates that the process yield is greater than 95% regardless of the applied strains, helping to conserve most of the nanospheres for future use (Figure 4.6).

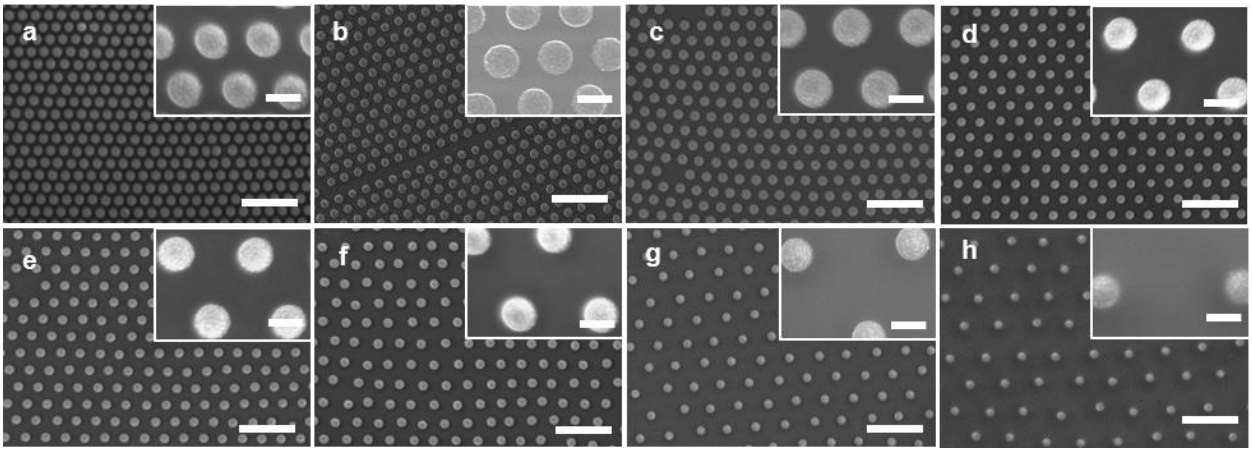

Figure 4.5 SEM images of the non-close-packed nanosphere array after transfer onto Si substrates with strains of: a. 0%, b. 25%, c. 30%, d. 50%, e. 70%, f. 100%, g. 200%, h. 300%. Inset: high magnified views of each image (Scale bar: 2 μm and 300 nm

The pitch of the original array is the same as the diameter of the unetched nanospheres, estimated at 490 nm. The SEM images in Fig. 4.5 show that the hexagonal arrangement of the original nanospheres was well preserved, even for the sample with 300% strain, and the distance between the adjacent nanospheres was proportional to the strains. The lattice spacing of the crystal

structures increased from 608 nm to 1364 nm as the strain increased from 30% to 300%. Although the hexagonal symmetry of the array was preserved, the pitch uniformity as a function of the applied strain was also of interest. It can be speculated that a larger strain may disturb the array

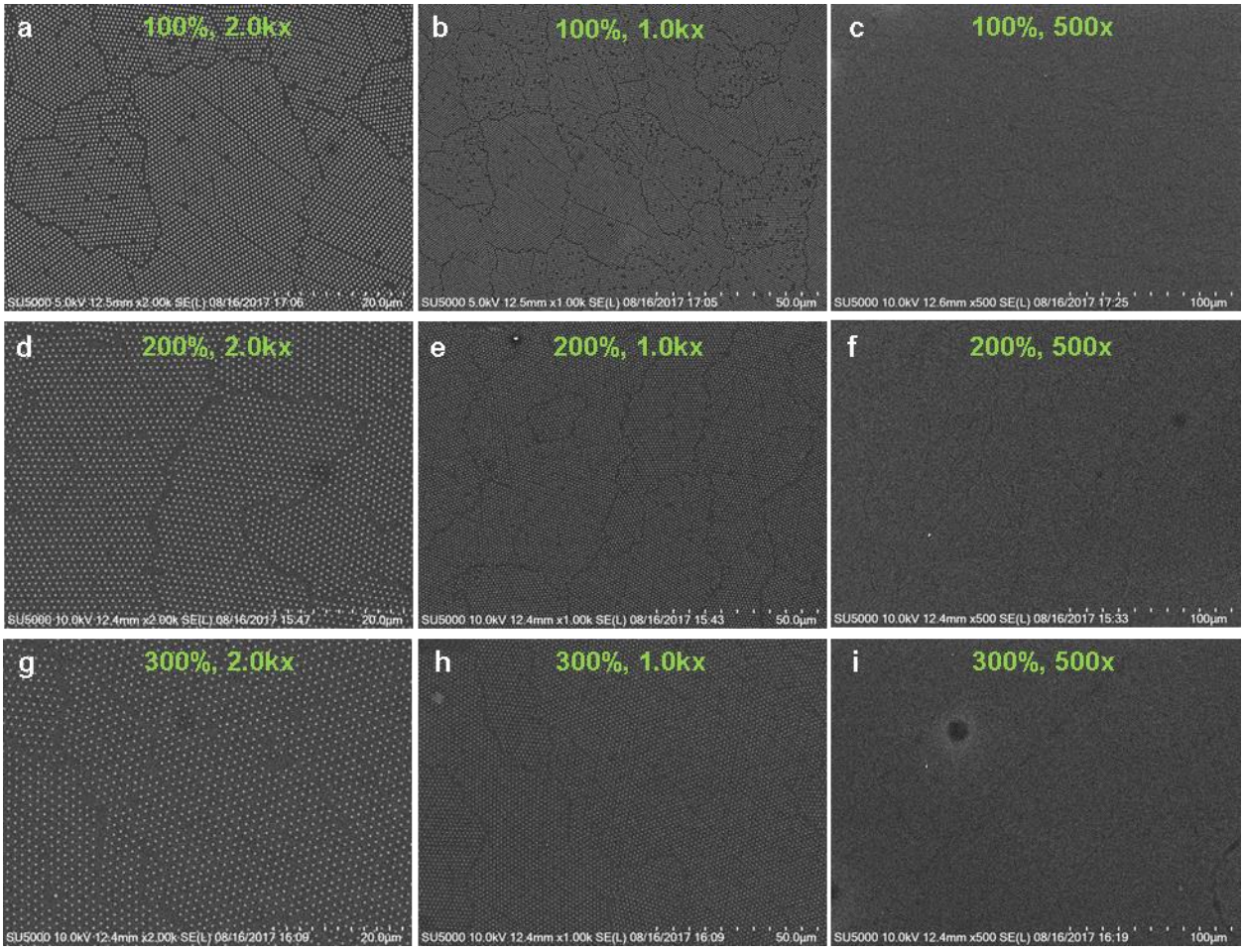

Figure 4.6 Low-magnification (500x, 1000x, 2000x) SEM images of three different SAT samples (100, 200, 300% strains) showing that the SAT process can work over a large area with a process yield of more than 99%.

lattice more due to the increased relative motion of nanospheres on the PDMS surface during stretching and an uncertainty associated with the transfer printing of the nanospheres from the more heavily stretched membranes. The disturbance of the array lattice was quantified by

measuring the center-to-center distance between two neighboring nanostructures in the SEM images[29].

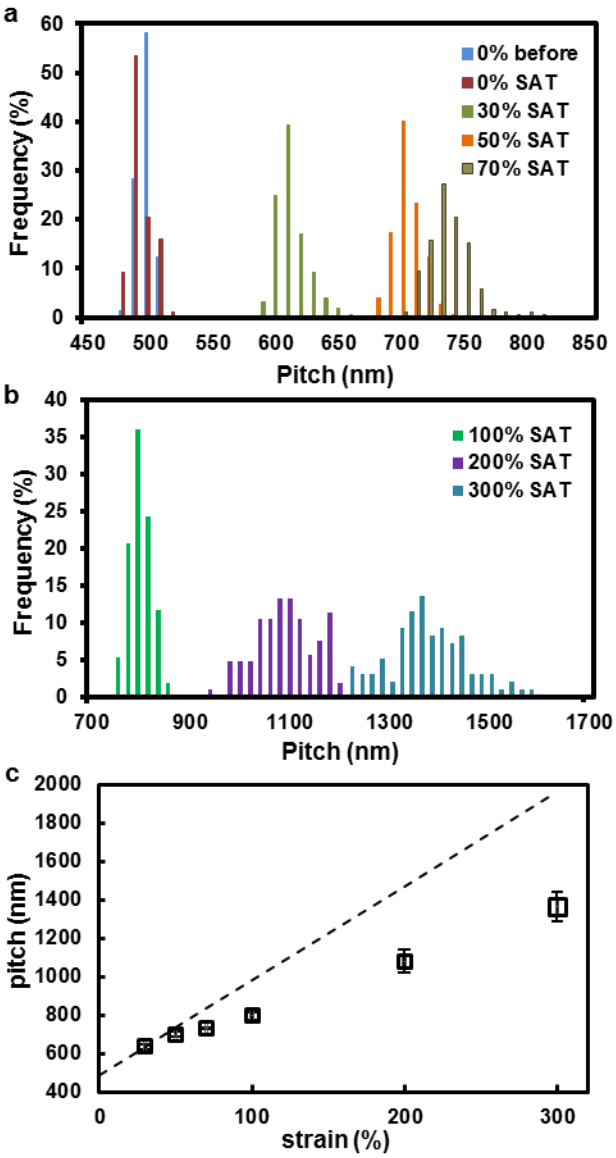

Figure 4.7 a) Pitch distributions measured from 150 nanospheres at different strains (light green for 30%, orange for 50%, and brown for 70%) and non-stretched array before and after transfer (blue for the original assembly and violet for the original assembly transferred without stretching). b) Pitch distributions measured from 80 nanospheres at larger strains (green for 100%, purple for 200%, and navy for 300%). c) Plot of the measured pitch as a function of actual strain. The dotted line is the nominal pitch calculated from the applied strain.

The histograms of the array pitch distribution for different strains are shown in Figure 4.7a and 4.7b. Note that a nanosphere array prepared by colloidal lithography typically exhibits intrinsic point and line defects. In order to minimize the effect of the defects on the pitch measurement, we selected from each sample the defect-free domains whose sizes are in the range of 10 μm^2. See the Figure 4.8 for more detailed description on the pitch measurement. "0% before transfer" means the nanosphere array in the originally-assembled substrate before it was transferred to the PDMS membrane. "0% SAT" indicates the nanosphere array transferred to the Si substrate without being the same (493 nm for blue and 490 nm for violet) but the "0% SAT" sample exhibits more spread (standard deviation = 5 nm for blue and 9 nm for violet) in the distribution, suggesting that the transfer printing process introduces a small degree of disturbance in the array. The histograms of the pitch in Figure 4.7a-b indicate that the average pitch and standard deviation of the stretched nanosphere arrays at 30%, 50%, 70%, 100%, 200% and 300% are 608 nm (13 nm), 699 nm (14 nm), 731 nm (18 nm), 794 nm (22 nm), 1080 nm (60 nm), and 1364 nm (79 nm), respectively.

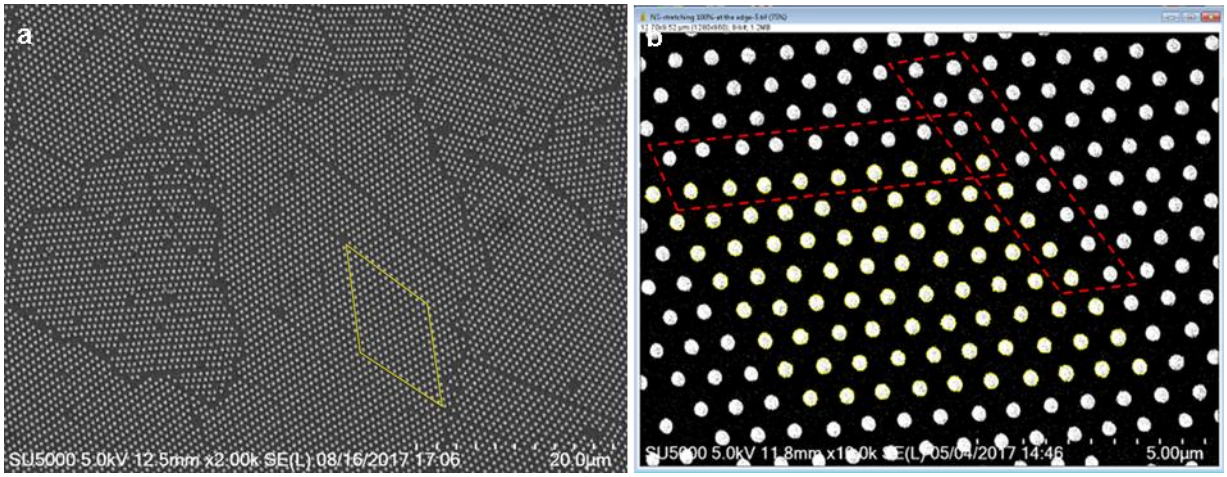

Figure 4.8 (a) SEM image of the 100% SAT sample. The yellow-boxed region represents the defect-free crystalline domain, (b) the black-and-white converted image with the proper threshold delineating the boundary of the nanospheres (Image-J). The red boxed regions are excluded for the analysis because of the apparent line defects from the initial assembly stage.

stretched. Comparison of these two histograms (blue and violet in Figure 4.7a) reveals the effect of the transfer printing processes on the array lattice. The mean values of the pitches are essentially

The average pitches and standard errors of all the samples at different strains are shown as a single plot in Figure 4.7c. The breath of the standard errors indicates the degree of array disturbance, which increases with larger strain. This is expected because the action of stretching will bring out more uncertainty in the transfer printing process. The straight dotted line is the nominal pitch calculated from the applied strain. The discrepancy between the nominal and actual pitch is rather small for the strain from 0 to 100%, indicating that the PDMS membrane was stretched in accordance with the strain imposed by the radial stretcher. However, a significant increase in deviation from the actual pitch is observed for larger applied strains. For example, the nominal pitches of 30% and 200% stretched samples are 637 nm and 1470 nm, respectively, and the averaged actual pitches obtained via SAT were 607 nm and 1080 nm, respectively. Therefore, the percent ratio of the actual pitch over the nominal pitch is 95.3% for the 30% sample, but 73.5% for the 200% sample. One hypothesis for this mismatch between the applied strain and actual pitch is that the PDMS membrane deformation is spatially non-uniform. It may be that the edge of the membrane stretches more than the center region because the membrane is gripped by the radial stretcher. The closer the gripping points (i.e., by the edge), the larger the stress applied to the membrane (i.e., the edge region of the membrane getting stretched more than the center region).

To test this hypothesis, we investigated the spatial uniformity by imaging the nanospheres near the center vs. edge of the nanosphere patterns after the SAT process. Note that all the images and pitch measurements shown in Figure 4.5 and 4.7 were obtained from the center region of the nanosphere pattern on the PDMS membrane. In Figures 4.9a, b and c, we compare the pitch distribution of the nanospheres near the center to those near the edge of the samples stretched

100%, 200% and 300%, respectively. In the case of the 100% stretched sample, the difference in the array pitch between the center and edge regions is small, i.e., 794 nm ± 21 nm for the center and 814 nm ± 68 nm for the edge. On the other hand, the 300% stretched sample exhibits a significant increase in the pitch from the center (1364 nm ± 79 nm) to the edge (1533 nm ± 127 nm). To better summarize the overall trend of the mismatch between the applied strain and actual pitch for both center and edge region, we plot the ratio of the actual to nominal pitch (denoted as a pitch ratio) over the entire range of the applied strains (see Figure 4.9d). This pitch ratio quantifies how much a portion of the PDMS membrane was stretched relative to the applied strain. Regardless of the applied strain, the edge region of the nanosphere pattern always shows a larger pitch ratio, meaning less stretching in the membrane center and more stretching away from it. The discrepancy in the pitch ratio between the center and edge regions grows larger for larger applied strain. In addition, the nanosphere array near the pattern edge always exhibits a broader pitch distribution, which is accentuated with larger strain. This reflects how the radial stretcher pulls the membrane apart. As can be seen from Figure 4.2, 10 fingers are equally distributed around the membrane to stretch it radially. At large strains, the membrane between the two adjacent gripping points tends to retract inward, creating a non-uniform strain field in the membrane near the fingers, and increasing the variability in the array pitch.

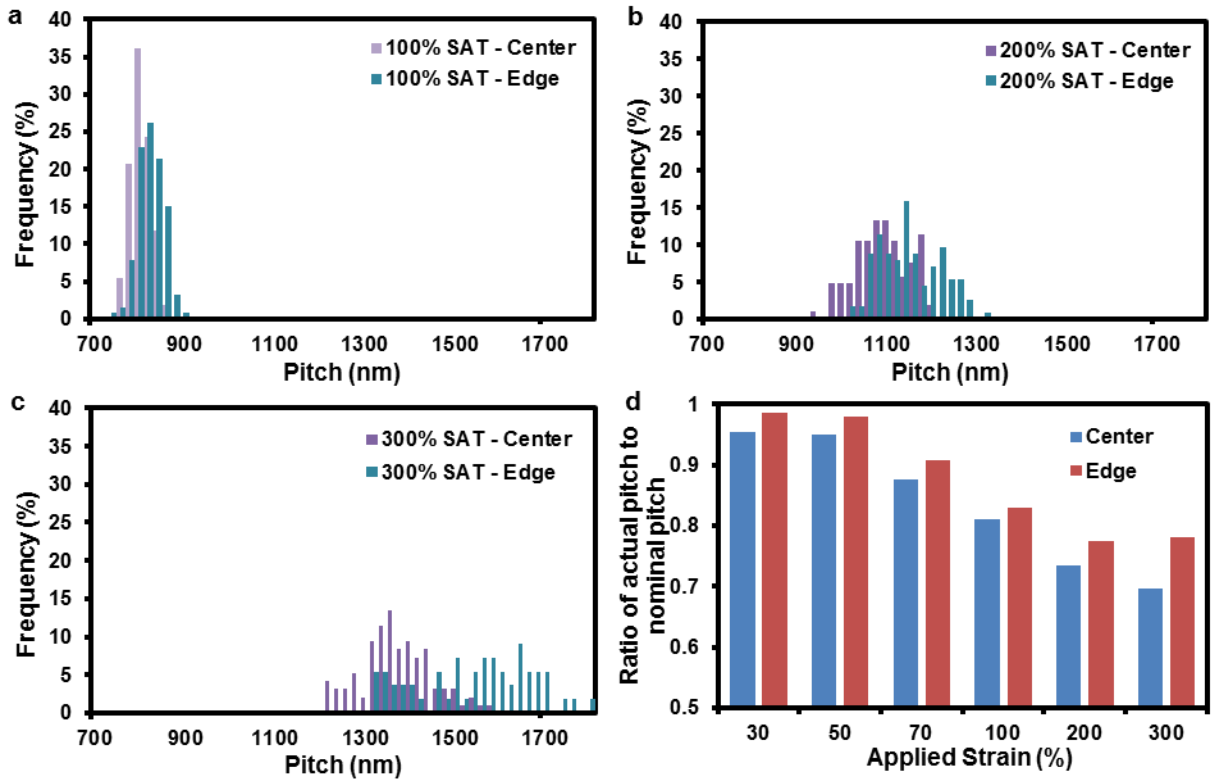

Figure 4.9 Pitch distributions measured from 80 nanospheres in the center and near the edge of the PDMS membrane for the various applied strains of a) 100%, b) 200%, and c) 300%; d) a ratio of the actual pitch to nominal pitch in the center and at the edge as a function of different strains from 30% to 300%.

Interestingly, the actual pitch near the edge of the nanosphere pattern is still smaller than the nominal pitch calculated from the applied strain. Note that the overall size of the nanosphere pattern is around 1 cm by 1 cm (see Figure 4.2g) while the freestanding portion of the PDMS membrane in the stretcher apparatus is 1.7 cm in diameter. When the pattern is transferred to the center of the PDMS membrane, the pattern edge is a few millimeter from the membrane edge. Therefore, we speculate that the PDMS membrane is stretched more near its edge, accounting for the remaining discrepancy in pitch. Because the edge portion gets stretched more extensively, the

membrane thins near the gripping points and can be easily ripped at large applied strains (see Figure 4.10).

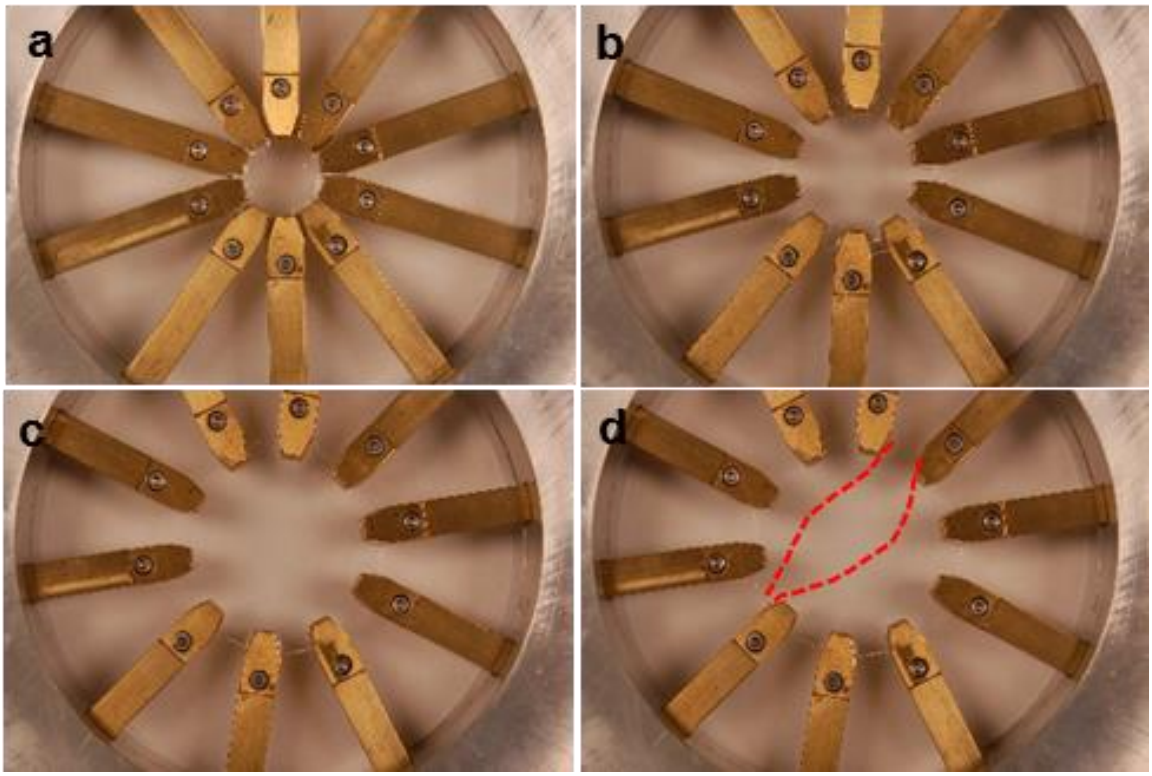

Figure 4.10 (a-d) Camera images showing the stretching process until membrane failure. From d, the membrane ripping first happens at the edge (between the adjacent gripping points). The red dash line in d) shows the ripped line.

4.3.2 Control of array structure

One advantage of creating a non-close-packed array via mechanical deformation of a soft substrate is the ability to modulate the nanosphere array pitch with high precision as well as to create various lattice structures. Previous studies reporting the SAT approach[30,31] employed uniaxial stretching of the stamp substrate, which can alter the lattice structure of the non-close-packed array due to anisotropic deformation. An interesting aspect of uniaxial stretching is that the resulting lattice structure depends on the stretching direction with respect to the array configuration

(see Figure 4.11 and 4.12 for the SEM images and schematic illustration). For example, an as-prepared 2D nanosphere array is made up of numerous crystal domains of hexagonal-close-packed arrays with random orientations. Therefore, uniaxial stretching causes each of the crystal domains to be stretched differently because their lattice structures are aligned differently with respect to the stretching direction. The SEM image in Figure 4.13a shows multiple crystal domains of the SAT sample made by uniaxial stretching of 100% nominal strain. The lattice structure of each domain differs from one another due to the anisotropic deformation. The Fast Fourier Transform (FFT) of each domain exhibits the crystalline lattice (see Figure 4.11A), but when these different domains are combined for FFT, a distorted lattice structure is clearly seen (see the inset of Figure 4.13a). Biaxial stretching also induces anisotropic deformation and leads to the various Bravais lattice structures as shown in Figure 5b and Figure 4.11B. In the same work[30,31], two-step uniaxial stretching was also utilized instead of biaxial stretching with the pre-stretched array being transferred to another PDMS substrate and stretched at a direction different from the initial stretching direction. Lattice structures such as rectangular, square, and oblique arrays can be produced from the as-prepared hexagonal nanosphere arrays. Since the SAT method based on uniaxial/biaxial deformation unavoidably breaks the hexagonal symmetry, maintaining the original hexagonal lattice structure across all the randomly-oriented crystal domains, requires that the stamp be stretched in an isotropic manner, necessitating radial stretching. Indeed, regardless of the initial orientation of the crystal domains, the radially-stretched sample preserves the hexagonal lattice structure of all the arrays on the substrate (see Figure 4.13c and Figure 4.11C).

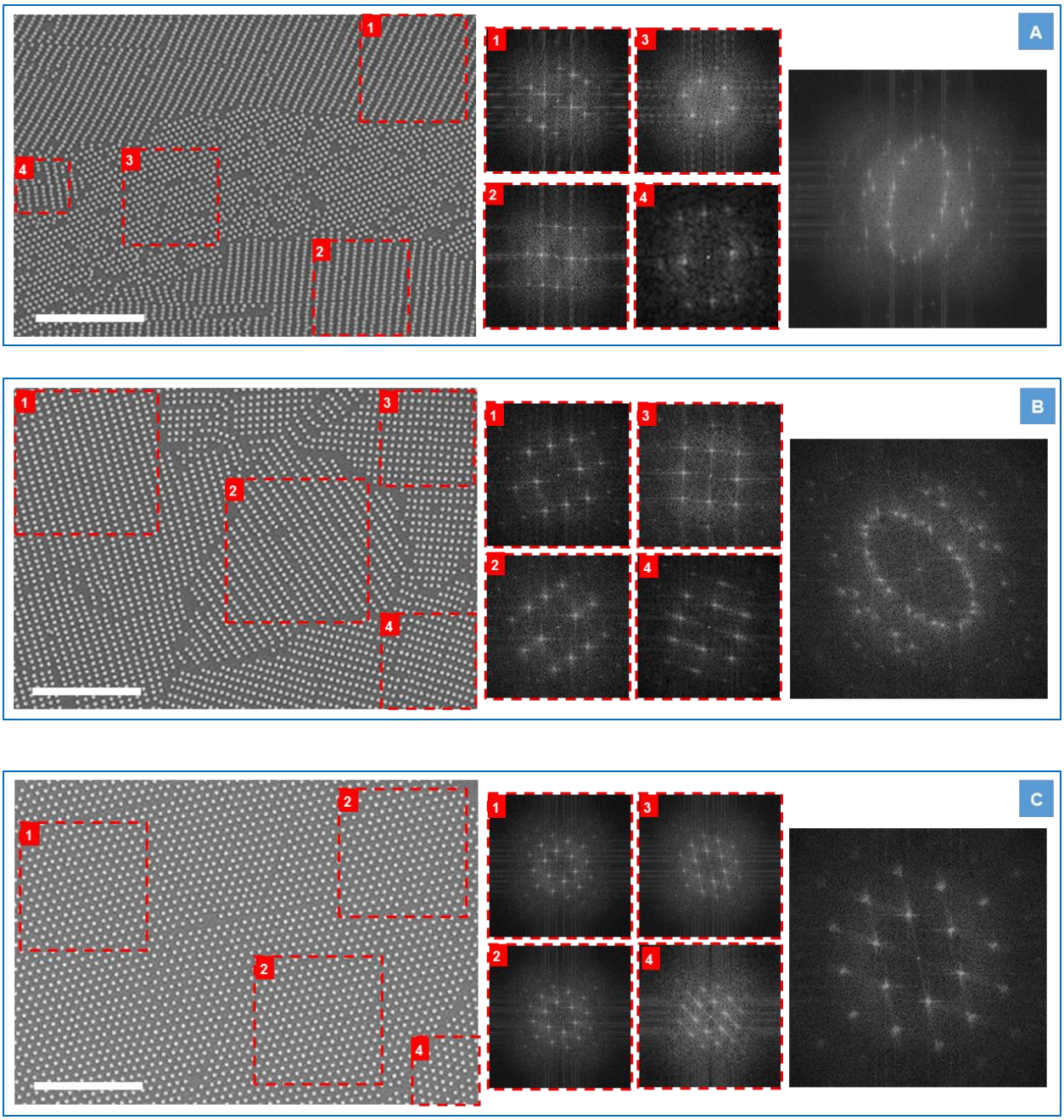

Figure 4.11 SEM images and Fast Fourier Transform (FFT) data for the PS nanosphere arrays stretched and transferred to the Si substrates with (A) uniaxial, (B) biaxial, and (C) radial stretching of 100%, respectively. The FFT technique is used to study the periodicity of micro- and nanostructure arrays and observe the lattice spacing and structure of the arrays. The FFT data was collected from multiple crystalline domains (1~4) and from the entire image (far right).

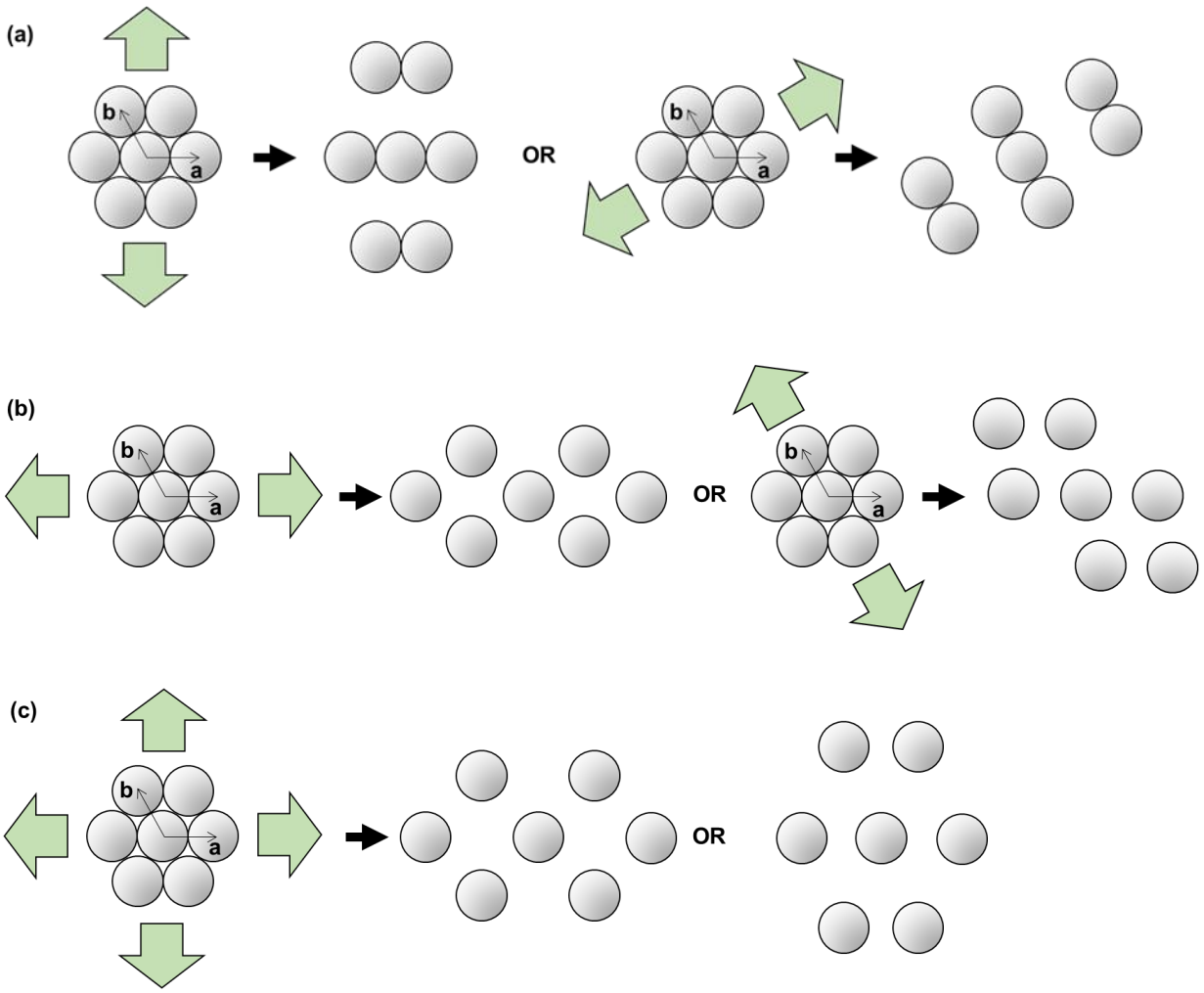

Figure 4.12 Schematic of the stretching direction with respect to the original hexagonal array in case of (a-b) uniaxial and (c) biaxial stretching.

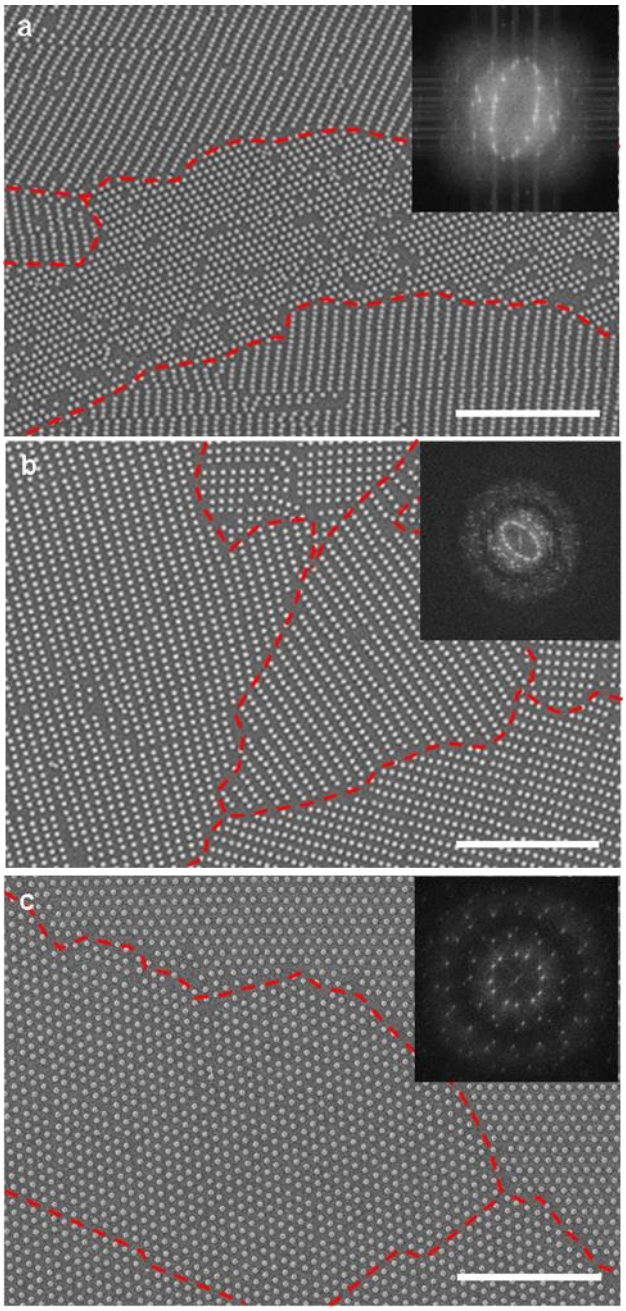

Figure 4.13 SEM images of the nanosphere array with stretching in three different directions and FFT data: a. uniaxial stretching 100%; b. biaxial stretching 100%, and c. radial stretching 100%, Insert: FFT figures for each SEM image.

4.3.3 Transfer the Array to Various Surfaces and Applications

Strong hydrophilicity of the substrates is important when directly assembling nanospheres suspended in an aqueous solution into a 2D array[42]. Therefore, substrates with insufficient hydrophilic surfaces must be functionalized or otherwise treated to improve their wettability for a high-quality 2D assembly. Here, we employ the SAT technique to transfer highly-ordered hexagonal arrays onto the surface of any target material, such as glass, quartz, and flexible substrate. A thin adhesive layer (e.g., 60 ~ 100 nm-thick SU-8 layer) was spin-coated on the surface of the target substrate to improve the adhesion with the nanospheres. Figure 4.14 shows Al-coated nanosphere arrays transferred onto a Si coupon (Fig. 4.14a), a quartz disc (Fig. 4.14b), and a plastic film (polyethylene terephthalate, PET) (Fig. 4.14c). Prior to the transfer to the target substrates, the nanosphere arrays were etched and coated with Al (resulting in an average diameter of 342 nm), transferred onto the PDMS stamp and stretched by 100%. The color observed on each surface indicates the regularity of the nanosphere array preserved during the SAT process. Three SAT samples of the Al-coated nanosphere arrays on the quartz discs were studied for their optical characteristics. As shown in Fig. 4.14d, the transmission spectra were measured for each sample (0%, 50%, and 100% SAT on the quartz substrates). The transmission measurement from a blank quartz disc was used to normalize the data. The transmission spectrum of the 0% stretched sample has a broad dip related to the strong reflection and/or absorption of the Al-coated nanosphere pattern that is centered around 1050 nm. This spectral feature shifts to about 1280 nm for the 50% stretched sample. Thus there is an apparent dependence of a dip position as a function of pitch. The overall transmission increases with the stretch percentage because the more the array is stretched, the less dense the array, and the more transparent the substrate (see Fig. 4.14d).

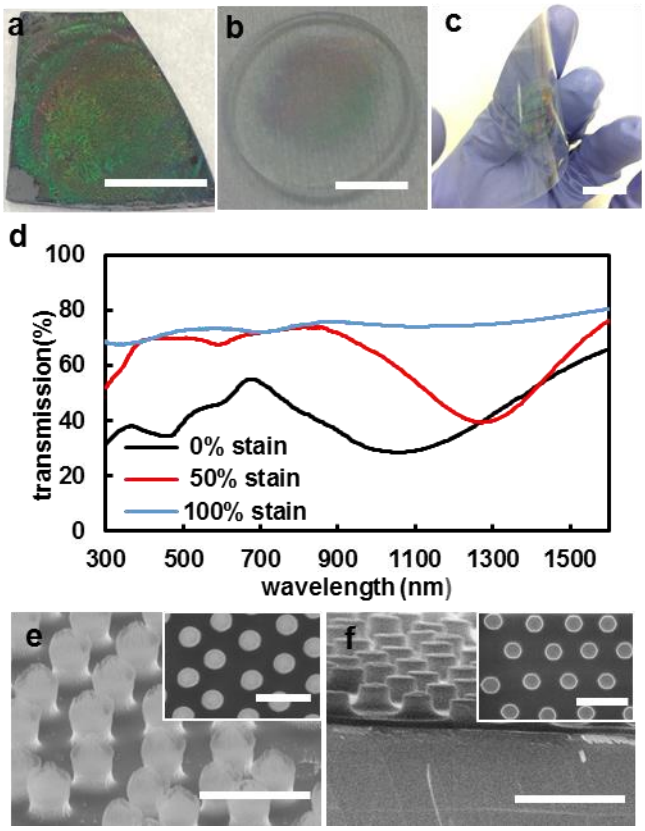

Figure 4.14 Camera images of 100% SAT nanosphere array on a. silicon wafer, b. quartz, c. flexible PET film; d. the transmission spectra of the three SAT samples (0%, 50%, 100%) on the quartz substrates; e. an array of the fabricated Si nanopillars (insert SEM image: top-view of the Si nanopillar array); f. the pattern of the UV polymer as the original etched Si mold (insert SEM image: top-view of UV pattern array). Scale bar: a-b: 8 mm; c: 15 mm, e-f: 2 μm.

Finally, the Al film coated on the nanospheres can serve as an etch mask for substrate etching. The PS nanospheres of 490 nm nominal diameter were etched to 330 nm in RIE and deposited with a 20 nm-thick Al layer. Once picked up by the PDMS stamp and stretched to 100%, the Al-coated nanospheres were transferred to the SU-8-coated Si substrate. The underlying SU-8 layer as well as the Si substrate was etched in O_2 and CF_4/O_2 plasmas, respectively. Figure 4.14e shows an array of Si nanopillars fabricated with the nanosphere mask. This Si nanopattern was utilized as a mold to create a UV nanoimprint replica. Briefly, we first created the inversed pattern

of a UV polymer (ZPUA, Gelest Inc.) on a PET film, which was then used to transfer the nanopattern onto a new Si substrate using UV nanoimprinting lithography. The pattern of the UV polymer on the original etched Si mold was replicated on the new Si surface (see Fig. 4.14f), suggesting that nanostructures initially patterned by the nanosphere lithography template can be reproduced many times because of the nature of the nanoimprinting process. This feature is important when the exactly same pattern is required for the specific applications. As illustrated in Fig. 4.13, the stochastic nature of self-assembly in nanosphere lithography cannot produce the exactly same pattern – i.e., each time nanospheres are assembled on the non-patterned surface, the resulting assemblies are different in terms of the grain size, location and orientation. Therefore, the combination of the nanosphere lithography and nanoimprinting lithography provides an inexpensive platform for reproducibly producing nanopatterns. With the flexibility offered by our SAT approach, the pitch of the resulting hexagonal nanopatterns is not limited to the original nanosphere dimensions but can be substantially modified over a large area.

4.4 Conclusion

We combined colloidal lithography and deformable soft lithographic transfer in a simple and robust technique that creates well-separated, highly-ordered, large area 2D arrays of hexagonal nanospheres. To overcome the limitations of the previous approaches such as solvent swelling and uniaxial/biaxial stretching of an elastomer substrate, our custom radial stretching apparatus permits isotropic deformation of a deformable substrate like PDMS. As a result, our modified arrays maintain their original hexagonal arrangement over large areas and regardless of the initial crystalline orientations. We demonstrated that the prepolymer-to-curing-agent-ratio of PDMS could be tuned to achieve an increase in pitch as large as 213% in 2D nanosphere assemblies using a single stretching-and-transfer process. The array pitch measured from the image analysis was

always smaller than the nominal pitch calculated from the applied strain, and the discrepancy grew larger with increasing strain due to the spatial non-uniformity of the PDMS stretching. The hexagonally-ordered non-close-packed nanosphere array was transferred onto target substrates including a Si wafer, quartz, and plastics. The arrays were employed as etch masks and molds for fabricating periodic nanostructure arrays which may be useful in sensing and optoelectronic applications.

REFERENCES

REFERENCES

1. Schaffner, M.; England, G.; Kolle, M.; Aizenberg, J.; Vogel, N. Combining Bottom-Up Self-Assembly with Top-Down Microfabrication to Create Hierarchical Inverse Opals with High Structural Order. *Small* **2015**, *11*, 4334–4340.

2. Vogel, N.; Weiss, C. K.; Landfester, K. From soft to hard: the generation of functional and complex colloidal monolayers for nanolithography. *Soft Matter* **2012**, *8*, 4044–4061.

3. Vogel, N.; Retsch, M.; Fustin, C.-A.; del Campo, A.; Jonas, U. Advances in Colloidal Assembly: The Design of Structure and Hierarchy in Two and Three Dimensions. *Chem. Rev.* **2015**, *115*, 6265–6311.

4. Yu, B.; Zhai, F.; Cong, H.; Yang, D. Photosensitive polystyrene/silver bromide hybrid colloidal crystals as recoverable colorimetric naked eye probes for bromine gas sensing. *J. Mater. Chem. C* **2016**, *4*, 1386–1391.

5. Yi, Z.; Niu, G.; Liu, J.; Kang, X.; Yao, W.; Zhang, W.; Yi, Y.; Yi, Y.; Ye, X.; Duan, T.; Tang, Y. Ordered array of Ag semishells on different diameter monolayer polystyrene colloidal crystals: An ultrasensitive and reproducible SERS substrate. *Sci. Rep*. **2016**, *6*, 32314.

6. Zhang, X.; Xiao, X.; Wu, W.; Zhang, X.; Jiang, C. Ultrasensitive SERS performance in 3D 'sunflower-like' nanoarrays decorated with Ag nanoparticles. *Nanoscale* **2017**, *9*, 3114–3120.

7. McNew, C. P.; Kananizadeh, N.; Li, Y.; LeBoeuf, E. J. The attachment of colloidal particles to environmentally relevant surfaces and the effect of particle shape. *Chemosphere* **2017**, *168*, 65–79.

8. Li, F.; Josephson, D. P.; Stein, A. Colloidal Assembly: The Road from Particles to Colloidal Molecules and Crystals. *Angew. Chem. Int. Ed.* **2011**, *50*, 360–388.

9. Talapin, D. V.; Lee, J.-S.; Kovalenko, M. V.; Shevchenko, E. V. Prospects of Colloidal Nanocrystals for Electronic and Optoelectronic Applications. *Chem. Rev.* **2010**, *110*, 389–458.

10. Yang, X.; Ge, D.; Wu, G.; Liao, Z.; Yang, S. Production of Structural Colors with High Contrast and Wide Viewing Angles from Assemblies of Polypyrrole Black Coated Polystyrene Nanoparticles. *ACS Appl. Mater. Interfaces* **2016**, *8*, 16289–16295.

11. Haynes, C. L.; Van Duyne, R. P. Nanosphere Lithography: A Versatile Nanofabrication Tool for Studies of Size-Dependent Nanoparticle Optics. *J. Phys. Chem. B* **2001**, *105*, 5599–5611.

12. Yasukawa, Y.; Asoh, H.; Ono, S. Site-Selective Metal Patterning/Metal-Assisted Chemical Etching on GaAs Substrate through Colloidal Crystal Templating. *ECS Trans.* **2008**, *13*, 83–92.

13. Cao, B.; Cai, W.; Sun, F.; Li, Y.; Zhang, L. Fabrication of large-scale zinc oxide ordered pore arrays with controllable morphology. *Chem. Commun*. **2004**, 1604–1605.

14. Hatton, B.; Mishchenko, L.; Davis, S.; Sandhage, K. H.; Aizenberg, J. Assembly of large-area, highly ordered, crack-free inverse opal films. *Proc. Natl. Acad. Sci.* **2010**, *107*, 10354–10359.

15. Huang, X.; Ratchford, D.; Pehrsson, P. E.; Yeom, J. Fabrication of metallic nanodisc hexagonal arrays using nanosphere lithography and two-step lift-off. *Nanotechnology* **2016**, *27*, 395302.

16. Paik, T.; Diroll, B. T.; Kagan, C. R.; Murray, C. B. Binary and Ternary Superlattices Self-Assembled from Colloidal Nanodisks and Nanorods. *J. Am. Chem. Soc.* **2015**, 137, 6662–6669.

17. Sun, Z.; Li, Y.; Zhang, J.; Li, Y.; Zhao, Z.; Zhang, K.; Zhang, G.; Guo, J.; Yang, B. A Universal Approach to Fabricate Various Nanoring Arrays Based on a Colloidal-Crystal-Assisted-Lithography Strategy. *Adv. Funct. Mater*. **2008**, 18, 4036–4042.

18. Chen, J.; Liao, W.; Chen, X.; Yang, T.; Wark, S.; Son, D.; Batteas, J.; Cremer, P. Evaporation-Induced Assembly of Quantum Dots into Nanorings. *ACS Nano* **2009**, *3*, 173–180.

19. Vogel, N.; Fischer, J.; Mohammadi, R.; Retsch, M.; Butt, H.J.; Landfester, K.; Weiss, C.K.; Kreiter, M. Plasmon Hybridization in Stacked Double Crescents Arrays Fabricated by Colloidal Lithography. *Nano Lett*. **2011**, *11*, 446–454.

20. Bochenkov, V. E.; Sutherland, D. S. From Rings to Crescents: A Novel Fabrication Technique Uncovers the Transition Details. *Nano Lett.* **2013**, *13*, 1216–1220.

21. Cataldo, S.; Zhao, J.; Neubrech, F.; Frank, B.; Zhang, C.; Braun, P.V.; Giessen, H. Hole-Mask Colloidal Nanolithography for Large-Area Low-Cost Metamaterials and Antenna-Assisted Surface-Enhanced Infrared Absorption Substrates. *ACS Nano* **2012**, *6*, 979–985.

22. Choi, H. K.; Yang, Y. J.; Park, O. O. Hemispherical Arrays of Colloidal Crystals Fabricated by Transfer Printing. *Langmuir* **2014**, *30*, 103–109.

23. Peng, K.; Zhang, M.; Lu, A.; Wong, N.; Zhang, R.; Lee, S. Ordered silicon nanowire arrays via nanosphere lithography and metal-induced etching. *Appl. Phys. Lett.* **2007**, *90*, 163123.

24. Li, L.; Zhai, T.; Zeng, H.; Fang, X.; Bando, Y.; Golberg, D. Polystyrene sphere-assisted one-dimensional nanostructure arrays: synthesis and applications. *J. Mater. Chem.* **2010**, *21*, 40–56.

25. Vogel, N. *Surface Patterning with Colloidal Monolayers*. Springer Berlin Heidelberg, 2012.

26. Jiang, P.; McFarland, M. J. Large-Scale Fabrication of Wafer-Size Colloidal Crystals, Macroporous Polymers and Nanocomposites by Spin-Coating. *J. Am. Chem. Soc*. **2004**, *126*, 13778–13786.

27. Tsuji, S.; Kawaguchi, H., Self-Assembly of Poly (N-isopropylacrylamide)-Carrying Microspheres into Two-Dimensional Colloidal Arrays. *Langmuir* **2005**, *21*, 2434-2437.

28. Plettl, A.; Enderle, F.; Saitner, M.; Manzke, A.; Pfahler, C.; Wiedemann, S.; Ziemann, P. Non-Close-Packed Crystals from Self-Assembled Polystyrene Spheres by Isotropic Plasma Etching: Adding Flexibility to Colloid Lithography. *Adv. Funct. Mater*. **2009**, *19*, 3279–3284.

29. Yeom, J.; Ratchford, D.; Field, C. R.; Brintlinger, T. H.; Pehrsson, P. E. Decoupling Diameter and Pitch in Silicon Nanowire Arrays Made by Metal-Assisted Chemical Etching. *Adv. Funct. Mater*. **2014**, *24*, 106–116.

30. Yan, X.; Yao, J.; Lu, G.; Li, X.; Zhang, J.; Han, K.; Yang, B. Fabrication of Non-Close-Packed Arrays of Colloidal Spheres by Soft Lithography. *J. Am. Chem. Soc.* **2005**, *127*, 7688–7689.

31. Li, X.; Wang, T.; Zhang, J.; Yan, X.; Zhang, X.; Zhu, D.; Li, W.; Zhang, X.; Yang, B. Modulating Two-Dimensional Non-Close-Packed Colloidal Crystal Arrays by Deformable Soft Lithography. *Langmuir* **2010**, *26*, 2930–2936.

32. Wang, Y.; Balowski, J.; Phillips, C.; Phillips, R.; Sims, C.E.; Albritton, N.L. Benchtop micromolding of polystyrene by soft lithography. *Lab. Chip* **2011**, *11*, 3089–3097.

33. Kumnorkaew, P.; Ee, Y.-K.; Tansu, N.; Gilchrist, J. F. Investigation of the Deposition of Microsphere Monolayers for Fabrication of Microlens Arrays. *Langmuir* **2008**, *24*, 12150–12157.

34. Aizenberg, J.; Braun, P. V.; Wiltzius, P. Patterned Colloidal Deposition Controlled by Electrostatic and Capillary Forces. *Phys. Rev. Lett*. **2000**, *84*, 2997–3000.

35. Feng, X.; Meitl, M.A.; Bowen, A.M.; Huang, Y.; Nuzzo, R.G.; Rogers, J.A. Competing Fracture in Kinetically Controlled Transfer Printing. *Langmuir* **2007**, *23*, 12555–12560.

36. Yeom, J.; Shannon, M. A. Detachment Lithography of Photosensitive Polymers: A Route to Fabricating Three-Dimensional Structures. *Adv. Funct. Mater*. **2010**, *20*, 289–295.

37. Choy, W. C. H. The emerging multiple metal nanostructures for enhancing the light trapping of thin film organic photovoltaic cells. *Chem. Commun*. **2014**, *50*, 11984–11993.

38. Kim, T. K.; Kim, J. K.; Jeong, O. C. Measurement of nonlinear mechanical properties of PDMS elastomer. *Microelectron. Eng*. **2011**, *88*, 1982–1985.

39. Choi, H. K.; Im, S. H.; Park, O. O. Shape and feature size control of colloidal crystal-based patterns using stretched polydimethylsiloxane replica molds. *Langmuir* **2009**, *25*, 12011–12014.

40. Sun, Z.; Yang, B. Fabricating colloidal crystals and construction of ordered nanostructures. *Nanoscale Res. Lett*. **2006**, *1*, 46–56.

41. Khanafer, K.; Duprey, A.; Schlicht, M.; Berguer, R. Effects of strain rate, mixing ratio, and stress–strain definition on the mechanical behavior of the polydimethylsiloxane (PDMS) material as related to its biological applications. *Biomed. Microdevices* **2009**, *11*, 503–508.

42. Venditti, I.; Fratoddi, I.; Palazzesi, C.; Prosposito, P.; Casalboni, M.; Cametti, C.; Battocchio, C.; Polzonetti, G.; Russo, M.V. Self-assembled nanoparticles of functional copolymers for photonic applications. *J. Colloid Interface Sci*. **2010**, *348*, 424–430.

CHAPTER 5

FABRICATION OF METALLIC NANODOT HEXAGONAL ARRAYS USING NANOSPHERE LITHOGRAPY AND DOUBLE LIFT OFF

5.1 Introduction

Metallic nanoparticle and nanodot (or nanodisc) arrays attract great interest thanks to their versatility and utility. They exhibit localized surface plasmon resonances, which enhance optical absorption, scattering, and focusing[1–6]. As a result they have been used in applications including biosensing[7–9], optical antennas[10] and surface enhanced Raman scattering (SERS)[11–16]. Nanodot arrays have also been used in various patterning processes, where they serve as masks for etching and evaporation, seed materials or reaction substrates for nanostructure growth[17], and molds for replication[18]. Simultaneous control of particle size and their relative arrangement is important in ordered nanodot arrays for optical applications[19]. Many top-down and bottom-up methods have been used to fabricate ordered arrays of metallic nanostructures, including photolithography, focused ion beam milling[20,21], electron beam lithography[22], self-assembly[23], and template-based methods using nanosphere lithography[24–26] or an anodized alumina membrane[27]. Among them, nanosphere lithography (NSL) offers a simple and low-cost way to create periodic nanostructures like metallic nanoparticles/nanodots over a relatively large area[28]. Moreover, NSL provides design flexibility, as the density and size of the NSL-patterned nanoparticles can be tuned – a feature that is not commonly found in other inexpensive bottom-up methods[29].

NSL relies on a spin-coating or controlled convective/evaporative process to produce two-dimensional (2D) colloidal crystals in a hexagonally close-packed array on a substrate[26]. The nanospheres in the array can serve as a physical mask. Due to the simple nature of the NSL templating method, ordered metal nanoparticle arrays are easily fabricated by combining NSL with

metal evaporation[30]. A wide variety of metal nanoparticle array geometries have been fabricated by controlling the number of nanosphere layers during metal deposition[31–33], deposition angle and duration[34,35], thermal- or e-beam treatment of nanospheres[22], and post-treatment of the obtained nanodot arrays. However, the majority of the nanodot arrays obtained from the NSL template are restricted to the hexagonally ordered triangular arrays as the metal layer is deposited into interstitial spaces among nanospheres[32]. To our surprise, metallic nanodot arrays with the same arrangement as the original nanosphere array have been rarely found in literature. One approach is to use a combination of NSL templating, hydrophobic treatment, and subsequent site-selective electroless deposition[36,37]. Another is to utilize the NSL-based hemispherical elastomer stamp together with a nano-transfer printing method[38]. However, the resulting nanodots from these methods are irregularly shaped or noncontiguous compared to the nanodots obtained from the physical vapor deposition of metals. The type of the nanodot materials is also restricted due to the limited compatibility of the electroless deposition or transfer printing. Therefore, a scalable fabrication procedure of creating a well-defined, high quality hexagonal array of metallic nanodots with the same arrangement of the original nanosphere array needs to be developed.

In this chapter, we combine NSL templating with a facile double lift-off process to obtain a high-quality hexagonal array of metallic nanodots, i.e., in the same arrangement as the original nanosphere array. Here, the double lift-off process denotes two consecutive metal lift-off steps. In the first step, an initial metal layer is deposited over the reduced nanosphere array which serves as a lift-off mask. In the second step, the first metal layer now serves as another lift-off mask for the target nanodot metal. Because the lift-off processes are performed twice, the resultant nanostructures are discrete features with the same placement as the original nanosphere template. This combined technique produces a highly-ordered hexagonal array of well-defined metallic

nanodots over a relatively large area. In order to assist the second lift-off step, we employ two different metal layers and create re-entrant sidewall profiles by sacrificial etching of the underlying metal layer, significantly improving the lift-off yield. This ordered metallic nanodot array also serves as an etch mask in reactive ion etching (RIE) and is used to produce a large-area, hexagonal array of silicon nanowires exhibiting highly anti-reflecting structures in almost all UV and visible wavelengths.

5.2 Experiment Section

Substrate preparation: The substrate preparation was previously reported[29]. Briefly, four-inch single-side-polished silicon wafers (Montco silicon, <100> orientation and 500 μm in thickness, N-type, 8-12 Ω cm) were cut into 2 cm by 2 cm coupons, which were ultrasonically cleaned in acetone and isopropyl alcohol for 5 min. The Si coupons were further cleaned in piranha solution (H_2SO_4: H_2O_2 =3:1) for 30 min and subsequently in standard cleaning solution (H_2O_2: NH_4OH: deionized water= 1:1:5) for 30 min to render their surfaces hydrophilic. The coupons were then thoroughly rinsed with DI water and stored in DI water until used.

Nanosphere Lithography: Polystyrene nanospheres (nanospheres) with a monodisperse diameter of 0.5 μm were purchased from Polysciences Inc. and mixed with a 400:1 solution of methanol: Triton X-100 as 3:1 (3 part of nanosphere, 1 part of a mixture of methanol and Triton X-100). In order to form an hexagonally close-packed monolayer, the nanosphere solution was spin-coated onto each coupon at 400, 500, and 1400 rpm (for 30s, 2 min, and 10s, respectively). The nanosphere-coated substrate was then dried overnight.

Nanodot Fabrication: The nanospheres were etched in an ICP-RIE (Oxford Plasmalab System 100) to reduce the nanosphere size and separate them. The parameters for the RIE plasma were a

mixture of O_2 and CF_4 (40 and 10 sccm, respectively), 20 mTorr of a chamber pressure, 800 W of an ICP power, 10 W of a platen power, and -20°C for platen temperature. Etching time was controlled to reduce the nanosphere diameter to 230~250 nm. The bilayer of 50-nm-thick Al and 50-nm-thick Au was evaporated on top of the nanosphere arrays in a Temescal e-beam evaporator (background pressure less than 1×10^{-6} Torr). A semiconductor dicing tape or cured polydimethylsiloxane (PDMS) stamp was used to remove the nanospheres and obtain the nanohole array in the Al/Au film. The Al layer was undercut to create a re-entrant sidewall profile by immersing the sample into the Al Etchant Type A solution (16 part H_3PO_4, 1 part HNO_3, 1 part HAc, 2 parts H_2O) for 10s. Next, a 25–nm-thick Cr layer was evaporated on the substrate also using a Temescal e-beam evaporator. In the final lift-off step, the coupon was immersed into the Al Etchant Type A solution with mild sonication for 1 min. The coupon was cleaned with a copious amount of DI water and dried for imaging.

Si Nanowire Fabrication: The silicon substrate was etched using the Cr nanodot array as an etch mask in the ICP-RIE (Oxford Plasmalab System 100). Tapered SiNWs were produced using 60 sccm of SF_6 and 8 sccm of O_2, 800 W of ICP power, 7 W of platen power, and a platen temperature of 110°C.

Imaging and Analysis: SEM images were obtained using a Carl Zeiss SMT Supra 55 (field-emission high-resolution SEM) instrument. Image analysis was performed using ImageJ.

5.3 Results and Discussion

5.3.1 Challenges of conventional lift-off process

Hypothetically we can consider two approaches to obtaining the desired metallic nanodot array by combining the NSL technique with physical vapor deposition. The first approach is to

create the 2D polystyrene (PS) nanosphere array on a substrate already coated by a thin metal layer[39], reduce the nanosphere diameters by RIE, and then dry etch the metal layer directly using the nanosphere array as an etch mask (see Figure 5.1a). The challenge of this approach is that for a given dry etch chemistry for the metal film, the PS nanospheres function poorly as the etch mask. The second approach is a double lift-off method, as shown in Figure 5.1b, - the first nanosphere lift-off using a relatively thick metal film is followed by a second lift-off with a thin film of another metal. The thickness of the metal layer in the first lift-off step should be larger than that in the second lift-off step, so that the second metal film breaks at the edge of the protrusion and the underlying metal layer is etched through the formed gap. Prior to the double lift-off process, the nanosphere size is reduced with RIE to a desired diameter. Ideally, the line-of-sight nature of physical vapor deposition enables the first (thicker) metal layer to have a straight sidewall, which in turn assists the subsequent lift-off. However, in reality, when a 2D nanosphere array is used as a deposition mask, the line-of-sight evaporation leads to a positive slope of the deposited metal layer (see Figure 5.1c). When the mask layer exhibits a positive slope in the sidewall profile, the subsequent metal evaporation step forms an uninterrupted contiguous film, which is detrimental to the final lift-off process. The formation of the positive slope in the metal layer obtained from the NSL-based lift-off process can be attributed to two factors: (i) the surface diffusion allows metal atoms to migrate towards the space underneath the reduced nanospheres (see the inset of Figure 5.1c) and (ii) more importantly, dynamic shadowing from the metal film deposited onto the nanospheres renders the film deposited on the substrate to be three dimensional and prismatic[40]. The latter effect is fundamental in vacuum deposition and becomes significant when a thick metal film is deposited through the NSL-based mask. Assuming the vapor flux is perpendicular to the substrate, the vertical growth of the metal film is always accompanied by the lateral growth on the

masking structure (in this case, nanospheres). Thus, the lateral deposition of metal on the nanospheres effectively reduces the opening of the masking structure, producing a positive sidewall profile of the resulting metal film.

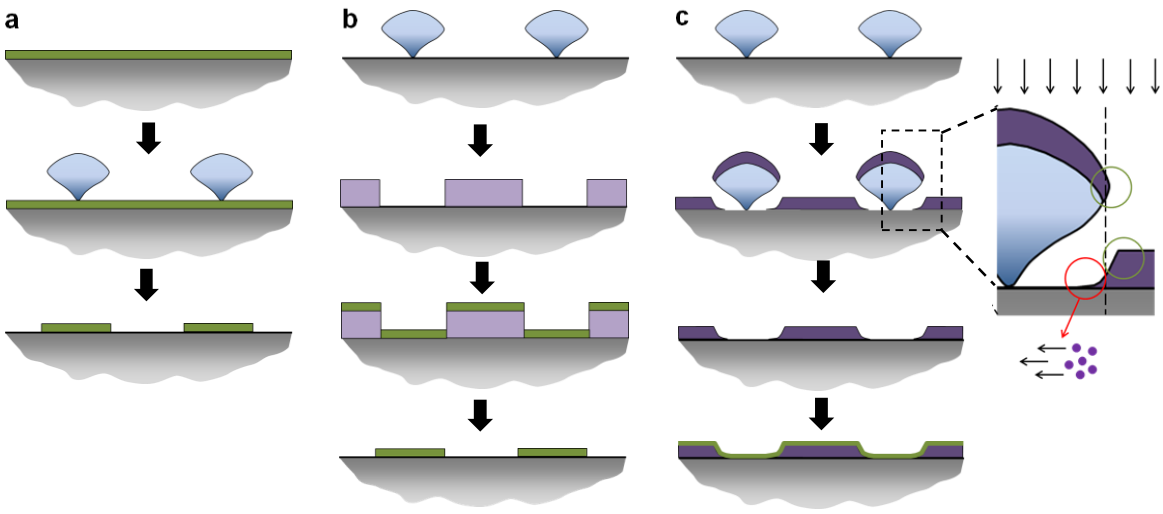

Figure 5.1 Hypothetical approaches for NSL-based metal nanodot fabrication; (a) metal etching with the nanosphere mask (green = target metal layer), (b) double lift-off (purple = sacrificial metal layer), (c) challenge of the double lift-off process –dynamic shadowing and lateral particle diffusion create a positive sidewall profile and impede subsequent lift-off.

5.3.2 Our approach combined NSL with double lift-off

To address this issue, we deposit a bilayer of two dissimilar metals in the first lift-off step and selectively undercut the bottom layer. This creates a negative or re-entrant sidewall profile in the initial metal film, assisting the second lift-off step. Figure 5.2 shows the key fabrication steps to generate a hexagonal array of metallic nanodots using the modified double lift-off process. Each of the steps is depicted in the SEM images in Figure 5.3. Unlike the general double lift-off process that usually employs one sacrificial layer for etching the structure, this modified process require a sacrificial metal bilayer to mitigate surface diffusion on the bottom metal layer and lead to a cap-like structure.

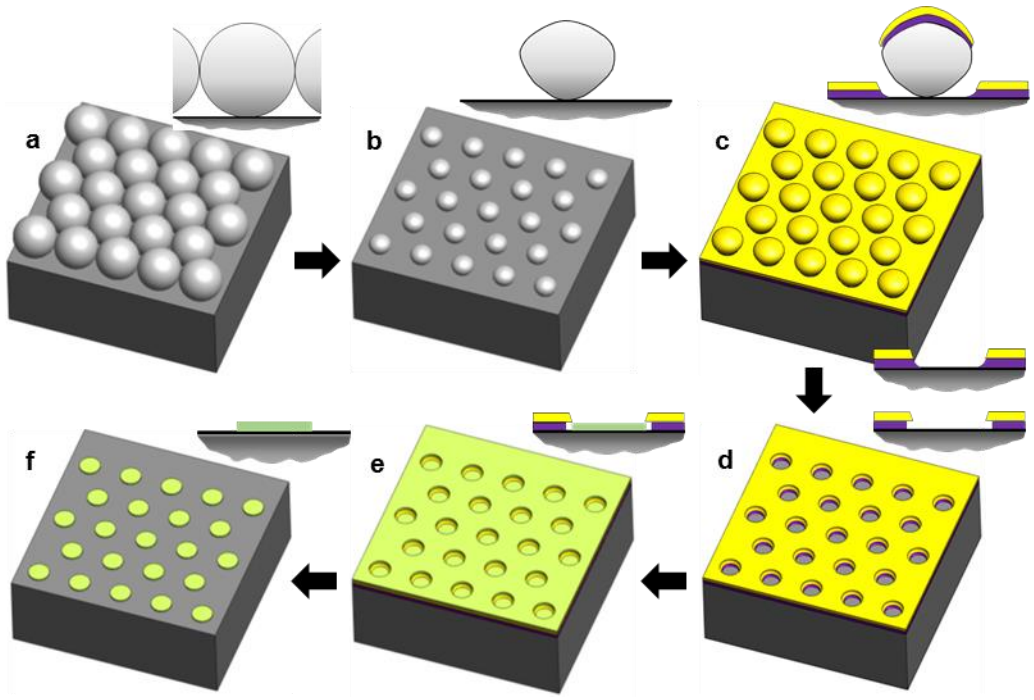

Figure 5.2 (a-f) Schematic diagram of the proposed double lift-off process to fabricate metallic nanodots (white: nanospheres, purple: sacrificial metal layer, yellow: cap metal layer, and green: target metal layer). Each 3D diagram has an accompanying cross-sectional inset image for clarity.

A simple spin-coating technique was used to create 2D colloidal crystals on silicon substrates (Figure 5.2a)[41]. Prior to spin-coating, the silicon substrates were cleaned in a standard cleaning solution to render their surfaces hydrophilic (see the Experimental section). Dispersion of polystyrene (PS) nanosphere (500 nm in nominal diameter) and surfactant was spin-coated in multiple ramping/spinning steps to create a uniform nanosphere monolayer. The nanosphere size was then reduced to half the initial diameter in RIE using a plasma discharge in a mixture of O_2 and CF_4, resulting relatively smooth nanospheres (see Figure 5.2b)[29]. With the reduced nanosphere array as a masking layer, a bilayer of 50-nm-thick Aluminum (Al) and 50-nm-thick gold (Au)was deposited on top of the reduced nanospheres and Si substrate (Figure 5.2c). The metal-decorated nanospheres were then removed from the substrate either by scotch tape, solvents such as

chloroform, or a flat viscoelastic stamp made of polydimethylsiloxane (PDMS) (Figure 5.2d). For reasons illustrated earlier, the 100-nm-thick bilayer film exhibits a positive slope on the sidewall, which inhibits the subsequent liftoff process. Figure 5.3a and 5.3b show cross-sectional scanning electron microscope (SEM) images of the Si sample after bilayer deposition and nanosphere lift-off, respectively, and clearly show the bilayer's positive slope. If we used this metal layer as a shadow mask and proceeded with the second lift-off step, the subsequent metal layer would form a continuous film and prevent etchants from attacking the underlying the first metal layer, i.e., failure of the second lift-off step.

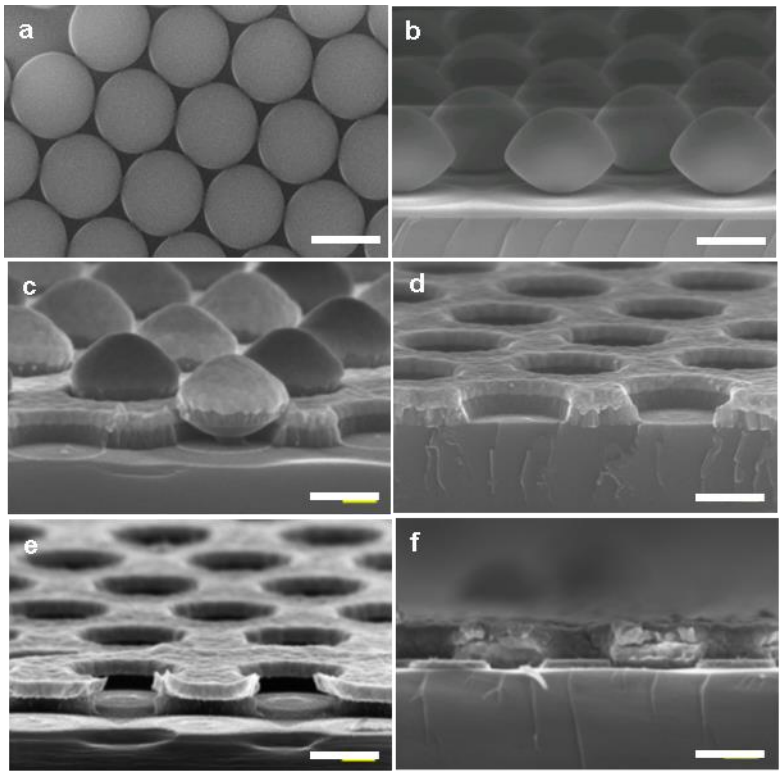

Figure 5.3 SEM images of the key process steps: (a) as-deposited 2D colloidal crystal of 500 nm PS nanospheres, (b) size reduction in PS nanospheres etched by ICP-RIE, (c) reduced nanospheres coated with a bilayer of 50 nm of Al and 50 nm of Au, (d) nanospheres removed using tape or a PDMS stamp to leave the Al/Au bilayer with nanohole arrays (Note: a positive sidewall profile is clearly visible), (e) sacrificial Al layer etching to create the re-entrant sidewall profile, (f) deposition of 25 nm of Cr. All scale bars are 200 nm.

To create a re-entrant sidewall profile, we etched the bottom layer (Al) of the bimetallic sacrificial layer just slightly to create an undercut structure, with the Au layer overhung as shown in Figure 5.3c. The cross-sectional inset image in Figure 5.2d also schematically shows this undercutting step. Controlling the etch rate and etch time is critical to achieving the proper undercut structure. Obviously, the Al layer needs to be etched sufficiently to remove the positive slope, but if it is etched too long, the top Au layer will lift off or its overhang structure will collapse. Once the desired re-entrant sidewall profile was obtained, a final (3^{rd}) chromium (Cr) layer was deposited to form the nanodot array (see Figure 5.2e and 5.3d). The Cr thickness was smaller than that of the Al (1^{st}) layer, creating a gap between the two layers to facilitate the last lift-off process. Finally, the substrate was immersed in an Al etchant solution to allow the etchant to attack the underlying Al layer and complete the lift-off of the Al/Au layer (Figure 5.2f). Figure 5.4 shows SEM images of the resultant hexagonal array of Cr nanodots in various magnifications and viewing angles. The highly ordered Cr nanodot array was obtained over a large area ($> 20\ mm^2$) (see Figure 5.4a) with a negligible defect density (< 3%). Defective nanodot areas arise either from the initial nanosphere assembly or from the first lift-off step (i.e., nanosphere removal). Since this paper deals with the nanodot fabrication via the double lift-off process, we focused on the defects occurring during the lift-off processes. Figure 5.4b shows a representative zoom-in image of the Cr nanodot array with a few missing nanodots (observed in the left middle and bottom row), which we attribute to incomplete nanosphere removal during the initial lift-off process. Dry lift-off (using a tape or PDMS stamp) was more effective than wet etching of nanospheres. The patterning defect rate, however, is very low – according to Figure 5.4b, 5 missing out of 437 nanodots amounts to

only 1.1%. In addition, the position of the nanodots precisely matches the original nanosphere array.

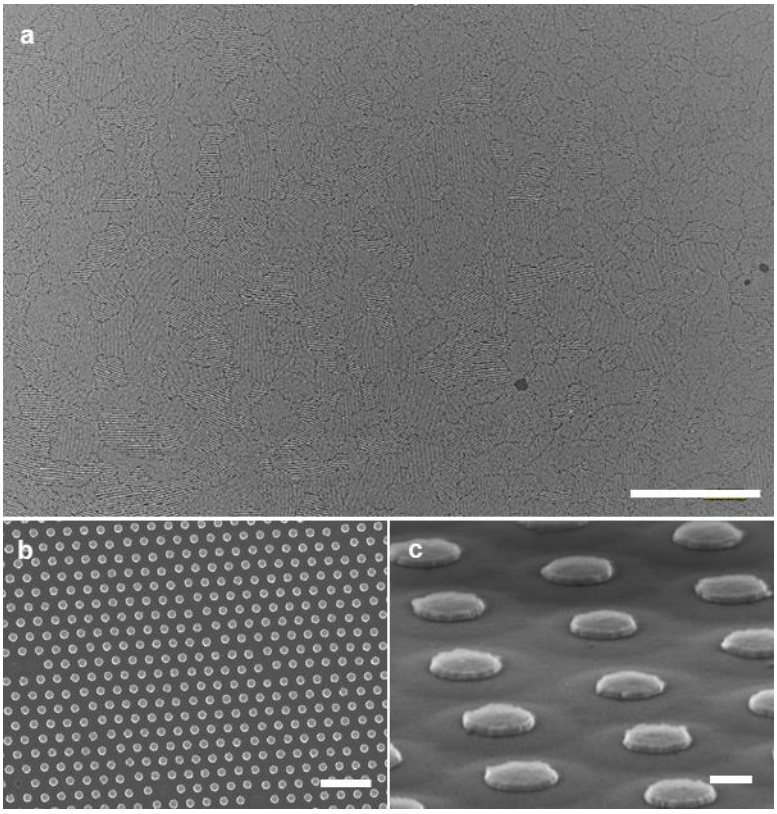

Figure 5.4 SEM images of Cr nanodots array at various magnifications and viewing angles: (a) and (b) from top down, (c) 70° tilted. Scale bar is 100 μm for (a), 2 μm for (b), and 100 nm for (c).

5.3.3 Original order and size control

The nanodot's size, shape and hexagonal arrangement (in comparison to the original nanosphere array) were quantified by analyzing the SEM images for fitted diameter, roughness, and pitch. The fitted diameter was calculated from the two-dimensional projection area of the nanostructure (etched nanosphere, nanohole, or nanodots). The roughness factor, defined as a ratio between the actual perimeter of the two-dimensional projection and the perimeter computed from the fitted diameter, was also estimated. The disturbance of the array lattice was quantified by

measuring the pitch, that is, the center to center distance between two neighboring nanostructures[29]. Figure 5.5 presents the fitted diameter, roughness factor, and pitch of the nanostructure array at each processing step including nanosphere reduction (open square), nanoholes after the nanosphere removal (closed square), and Cr nanodots (open circle). The histogram of the fitted diameter in Figure 5.5a indicates that the averaged diameters of the reduced nanospheres, nanoholes after the 1st lift-off, and nanodots are 232 nm (±4 nm), 239 nm (±4 nm), and 240 nm (±7 nm), respectively. The numbers in the parentheses and the error bars seen in Figure 5b and 5c represent the standard deviation of more than 100 measurements. The average diameter increased from the reduced nanosphere to the nanohole, probably because lateral growth of the metal film on the nanospheres during the bilayer deposition, which effectively increased the nanosphere mask size and enlarged the resulting nanoholes in the bilayer film. As a result, the nanodots were slightly (3.4%) wider than the reduced nanospheres. The roughness of the Cr nanodots and their pitch hardly changed from the original nanosphere array, highlighting their regular, well-defined shape and precise arrangement (see Figure 5.5b and 5.5c).

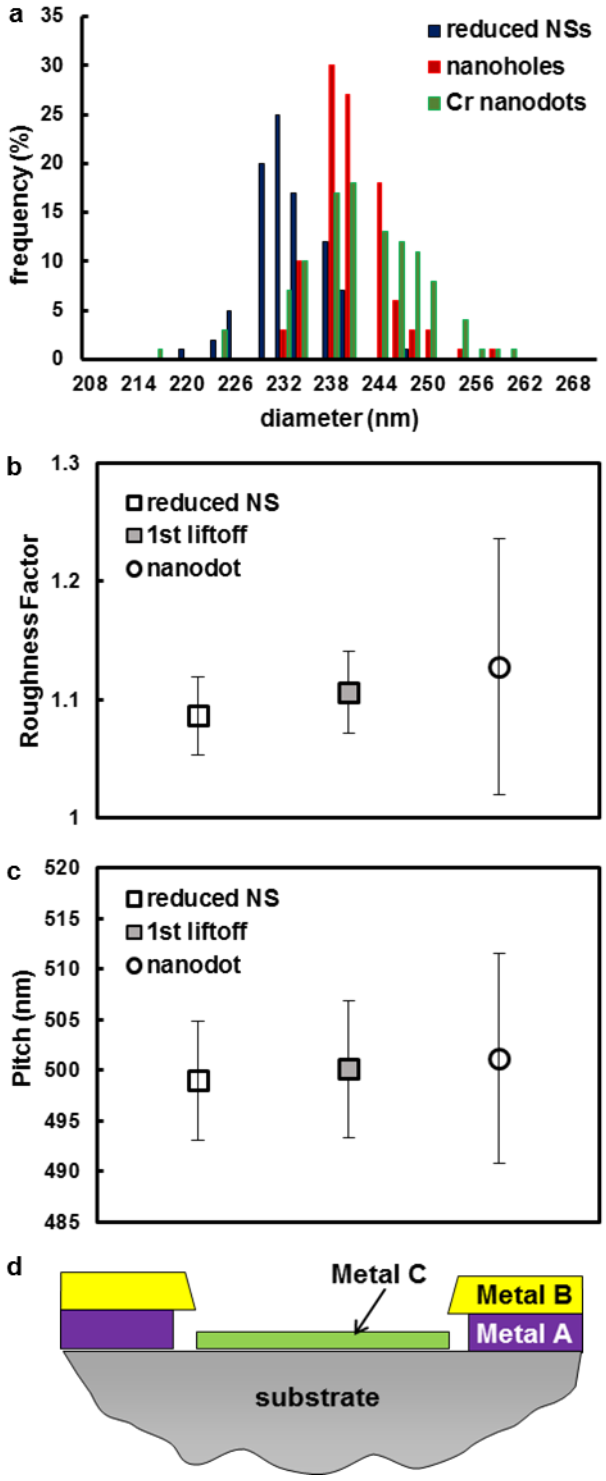

Figure 5.5 (a) Size distribution of 120 individual nanostructures at the three key process steps: dark blue for reduced nanospheres, red for nanoholes after 1st lift-off, green for Cr nanodots. Plots of (b) roughness factor and (c) pitch at those steps with the error bars indicate the standard deviation, while (d) schematically shows the three metal layers involved in the double lift-off process

The bilayer strategy to create a re-entrant sidewall profile for easing lift-off is common for patterning submicron or nanometer-sized metallic features with photolithography or e-beam lithography[42,43]. For example, in e-beam lithography, the e-beam resist or lift-off layer, which is more sensitive to the electron radiation and/or developer solution, is used in the bottom layer. After exposure, both top and bottom layer of the exposed region are developed but the bottom layer is over-developed to create an undercut feature. In our case, the nanodots were created by exploiting the different etch rates of three metals. As seen in Figure 5.5d, the three layers included a sacrificial layer (Metal A), a cap layer (Metal B) that forms a bilayer for the initial lift-off, and a target layer (Metal C) for the desired nanodot material. Care is required in selecting the metals, because metals B and C are exposed to an etchant of Metal A during the double lift-off process and must therefore be relatively inert to the etchant. Metals B and C can be the same material provided Metal C is sufficiently thinner than Metal A. In our case, we chose Al for Metal A, Au for Metal B, and Cr for Metal C, because the Al etchant (a mixture of phosphoric, acetic, and nitric acids) does not attack Au or Cr. We cannot arbitrarily change the order of these metals. For example, Al may not be Metal B or C because both Au and Cr etchants attack Al. This also means that there is a limitation on the nanodot material –metals susceptible to corrosion are less likely to work. If one wants to create Al or copper (Cu)-based nanodots, it is difficult to find an appropriate Metal A, since Al and Cu are damaged by most metal etchants. Williams et. al. reported the etching rates and selectivity of metals and other materials in various etching solutions for microelectronics and microelectromechanical system applications[44,45]. According to their work, if Al is used as the sacrificial layer (Metal A), potential nanodot metals include tungsten, platinum, palladium, silver,

Au, Cr, titanium, tantalum, vanadium, and molybdenum. However, copper or nickel nanodots cannot be created because Aluminum etchant Type A etches both metals.

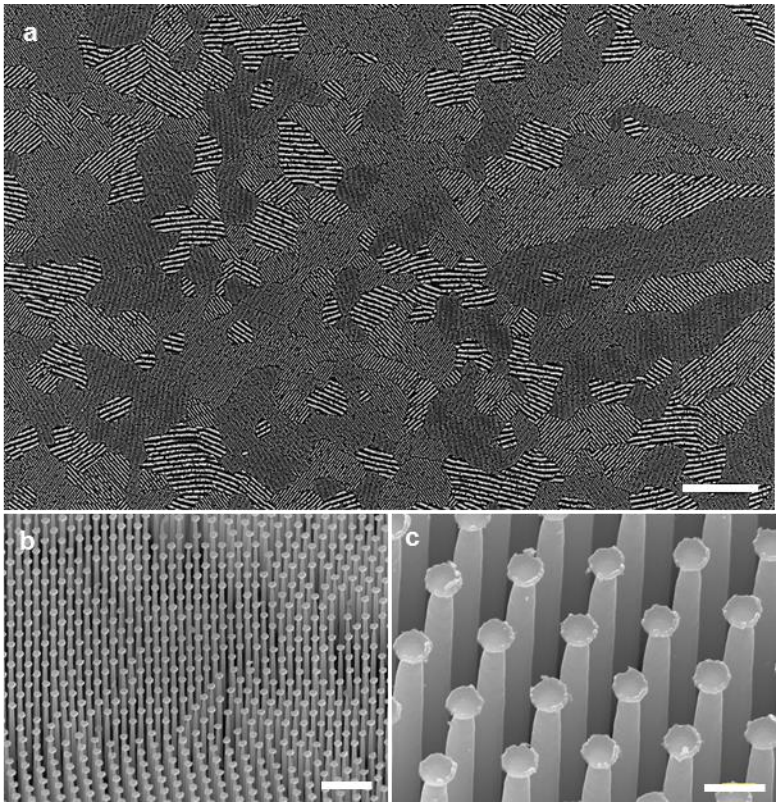

Figure 5.6 (a-c) SEM images (at various magnifications and tilted at 45°) of ICP-RIE-etched, vertically-aligned Si nanowire arrays with the Cr nanodots as the etch mask. Scale bar is 40 μm for (a), 2 μm for (b), and 400 nm for (c).

Finally, the hexagonal Cr nanodot array was used as an etch mask in RIE to create vertically-aligned silicon nanowires (Si NWs). There are other NSL-based techniques that one could use to make the Si NWs with fewer required steps. Most notably, metal-assisted chemical etching (MACE) combined with NSL has been extensively employed for fabricating ordered Si NW arrays with the same hexagonal arrangement[2946]. However, this NSL/MACE approach can introduce substantial porosity into the NWs[47,48] and is essentially limited to Si[49]. Here we performed cryogenic Si etching in an inductively-coupled plasma RIE (ICP-RIE) system to create

nonporous Si NWs with extremely smooth sidewalls. Figure 5.6 reveals the SEM images of the etched Si NWs at various magnifications and a 45° tilt. As with the nanodot array, the vertically-aligned Si NW array extended over a large area without defects, and the hexagonal array arrangement was well preserved. The grayscale interference pattern in Figure 5.6a reveals the different orientations of the colloidal crystal domains carried over from the nanosphere assembly. The Cr nanodots remained virtually intact during Si etching, and acted as a cap on each NW. The ICP-RIE recipe was tuned to produce the tapered NW array with an aspect ratio of approximately 11.6 (see Figure 5.7). Such high aspect-ratio, tapered NW arrays are efficient anti-reflecting surfaces[50]. Our Si NW arrays exhibited strong anti-reflecting character (less than 1%) for wavelengths ranging from 200 to 1000 nm (see Figure 5.8). Our fabrication scheme thus presents a quick, easy, bottom-up process for creating tapered Si NW arrays for anti-reflectance applications.

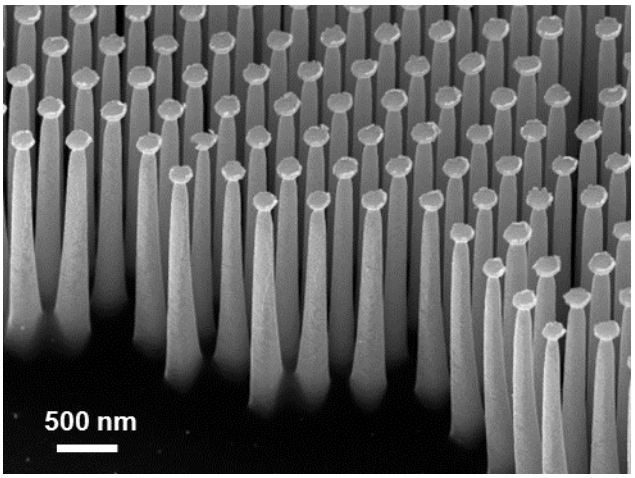

Figure 5.7 An SEM image of the ICP-RIE-etched tapered Si NW array with an aspect ratio of approximately 11.6. The aspect ratio was calculated by dividing the height (2.8 μm) of the Si NW by the diameter (240 nm).

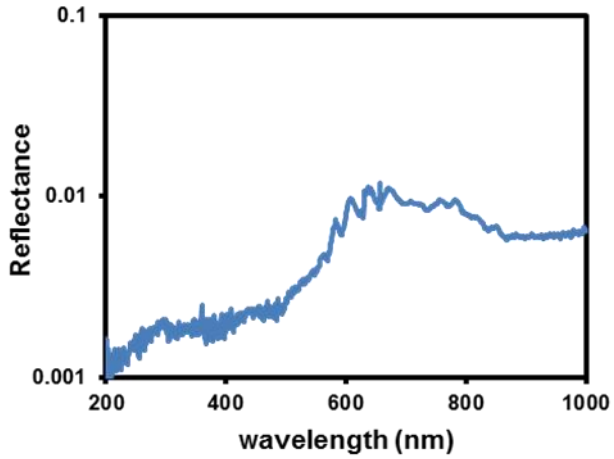

Figure 5.8 Reflectance measurement (in log-scale) of the tapered Si NW array after the Cr nanodots were removed. The laser was directed perpendicular to the substrate. The measurement was performed using an n & k analyzer 1200 (n&k Technology).

5.4 Conclusion

We combined nanosphere lithography (NSL) and a double lift-off process in a facile, low-cost and efficient fabrication route for large-area hexagonal arrays of metallic nanodots. In contrast to common NSL-based metallic nanodot arrays, our method creates well-defined metal nanodot arrays with the same configuration as the nanosphere layers used to make it. The double lift-off process used consists of two consecutive metal lift-off steps – first using nanospheres as a mask and then the lift-off metal as another mask for the second lift-off. We used a bilayer of two metals, the bottom sacrificial layer and the top cap layer, and created a re-entrant sidewall profile by undercutting the sacrificial layer to facilitate the final lift-off of metallic nanodots. The quality of the nanodot pattern and the array periodicity was investigated using statistical image analysis and compared to the original nanosphere array in terms of size distribution, surface ruggedness (or smoothness) and array pitch. This nanodot array was later used as an etch mask to create vertically-aligned Si nanowire array, and this combined approach represents a scalable and inexpensive

fabrication of a relatively large-area, ordered array of various nanostructures. Such arrays are potentially useful in biosensing, LSPR, SERS, and other optical applications.

REFERENCES

REFERENCES

1. Ding, T., Herrmann, L. O., de Nijs, B., Benz, F. & Baumberg, J. J. Self-Aligned Colloidal Lithography for Controllable and Tuneable Plasmonic Nanogaps. *Small* 11, 2139–2143 (2015).

2. Zhao, J., Zhang, X., Yonzon, C. R., Haes, A. J. & Van Duyne, R. P. Localized surface plasmon resonance biosensors. *Nanomed.* 1, 219+ (2006).

3. Willets, K. A. & Duyne, R. P. V. Localized Surface Plasmon Resonance Spectroscopy and Sensing. *Annu. Rev. Phys. Chem.* 58, 267–297 (2007).

4. Chen, Y. & Ming, H. Review of surface plasmon resonance and localized surface plasmon resonance sensor. *Photonic Sens.* 2, 37–49 (2012).

5. Rivera, V. A. G., Jr, E. M. & Ferri, F. A. *Localized Surface Plasmon Resonances: Noble Metal Nanoparticle Interaction with Rare-Earth Ions*. (INTECH Open Access Publisher, 2012).

6. Chan, G. H., Zhao, J., Schatz, G. C. & Duyne, R. P. V. Localized Surface Plasmon Resonance Spectroscopy of Triangular Aluminum Nanoparticles. *J. Phys. Chem. C* 112, 13958–13963 (2008).

7. Liu, F. *et al.* Effects of nanoparticle size and cell type on high sensitivity cell detection using a localized surface plasmon resonance biosensor. *Biosens. Bioelectron.* 55, 141–148 (2014).

8. McFarland, A. D. & Van Duyne, R. P. Single Silver Nanoparticles as Real-Time Optical Sensors with Zeptomole Sensitivity. *Nano Lett.* 3, 1057–1062 (2003).

9. Dahlin, A. *et al.* Localized Surface Plasmon Resonance Sensing of Lipid-Membrane-Mediated Biorecognition Events. *J. Am. Chem. Soc.* 127, 5043–5048 (2005).

10. Mühlschlegel, P., Eisler, H.-J., Martin, O. J. F., Hecht, B. & Pohl, D. W. Resonant optical antennas. *Science* 308, 1607–1609 (2005).

11. Mei, F. *et al.* Fabrication and optical properties of controlled Ag nanostructures for plasmonic applications. *J. Appl. Phys.* 114, 083523 (2013).

12. Sharma, B. *et al.* High-performance SERS substrates: Advances and challenges. *MRS Bull.* 38, 615–624 (2013).

13. Langhammer, C., Yuan, Z., Zorić, I. & Kasemo, B. Plasmonic Properties of Supported Pt and Pd Nanostructures. *Nano Lett.* 6, 833–838 (2006).

14. Liu, J., Cai, H., Kong, L. & Zhu, X. Enhancement of surface enhanced raman scattering from arrays of hybrid Au–Ag nanoparticles via localised surface plasmon resonance. *Mater. Sci. Technol.* 31, 857–865 (2014).

15. Dai, Z. G. *et al.* In situ Raman scattering study on a controllable plasmon-driven surface catalysis reaction on Ag nanoparticle arrays. *Nanotechnology* 23, 335701 (2012).

16. Jensen, T. R., Malinsky, M. D., Haynes, C. L. & Van Duyne, R. P. Nanosphere Lithography: Tunable Localized Surface Plasmon Resonance Spectra of Silver Nanoparticles. *J. Phys. Chem. B* 104, 10549–10556 (2000).

17. Gibert, M. *et al.* Self-Organization of Heteroepitaxial CeO2 Nanodots Grown from Chemical Solutions. *Adv. Mater.* 19, 3937–3942 (2007).

18. Cattoni, A., Cambril, E., Decanini, D., Faini, G. & Haghiri-Gosnet, A. M. Soft UV-NIL at 20 nm scale using flexible bi-layer stamp casted on HSQ master mold. *Microelectron. Eng.* 87, 1015–1018 (2010).

19. Bechelany, M. *et al.* Simple Synthetic Route for SERS-Active Gold Nanoparticles Substrate with Controlled Shape and Organization. *Langmuir* 26, 14364–14371 (2010).

20. Buckmaster, R. *et al.* Novel Method for Site-Controlled Surface Nanodot Fabrication by Ion Beam Synthesis. *Nano Lett.* 5, 771–776 (2005).

21. Han, D., Pal, S., Liu, Y. & Yan, H. Folding and cutting DNA into reconfigurable topological nanostructures. *Nat. Nanotechnol.* 5, 712–717 (2010).

22. Stodolka, J. *et al.* Fabrication of two-dimensional hybrid photonic crystals utilizing electron beam lithography. *Microelectron. Eng.* 78–79, 442–447 (2005).

23. Wang, L., Montagne, F., Hoffmann, P. & Pugin, R. Gold nanoring arrays from responsive block copolymer templates. *Chem. Commun.* 3798–3800 (2009). doi:10.1039/B906825B

24. Barcelo, S. J., Lam, S.-T., Gibson, G. A., Sheng, X. & Henze, D. Nanosphere lithography based technique for fabrication of large area well ordered metal particle arrays. in 8323, 83232L-83232L–7 (2012).

25. Fang, Y. *et al.* Scalable bottom-up fabrication of colloidal photonic crystals and periodic plasmonic nanostructures. *J. Mater. Chem. C* 1, 6031–6047 (2013).

26. Vogel, N., Retsch, M., Fustin, C.-A., del Campo, A. & Jonas, U. Advances in Colloidal Assembly: The Design of Structure and Hierarchy in Two and Three Dimensions. *Chem. Rev.* 115, 6265–6311 (2015).

27. Dickey, M. D. *et al.* Fabrication of Arrays of Metal and Metal Oxide Nanotubes by Shadow Evaporation. *ACS Nano* 2, 800–808 (2008).

28. Ho, Y.-H. *et al.* Transparent and conductive metallic electrodes fabricated by using nanosphere lithography. *Org. Electron.* 12, 961–965 (2011).

29. Yeom, J., Ratchford, D., Field, C. R., Brintlinger, T. H. & Pehrsson, P. E. Decoupling Diameter and Pitch in Silicon Nanowire Arrays Made by Metal-Assisted Chemical Etching. *Adv. Funct. Mater.* 24, 106–116 (2014).

30. Zhang, J., Li, Y., Zhang, X. & Yang, B. Colloidal Self-Assembly Meets Nanofabrication: From Two-Dimensional Colloidal Crystals to Nanostructure Arrays. *Adv. Mater.* 22, 4249–4269 (2010).

31. Hulteen, J. C. *et al.* Nanosphere Lithography: Size-Tunable Silver Nanoparticle and Surface Cluster Arrays. *J. Phys. Chem. B* 103, 3854–3863 (1999).

32. Jensen, T. R., Malinsky, M. D., Haynes, C. L. & Van Duyne, R. P. Nanosphere Lithography: Tunable Localized Surface Plasmon Resonance Spectra of Silver Nanoparticles. *J. Phys. Chem. B* 104, 10549–10556 (2000).

33. Haynes, C. L. & Van Duyne, R. P. Nanosphere Lithography: A Versatile Nanofabrication Tool for Studies of Size-Dependent Nanoparticle Optics. *J. Phys. Chem. B* 105, 5599–5611 (2001).

34. Duyne, R. P. V., Hulteen, J. C. & Treichel, D. A. Atomic force microscopy and surface-enhanced Raman spectroscopy. I. Ag island films and Ag film over polymer nanosphere surfaces supported on glass. *J. Chem. Phys.* 99, 2101–2115 (1993).

35. Liang, J.-S., Chen, S.-H., Lin, E.-Y., Luo, D.-F. & Jiang, S.-J. Morphology evolution of glancing angle deposition Ag films on nanosphere-array substrates: Kinetic Monte Carlo simulation. *Comput. Mater. Sci.* 79, 31–35 (2013).

36. Asoh, H., Sakamoto, S. & Ono, S. Metal patterning on silicon surface by site-selective electroless deposition through colloidal crystal templating. *J. Colloid Interface Sci.* 316, 547–552 (2007).

37. Sakamoto, S. *et al.* Ordered hexagonal array of Au nanodots on Si substrate based on colloidal crystal templating. *Nanotechnology* 19, 405304 (2008).

38. Wang, T. *et al.* Nanotransfer printing of gold disk, ring and crescent arrays and their IR range optical properties. *J. Mater. Chem. C* 2, 2333–2340 (2014).

39. Wang, J., Duan, G., Li, Y., Liu, G. & Cai, W. Wet Etching-Assisted Colloidal Lithography: A General Strategy toward Nanodisk and Nanohole Arrays on Arbitrary Substrates. *ACS Appl. Mater. Interfaces* 6, 9207–9213 (2014).

40. Ye, S., Routzahn, A. L. & Carroll, R. L. Fabrication of 3D Metal Dot Arrays by Geometrically Structured Dynamic Shadowing Lithography. *Langmuir* 27, 13806–13812 (2011).

41. Jiang, P. & McFarland, M. J. Wafer-Scale Periodic Nanohole Arrays Templated from Two-Dimensional Nonclose-Packed Colloidal Crystals. *J. Am. Chem. Soc.* 127, 3710–3711 (2005).

42. Mohamed, K. & Alkaisi, M. M. Investigation of a nanofabrication process to achieve high aspect-ratio nanostructures on a quartz substrate. *Nanotechnology* 24, 015302 (2013).

43. Gerbedoen, J.-C. *et al.* All Evaporation Submicron Lift-off Lithography Process with Negative e-Beam QSR-5 Resist. *Microelectron Eng* 103, 123–125 (2013).

44. Williams, K. R. & Muller, R. S. Etch rates for micromachining processing. *J. Microelectromechanical Syst.* 5, 256–269 (1996).

45. Williams, K. R., Gupta, K. & Wasilik, M. Etch rates for micromachining processing-Part II. *J. Microelectromechanical Syst.* 12, 761–778 (2003).

46. Huang, Z., Fang, H. & Zhu, J. Fabrication of Silicon Nanowire Arrays with Controlled Diameter, Length, and Density. *Adv. Mater.* 19, 744–748 (2007).

47. Balasundaram, K. *et al.* Porosity control in metal-assisted chemical etching of degenerately doped silicon nanowires. *Nanotechnology* 23, 305304 (2012).

48. Ratchford, D., Yeom, J., Long, J. P. & Pehrsson, P. E. Influence of inhomogeneous porosity on silicon nanowire Raman enhancement and leaky mode modulated photoluminescence. *Nanoscale* 7, 4124–4133 (2015).

49. Huang, Z., Geyer, N., Werner, P., de Boor, J. & Gösele, U. Metal-Assisted Chemical Etching of Silicon: A Review. *Adv. Mater.* 23, 285–308 (2011).

50. Druzhinin, A. A., Yerokhov, V. Y., Nichkalo, S. I., Berezhanskyi, Y. I. & Chekaylo, M. V. Texturing of the silicon substrate with nanopores and Si nanowires for anti-reflecting surfaces of solar cells. *J. Nano- Electron. Phys.* 7, 1–6 (2015).

CHAPTER 6

CONCLUSION AND OUTLOOKS

One aim of this dissertation is to fabricate micro preconcentrator (PC) and micro reactor components which could survive at medium-to-high-temperature condition for harsh operation environments. Additive manufacturing (AM), was known as metal 3D printing, was employed to produce the small scale microfluidic devices that can operate at high temperature than what polymer can withstand. Unlike the conventional Si-based MEMS approach, AM can create the devices with robust fluidic interconnects and high-yield bonding with straightforward, inexpensive and less time-consuming process. Binder jet printing (BJP), one of the oldest AM technology, which could produce high porous structure was adopted to fabricate the micro PC and microreactors. Chapter 2 introduce the design and material flexible micro preconcentrator (PC) fabricated by BJP process using stainless steel (SS) and boron nitride (BN) sintering additive as the printing material. The BN additive could low the sintering temperature of the SS and also improve the density of the part. Unlike the conventional approach for micro PC fabricated by MEMS whereas the epoxy or polyimide was applied for connection which is weak and not robust, the micro PC created by 3DP approach is compatible with commercial fitting. This high-dense part with internal conduits has sophisticated features inside the SS channel and the part was machinable to meet the commercial PEEK fitting connection requirements. The connection with commercial fitting was tested under high operating pressure and resulting in gas leak-tight which could be used in fluidic applications. Membrane heater was adopted as heating source to heat up the 3DP SS PC for desorption. In order to improve the heat performance of PC, many critical factor of PC was investigated, including thermal mass of PC, insulation condition of PC, and heat ramping rate on PC. We found that low thermal mass could heat up the micro PC for thermal desorption at short

time and achieve much higher temperature for the absorbent inside the micro PC when the heat ramping rate was set. It was also observed that the PC could reach the target temperature more rapidly or with less power consumption with thick insulation condition. High heating rate was chosen for fast response of PC thermal desorption performance because this high heating rate can have the absorbent reach the desorption temperature in a shorter time. The obtained micro PC could serve as a front-end injector for portable micro GC system and real-time gas sensing applications.

In chapter 3, a novel and facile approach combined with Binder jet printing (BJP) and selectively reactive sintering (SRS) process to produce the functionally gradient materials (FGMs)-stainless steel (SS) microreactor which could be used as thermal heating component. The SRS process makes the microreactor has more metal oxide thickness at the edge part and more metal thickness in the center part. This approach overcomes the limitation of conventional techniques of metal/ceramic fabrication approach by 3D printing and adjust the property of the original printing material by straightforward steps. The 3DP SS part was conducting post-processing in oxygen environment and form the metal/metal oxide and obtain the tunable resistivity which is larger than the original SS material. Two heating approaches-Structure heating and External heating were investigated in theoretical analysis, computed simulation and experimental results. Joule heating scenario demonstrated the better efficacy of the microreactor as an energy-efficient process heating unit and maximize the heat transfer than external membrane heating. A high temperature coefficient of resistance (TCR) of the modified metal/metal oxide microreactor was obtained and was adopted as resistance temperature detector (RTD) due to its property. The changes of resistance of 3DP microreactor is highly sensitive to the temperature variation so that the temperature could be calculated and predicted by monitoring the resistance of microreactor.

Moreover, purging the flow of gas also change the temperature of the sample so that it would influence the resistance of microreactor. 3DP microreactor could be used to measure the absolute flow rate when it is properly calibrated with various flow rates and heating condition.

In chapter 4, we present the novel approach to fabricating the pitch control of hexagonal non-close-packed colloidal nanosphere arrays using isotropic deformation of an elastomer. Deformable soft lithography using controlled deformation of elastomeric substrates and subsequent contact printing transfer offers a versatile method to systematically control the lattice spacing and arrangements of the 2D nanosphere array. However, the anisotropic nature of uniaxial and biaxial stretching as well as the strain limit of solvent swelling makes it difficult to create well-separated, ordered 2D nanosphere arrays with large-area hexagonal arrangements. In this chapter, a home-made radial stretching stage was used to generate the large-area hexagonal arrangements of polystyrene nanospheres with controlled pitch. The maximum stretchability and spatial uniformity of the polydimethylsiloxane (PDMS) elastomeric substrate is systematically investigated. A pitch increase as large as 213% is demonstrated using a single stretching-and-transfer process, which is at least three times larger than the maximum pitch increase achievable using a single swelling-and-transfer process. Unlike the colloidal arrays generated by the uniaxial and biaxial stretching, the isotropic expansion of radial stretching allows the hexagonal array to retain its original structures across the entire substrate. Upon radial strain applied to the PDMS sheet, the nanosphere array with modified pitch is transferred to a variety of target substrates, exhibiting different optical behaviors and serving as an etch mask or a template for molding.

Chapter 5 present the metallic nanodots with the same arrangements as the original nanosphere arrays was reported by combining nanosphere lithography (NSL) with novel double lift-off process. In this chapter, a bilayer of two dissimilar metals was employed to create a re-

entrant sidewall profile to undercut the sacrificial layer and facilitate the final lift-off metallic nanodots. The double lift-off process used consists of two consecutive metal lift-off steps - first using nanospheres as a mask and then the lift-off metal as another mask for the second lift-off. The quality of the metallic nnaodots pattern and the array periodicity is investigated using statistical images analysis and compared to the original nanpsphere array in terms of size distribution, surface ruggedness (or smoothness), and array pitch. This nanodot array could be used as an etch mask to create a vertically-aligned Si nanowire array, and this combined approach represents a scalable and inexpensive fabrication of a relatively large-area, ordered array of various nanostructures. Such arrays are potentially useful in biosensing, LSPR, SERS, and other optical applications.

Future work:

1. Continue to work on the different functionally gradient materials (FGMs) by combining the binder jet printing (BJP) process with different metal powder and selectively reactive sintering (SRS) process and investigate the electrical and mechanical property of the FGMs
2. Continue to work on the nanosphere lithography (NSL) with Ecoflex or PDMS with different thickness to create the nanosphere arrays with variable pitch and transfer to target substrates (Si, glass, PET, etc.) by soft lithography. And the optical response of this nanostructure need to be detected. Also continue to develop the new pattern for casting the elastomer mold with thickness variation and study the pitch changes as the function of applied strain.
3. Continue to investigate the wrinkle pattern with the applied strain in different elastomer thickness area and systematically study the bilayer system with different strain stretching and bonding process and study the optical applications.